AD-A141 445 ACOUSTO-OPTIC ADAPTIVE PROCESSING (AOAP)(U) GENERAL 1/2
ELECTRIC CO SYRACUSE NY ELECTRONICS LAB
W A PENN ET AL. DEC 83 RADC-TR-83-156 F30602-81-C-0264
UNCLASSIFIED F/G 20/1 NL

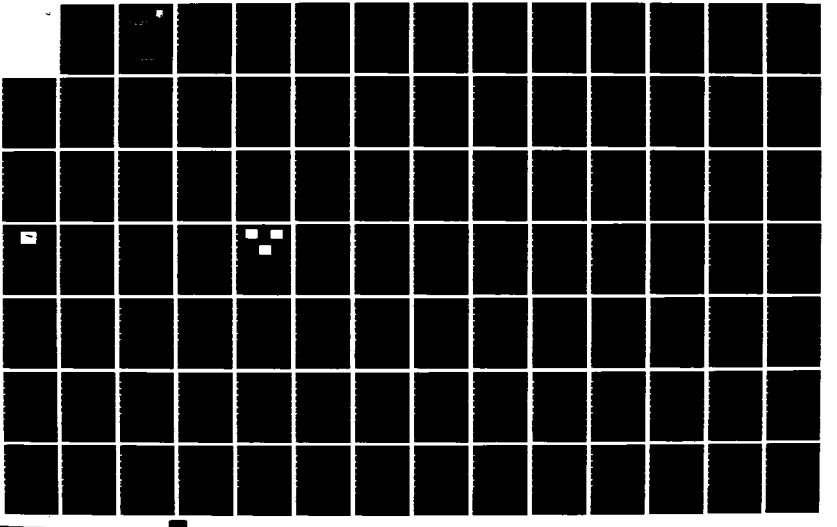

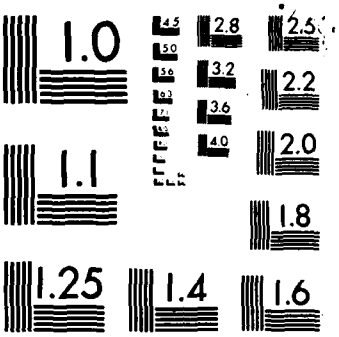

RADC-TR-83-156
Phase Report
December 1983

(12)

ACOUSTO-OPTIC ADAPTIVE PROCESSING (AOAP)

General Electric Company

W. A. Penn, D. R. Morgan, A. Aridgides and M. L. Noble

ROME AIR DEVELOPMENT CENTER
Air Force Systems Command
Griffiss Air Force Base, NY 13441

This report has been reviewed by the RADC Public Affairs Office (PA) and is releasable to the National Technical Information Service (NTIS). At NTIS it will be releasable to the general public, including foreign nations.

RADC-TR-83-156 has been reviewed and is approved for publication.

APPROVED: Vincent C Vannicola

VINCENT C. VANNICOLA
Project Engineer

APPROVED: Frank J Rehm

FRANK J. REHM
Technical Director
Surveillance Division

FOR THE COMMANDER: John P. Huss

JOHN P. HUSS
Acting Chief, Plans Office

If your address has changed or if you wish to be removed from the RADC mailing list, or if the addressee is no longer employed by your organization, please notify RADC (OCTS) Griffiss AFB NY 13441. This will assist us in maintaining a current mailing list.

Do not return copies of this report unless contractual obligations or notices on a specific document requires that it be returned.

UNCLASSIFIED

SECURITY CLASSIFICATION OF THIS PAGE (When Data Entered)

REPORT DOCUMENTATION PAGE	READ INSTRUCTIONS BEFORE COMPLETING FORM
1. REPORT NUMBER RADC-TR-83-156	2. GOVT ACCESSION NO. AD-A141445	3. RECIPIENT'S CATALOG NUMBER
4. TITLE (and Subtitle) ACOUSTO-OPTIC ADAPTIVE PROCESSING (AOAP)	5. TYPE OF REPORT & PERIOD COVERED Phase Report Sep 81 - Oct 82
	6. PERFORMING ORG. REPORT NUMBER N/A
7. AUTHOR(s) W.A. Penn M.L. Noble D.R. Morgan A. Aridgides	8. CONTRACT OR GRANT NUMBER(s) F30602-81-C-0264
9. PERFORMING ORGANIZATION NAME AND ADDRESS General Electric Company Electronics Laboratory Syracuse NY 13221	10. PROGRAM ELEMENT, PROJECT, TASK AREA & WORK UNIT NUMBERS 62702F 45061168
11. CONTROLLING OFFICE NAME AND ADDRESS Rome Air Development Center (OCTS) Griffiss AFB NY 13441	12. REPORT DATE December 1983 13. NUMBER OF PAGES 190
14. MONITORING AGENCY NAME & ADDRESS(if different from Controlling Office) Same	15. SECURITY CLASS. (of this report) UNCLASSIFIED 15a. DECLASSIFICATION/DOWNGRADING SCHEDULE N/A

16. DISTRIBUTION STATEMENT (of this Report)

Approved for public release; distribution unlimited

17. DISTRIBUTION STATEMENT (of the abstract entered in Block 20, if different from Report)

Same

18. SUPPLEMENTARY NOTES

RADC Project Engineer: Vincent C. Vannicola (OCTS)

19. KEY WORDS (Continue on reverse side if necessary and identify by block number)

Optical signal processing
Acousto-optical modulators
Adaptive signal processing
Adaptive sidelobe cancellation

20. ABSTRACT (Continue on reverse side if necessary and identify by block number)

The conventional approach for implementing adaptive cancellers to reject radar interference is to build a separate electronic loop for each required degree of freedom. The process consists of cross-correlating the radar signal with interference samples received by wide-beamwidth auxiliary antennae. These correlation values are then used to adjust the interference waveforms in amplitude and phase so that a precise subtraction of the offending interference can be accomplished.

DD FORM 1 JAN 73 1473 EDITION OF 1 NOV 65 IS OBSOLETE

UNCLASSIFIED

SECURITY CLASSIFICATION OF THIS PAGE (When Data Entered)

An optical implementation of such a processor is the subject of the effort described in this report. In the optical configuration which has been developed, the required operations of multiplication and time delay are provided by acousto-optical (AO) delay lines. The required time integration is provided by an image converter having a suitable delay time. In the optical realization, each resolvable optical element along the AO delay lines used as input modulators represents an additional delay time degree of freedom. Thus we find a "continuum of correlation weights" developed spatially along the delay line. The optical dimension transverse to the direction of acoustic propagation can be used to provide another array dimension.

In the following report, the details of the configuration which have been developed are described. An analysis of the system is presented which investigates the effects of system parameters and the loop gain on cancellation performance. The experimental feasibility model of the system which has been built is described, and the results obtained with this system presented. Limitations in performance which were experienced in the effort are analytically evaluated. Recommendations for improved performance are made. In addition, a theoretical study is included which evaluates an adaptive canceller when operating against a single interference source, with a single multipath environment, i.e., the possibility of direct path reception of the interference, and a single alternative delayed path. The results of this study, which are contained in an extensive set of computer runs, will serve as a guide to evaluating the performance of the eventual closed prototype systems which will be tested first, with laboratory signals, and then in a radar environment.

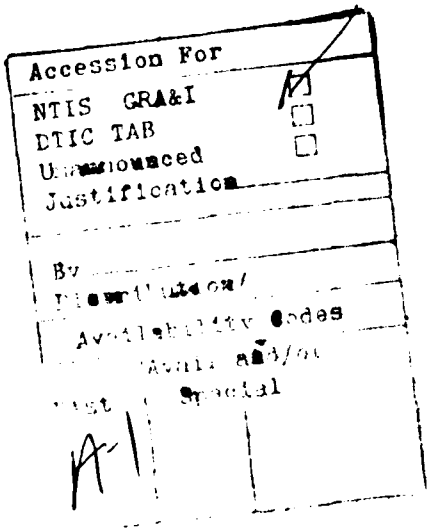

TABLE OF CONTENTS

TABLE OF CONTENTS (Continued)

TABLE OF CONTENTS (Continued)

TABLE OF CONTENTS (Continued)

LIST OF FIGURES

LIST OF FIGURES
(Continued)

LIST OF FIGURES
(Continued)

LIST OF FIGURES
(Continued)

LIST OF FIGURES
(Continued)

LIST OF FIGURES
(Continued)

LIST OF FIGURES
(Continued)

1 INTRODUCTION

1.1 GENERAL

The conventional approach for implementing adaptive signal cancellers to reject radar interference is to build a separate electronic loop for each required degree of freedom. The process consists of cross-correlating the radar signal with interference samples received by wide-beamwidth auxiliary antennae. These correlation values are then used to adjust the interference waveforms in amplitude and phase so that a precise subtraction of the offending interference can be accomplished. [1], [2], [3].

The interference components can arrive reflected from various objects causing "multi-path" delay. Each resolvable time delay requires a new degree of freedom in the processing, and in many cases an even denser time sampling is required. This requirement may be thought of as the need of the processor to have a sample of the interference waveform of the correct structure and timing to cancel such a waveform in the radar signal.

In addition, if there are independent interference sources in the radar space, a new set of adaptive loops with multi-path capability must be provided for each of these sources. The result is often an expensively large number of electronic loops.

An optical implementation of such a processor is the subject of the effort described in this report. The optical AOAP concept was first suggested in 1975 by Dr. Frank R. Dickey, Jr. of the General Electric Co., Syracuse, N.Y. [4] In the period of 1976 - 1980, the General Electric Co. was diligent in developing this idea, culminating in several internal publications [5], [6], and the effort for the Rome Air Development Center which is described in this report.

In the optical configuration which has been developed, the required operations of multiplication and time delay are provided by acousto-optical (AO) delay lines. The required time integration is provided by an image converter having a suitable delay time. In the optical realization, each resolvable optical element along the AO delay lines used as input modulators represents an additional delay time degree of freedom. Thus we find a "continuum of correlation weights" developed spatially along the delay line. The optical dimension transverse to the direction of acoustic propagation can be used to provide another array dimension.

Each additional interference source can be properly cancelled by providing another AO column in the optical aperture. Thus with an array of delay lines in the aperture, a single optical adaptive system can be equivalent to many hundreds of electronic control loops.

In the following report, the details of the configuration which has been developed are described. An analysis of the system is presented which investigates the effects of system parameters and the loop gain on cancellation performance. The experimental feasibility model of the system which has been built is described, and the results obtained with this system presented. Limitations in performance which were experienced in the effort are analytically evaluated. Recommendations for improved performance are made. In addition, a theoretical study is included which evaluates an adaptive canceller when operating against a single interference source, with a single multi-path environment, i.e. the possibility of direct path reception of the interference, and a single alternative delayed path. The results of this study, which are contained in an extensive set of computer runs, will serve as a guide to evaluating the performance of the eventual closed prototype systems which will be tested first with laboratory signals, and then in a radar environment.

1.2 ADAPTIVE CANCELLER LOOPS

A variety of wide-band electronic adaptive systems have been built to perform interference cancellation in radar and sonar systems. Interference is a propagating component in the radar or sonar field, which can be sensed by an auxiliary antenna or array. This interference component is detected and is cross-correlated with the output from the primary, or main antenna or array. Any correlation thus found indicates the presence of an unwanted component in the signal being generated by the system. This interference can be generated from either natural or hostile sources.

When a correlation is established, the precise complex value of this correlation is produced by the signal processing system. This value is then imposed (multiplied) onto the auxiliary (interference) signal to derive a version of the interference adjusted in amplitude and phase, that when subtracted from the main signal will cause interference cancellation. The residue of this subtraction is fed back into the adaptive loop thus formed, in the manner of a closed loop control system, which causes adjustment of the correlation coefficient to improve the cancellation. With proper integration in the control loop, a null is developed in regard to the interference, and the desired signal is passed without appreciable degradation.

The interference components can arrive reflected from various objects causing "multi-path" delayed components. Each resolvable time delay requires a new degree of freedom in the processing. In addition, if there are independent sources in the radar space, a new set of adaptive loops with multi-path capability must be provided for each of these sources. The result is often an expensively large number of electronic loops.

The essentials of a multi-loop electronic canceller are shown in Figure 1-1. The auxiliary signal a(t) is fed

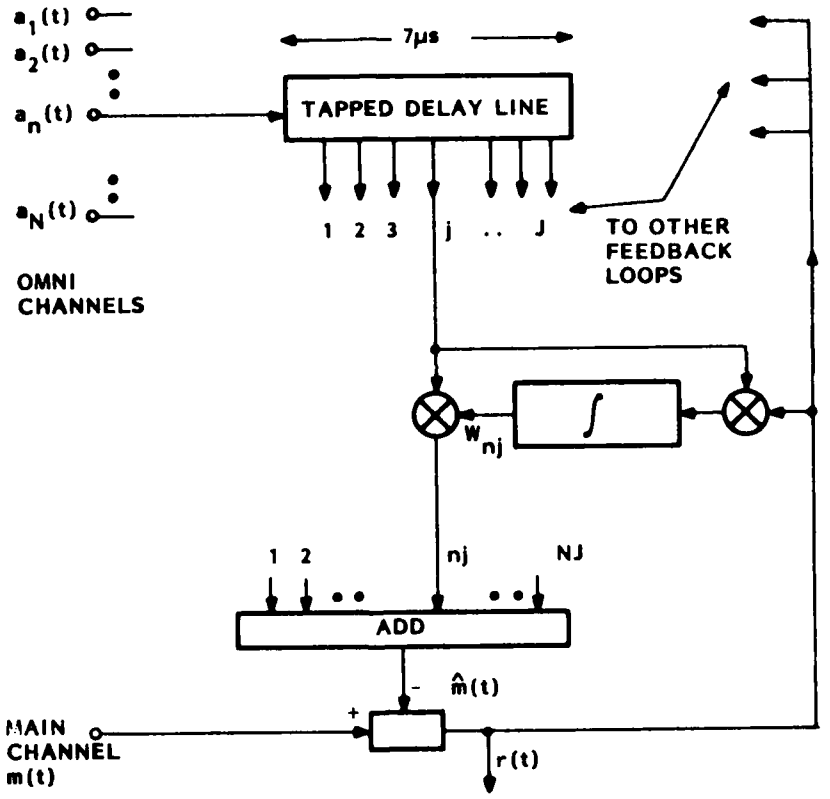

Figure 1-1. Conventional Array of Adaptive Loops

through a tapped delay line to account for all the expected multi-path time delays which might be experienced in the main channel for the given interference component. Each of these taps is provided with a separate electronic loop. The appropriate one of this subset of loops matches the actual time delay of the noise path. This particular loop will be characterized by a high correlation between its delayed auxiliary signal and the multi-path delayed interference component found in the main signal m(t). This correlation is developed by a multiplication between the main and auxiliary signals followed by a time integration. This develops a correlation "weight" W, which then multiplies the auxiliary signal, thus adjusting it in amplitude and phase so that a cancellation occurs with subtraction.

A whole set of loops spaced in time delay is made available for each auxiliary input in the system, which is a design response to the expectation of a multiplicity of noise sources. Thus a degree of freedom, i.e. a separate adaptive loop, is required in the most complete design for each combination of auxiliary input and time delay tap. The totality of signal outputs of the loops, each seeking its own null for its particular combination of input waveform and time delay, is summed (summing bus Σ) and the result is subtracted from the main loop. Analysis shows that the required spacing in time delay for good cancellation is the reciprocal bandwidth of the system, assuming an unlimited offset time window (tapped delay line length) and quadrature sampling. For a finite window, i.e. a finite number of taps, the tap density must be even finer, according to interpolation theory. Further, enough delay and corresponding number of taps must be provided to accommodate multipath components in the auxiliary signal, and the combination may exceed the primary signal delay by a large factor. [2] As a result, in many practical cases, many hundreds of loops are required. Obviously, reduction of the tap density has a direct effect on the amount of equipment required. The resulting compromise of performance is often a difficult issue.

2 MATHEMATICAL DESCRIPTION OF OPTICAL CANCELLER

The functions of the two multiplications, the time integration, and the delay line can be provided by an optical system which includes acousto-optic (AO) Bragg lines. The time integration can be supplied for example, by an image converter for which a phosphor screen provides an optical output with a particular decay time. Other devices are possible and will be discussed.

2.1 SIGNAL CORRELATION

2.1.1 Time Integrating Correlator

One possible arrangement of such a system is shown in Figure 2-1. The light source is modulated with the cancelled main signal. An optical modulator such as an electro-optical (EO) Pockel's cell can be used with a cw laser, or a semiconductor laser diode can be modulated directly. Thus all of the light entering the system varies in amplitude according to the main signal after it has been cancelled, i.e. $\bar{r}(t) = m(t) - \hat{m}(t)$ in Figure 2-1. The light then passes through a Bragg cell delay line, DL1. The acoustic wave launched in this cell is obtained from the auxiliary channel. This function is denoted as $\bar{a}(x-v_a t)$, where v_a is the acoustic velocity. This form of the argument expresses the fact that it is a traveling wave. At each point a multiplication is achieved between $\bar{a}$ and $\bar{r}$. The time offset between the two functions varies with position along the delay line. This product function is imaged point by point on the photocathode of the image converter. The spatial pattern is transferred to the output phosphor screen of the image converter, which performs the desired time integration. It is presumed that the integration is characterized by an exponentially decaying time weighting function. For this application a P1 phosphor was selected, providing a time constant on the order of 10 milliseconds. The spatial pattern thus developed represents the correlation function between $\bar{a}$ and $\bar{r}$, over a time history corresponding to the exponential decay of the optical device. The correlation function is presented in the spatial coordinate as a continuous function of signal offset. This corresponds to the "correlation weight" of the conventional time-sampled architecture composed of electronic loops. If we denote this weight function as $\bar{W}(x,t)$ we have:

$$\bar{W}(x,t) = \frac{1}{T_o} \int_{-\infty}^{t} \bar{a}(x,\tau)\, \bar{r}(\tau)\, e^{\left(\frac{-(t-\tau)}{T_o}\right)}\, d\tau \qquad (2\text{-}1)$$

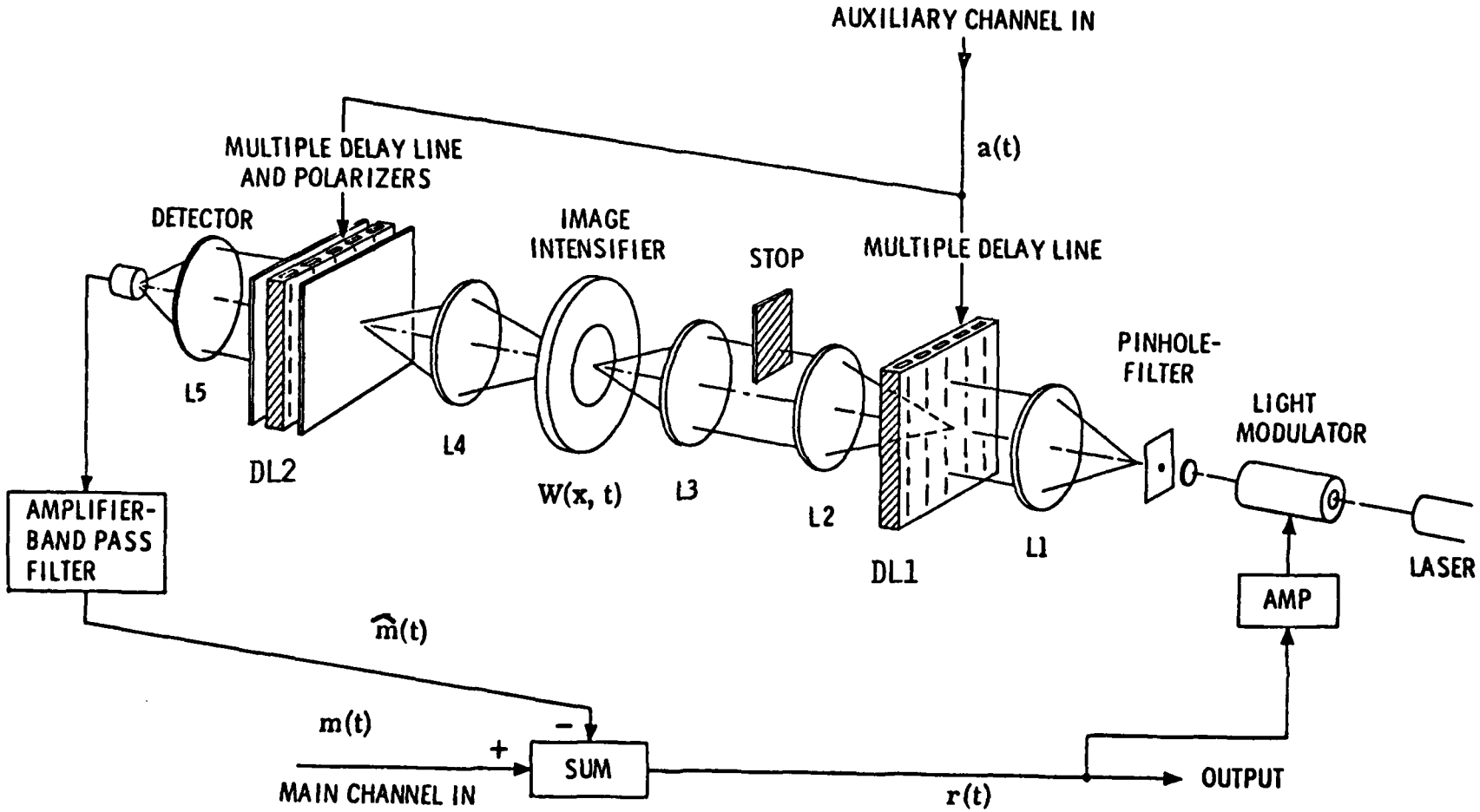

Figure 2-1. Optical Adaptive System

where t = current time

τ = time history variable

T_o = 1/e decay time of optical integrator

x = position along delay line or delay line image, representing correlation offset time

The relation between correlation offset time t' and delay line position x is given in terms of the acoustic velocity v_a as

$$t' = x/v_a \tag{2-2}$$

Both $\bar{a}(x,t)$ and $\bar{r}(t)$ are carrier borne signals. The carrier is the key to handling signals in both amplitude and phase which are thus mathematically representable as complex quantities. The i.f. carrier therefore assumes the role of the original radar or system propagation carrier. Thus if $\bar{a}_m$ and $\bar{r}_m$ are the complex modulation signals, $\bar{a}$ and $\bar{r}$ may be represented in the following way:

$$\bar{r}(t) = \bar{r}_m e^{j\omega_a t} + r_o + \bar{r}_m^* e^{-j\omega_a t} \tag{2-3}$$

where $\bar{r}_m$ = complex modulation signal (over-bars indicate complex quantities)

$\bar{r}_m^*$ = conjugate of $\bar{r}_m$

ω_a = acoustic carrier radian frequency.

Similarly,

$$\bar{a}(x,t) = \bar{a}\left(t - \frac{x}{v_a}\right) = \bar{a}_m \left(t - \frac{x}{v_a}\right) e^{j\omega_a\left(t - \frac{x}{v_a}\right)}$$

$$+ \bar{a}_o + \bar{a}_m^* \left(t - \frac{x}{v_a}\right) e^{-j\omega_a \left(t - \frac{x}{v_a}\right)} \tag{2-4}$$

This form includes the case of optical phase modulation in the delay line. Phase and amplitude modulation are differentiated by the relative phase of the $\bar{a}_m$ terms and a_o. The light beam, bearing signal $\bar{r}$, passes through the delay line which contains $\bar{a}$, and thus a product is formed. This product is imaged on the image converter and integrated

there with time constant T_o, according to equation (2-1). The product $\bar{a}(x,t)\bar{r}(t)$ from (2-3) and (2-4) forms 9 terms. These terms all have a factor

$$e^{\pm jn\omega_a t}, \quad n = 0, 1, 2 \quad .$$

For n = 1,2 the term is characterized by an acoustic carrier frequency, and hence will not survive the integration. Only the three n = 0 terms are thus of interest, and these lead to:

$$\bar{W}(x,t) = \bar{W}_o + \bar{W}_m \, e^{j\omega_a x/v_a} + \bar{W}_m^* \, e^{-j\omega_a x/v_a} \qquad (2\text{-}5)$$

where $W_o = r_o a_o$ = optical bias term

and

$$\bar{W}_m = \frac{1}{T_o} \int_{-\infty}^{t} \bar{a}_m^* \left(\tau - \frac{x}{v_a}\right) \bar{r}_m(\tau) \, e^{\frac{-(t-\tau)}{T_o}} \, d\tau \qquad (2\text{-}6)$$

This is recognized as the complex correlation function between $\bar{a}_m$ and $\bar{r}_m$, involving exponentially weighted integration. Equation (2-5) is equivalent to

$$\bar{W}(x,t) = \bar{W}_o + 2\,|W_m| \cos\left(\omega_a \frac{x}{v_a} + \phi_w\right) \qquad (2\text{-}7)$$

where ϕ_w = phase angle of correlation weight.

This may produce optical amplitude or phase modulation depending on the relative phase of $\bar{W}_o$. Since the delay line is an optical phase modulator, and $\bar{W}_o$ is the product of r_o and a_o, equation (2-4) and therefore equation (2-5) implies optical phase modulation. This condition may be converted to an equal combination of amplitude and phase modulation by eliminating one sideband, e.g. the third term in equation (2-4). The spectrum of the product function (corresponding to the acoustic carrier) is spatially displayed in the focal plane of lens L2. The extra term can thus be eliminated in the optical spatial frequency plane, between lenses L2 and L3 with a simple optical stop. This third term must be optically removed only when the array of optical orders are being generated in a symmetrical manner, such as by a Raman-Nath delay line. This is a line which is thin enough in the direction of optical travel, so that it effectively acts as a phase modulator in a single plane. In the case of a Bragg line, or a "thick" line, when adjusted at the Bragg angle, only one strong diffracted optical order is generated. This order is reconstructively related to the

input beam over the volume of the delay line. Thus, essentially only two orders emanate from the delay line, and the desired amplitude modulation is automatic, without the need of a stop.

2.1.2 Space Integrating Correlator

The $\overline{W}(x,t)$ pattern developed by the integrating device (image converter) is now imaged to a second optical delay line, DL2, similar to the first delay line (see Figure 2-1). Again a product is formed. In the case of an optically coherent system, the required amplitude modulation can again be provided by the elimination of an optical order. However, if the integrating device provides a light pattern which is optically incoherent, some different scheme must be used to provide the required amplitude modulation. An approach to the incoherent case is to use polarizers, and rely on the acoustically induced birefringence in the delay line to alter the polarization. It can be shown that the response of the output light intensity to a birefringent phase shift ϕ (phase difference between principal axes) is given by

$$\frac{I}{I_o} = \sin^2\left(\frac{\phi}{2}\right) \tag{2-8}$$

In this case, a birefringent bias, such as is provided by a phase plate, must be used to linearize the output expressed by (2-8). The product function between $\overline{W}(x,t)$ and $\overline{a}(x,t)$ is spatially integrated across DL2 by lens L5, which is focussed on the output detector. The function launched into DL2 is identical to the signal in DL1. This can be understood by referring to Figure 1-1, in which the generic architecture of an adaptive loop is shown, with the two successive multiplications of the auxiliary signal. Thus we have for the detector signal:

$$\hat{m}(t) = \int_{x_\Delta} \overline{a}(x,t)\, \overline{W}(x,t)\, dx \tag{2-9}$$

where x_Δ is the interval of spatial integration across DL2.

This again produces 9 terms. Now all but three of the terms have a spatial frequency corresponding to the acoustic delay line carrier frequency. The integration expressed by (2-9) will reject these spatial carrier-borne terms, since this is a spatial integration. The result is:

$$\hat{m}(t) = a_o \overline{W}_o + \frac{e^{j\omega_a t}}{T_o} \int_{x_\Delta} \overline{P}_m\, dx + \frac{e^{-j\omega_a t}}{T_o} \int_{x_\Delta} \overline{P}_m^*\, dx \tag{2-10}$$

where

$$\bar{P}_m = \bar{a}_m \left(t - \frac{x}{v_a} \right) \int_{-\infty}^{t} \bar{a}_m^* \left(\tau - \frac{x}{v_a} \right) \bar{r}_m(\tau) e^{\frac{-(t-\tau)}{T_o}} d\tau \qquad (2\text{-}11)$$

The result makes clear that a coherent phase-sensitive operation is accomplished. This is to say that the correct form of the complex correlation function between $\bar{a}$ and $\bar{r}$ is indicated by the integral, and the complex "weight" is used to adjust the amplitude and phase of $\bar{a}_m$ by multiplication for subsequent subtraction and cancellation of the input signal.

2.1.3 Space-time Transfer of Phase Coherent Signals

It is noteworthy to observe the manner in which the complex value of the signal is transferred through the system, with phase preserved. This happens because the signals are borne on either a time or space carrier throughout, in the manner of a narrow band signal. The first signal applied to the system is the modulation on the light source. The phase of this signal is with respect to an assumed reference carrier frequency, which is also the acoustic carrier in the delay lines. The correlation operation between the signal applied to the light source, $\bar{r}$, and the signal in DL1, $\bar{a}$, senses the phase between $\bar{r}$ and $\bar{a}$. This phase information is imparted to the spatial signal developed in the time integrator (image converter). Here the physical position of the spatial carrier cycles with respect to an assumed position denote the phase of the correlation pattern ($\bar{W}$). As the phase difference between $\bar{r}$ and $\bar{a}$ changes, the position of the carrier cycles in W will move accordingly. The dual of this sequence occurs in the second optical section. Here the spatial W-pattern interferes optically with the traveling acoustic wave in DL2, which upon spatial integration by the final lens, causes a time carrier to appear in the detector. The time phase of this output depends on the spatial position of the cycles in the W-function, and the phase of the acoustic wave in DL2. Thus a transfer of signal is made from the time domain to the space domain and back again, always with the phase being coherently transferred at each point.

Inspection of (2-11) reveals that the proper adaptive operation is realized. Signal $\bar{r}$ is inspected for a partial containment of $\bar{a}$ by a complex cross-correlation of $\bar{r}$ with $\bar{a}$ at an arbitrary offset time of x/v_a. This correlation weight is applied to $\bar{a}$, again offset by x/v_a. The result is the correct subtraction for an interference component delayed by x/v_a. Finally this result is integrated over

all values of x that are in an expected range to develop the complete subtraction signal, (equation 2-10).

2.2 CLOSED LOOP CONTROL SYSTEM

When the subtraction is made, the system becomes a closed control system. Some insight into the performance of this closed feedback configuration can be gained by assuming that a unity amplitude, zero phase signal is introduced into the system as the auxiliary input, and a constant signal, as represented by a step function is applied as the main signal input. Hopefully, the system will adapt to this constant signal, and, since the main signal now resembles the auxiliary signal within a proportional constant, the entire signal will be adaptively cancelled in the limit, and the output will approach zero. The optical aperture is assumed to be reasonably small in this simple case, so that only one effective degree of freedom need be assumed for this particular signal. The simplified diagram for this assumed case is shown in Figure 2-2. With the unity amplitude, zero phase auxiliary signal, the two multipliers have the effect of unity multiplication. The well-known closed loop response for a unity forward-gain control loop is

$$F(\omega) = \frac{1}{1 + H(\omega)} \qquad (2\text{-}12)$$

where $H(\omega)$ is the open loop frequency response.

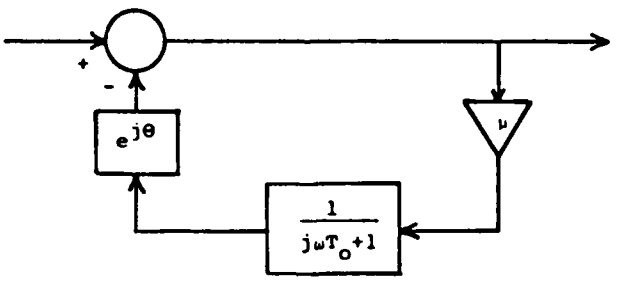

Figure 2-2. Simplified Control Loop

As shown in Figure 2-2, the transfer function $e^{j\theta}$ is placed in the loop to account for any incidental phase shift in the loop. A single-break integrator is assumed to model the optical storage device, such as an image converter. Collecting the appropriate factors and substituting these into (2-12) produces the closed loop transfer function:

$$\frac{1}{1 + H} = \frac{1}{1 + \frac{\mu}{1 + j\omega T_o}} e^{j\theta} \qquad (2\text{-}13)$$

This function has a pole at the complex frequency

$$s_\theta = \frac{-(1 + \mu\ e^{j\theta})}{T_o} \qquad (2\text{-}14)$$

As the spurious phase shift in the loop, θ, varies, the location of this resonant pole will move along the circular trajectory shown in Figure 2-3. Values in the right half plane lead to loop instability. It is significant that the response of this system is characterized by a single complex pole, rather than the usual case of a conjugate pair. It will be remembered that the variable which is mathematically represented throughout the loop is a carrier-borne signal, and the phase angle of the variable represents the instantaneous phase of the signal with respect to an assumed stable carrier frequency. In the usual control analysis, a complex pair of poles represents a sinusoidal oscillation in the amplitude of the controlled variable with an exponential growth or decay. Here a single pole represents a decay or growth of the signal, but the oscillation now manifests itself as a forward or backward progression of phase, i.e. a frequency shift for a time variable, and a spatial motion for a space variable. Consider, for example, the spatial sine-wave pattern representing the continuum of correlation weights, on the image intensifier. If the input is suddenly reduced to zero, implying that the correlation weights will also then approach zero, a moving sine-wave pattern will be observed, with the a.c. amplitude performing an exponential decay. If the modulation function for this behavior is plotted in the complex time domain plane, the trajectory is an inward spiral, approaching zero as a center point. This behavior has been described by Morgan [7]. The speed of this motion will depend on the amount of spurious phase shift.

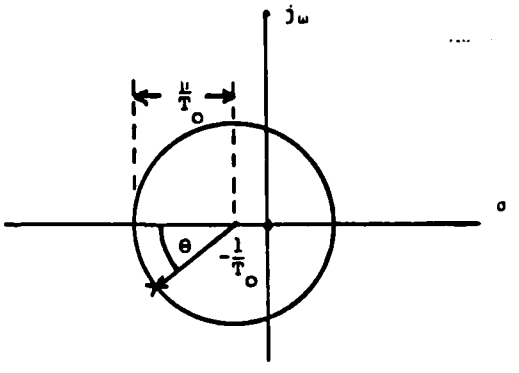

Figure 2-3. Trajectory of Closed Loop Pole in Complex Plane

3 DESCRIPTION OF EXPERIMENTAL SYSTEM

The experimental system was arranged essentially as shown in Figure 2-1. It is composed of two parts. The first section, from the light source to the optical integrator (image intensifier) is a time-integrating correlator. The second section, from the integrator to the output detector is a space-integrating correlator.

3.1 TIME INTEGRATING CORRELATOR

3.1.1 General

The operation of the time integrating correlator depends on signal modulation of the light source, and the first delay line. The main residue signal is imposed on the light source, and the auxiliary signal is passed through the first delay line in the form of a sound wave. Thus at each point along the delay line an optical multiplication is achieved, and at each such point a different correlation offset time is represented. This product function is then imaged on the image intensifier or any alternate integrating device that might be used to develop a spatial display of the continuous correlation function between the two signals.

3.1.2 Light Source

One possibility for a satisfactory light source, which would have several desirable characteristics, is a visible gas laser, such as an argon ion laser. This requires the use of an external optical time modulator, such as a Pockel's cell. One advantage of this approach is the abundance of input coherent light that can be thus obtained. On the order of 1 watt of usable spatially filtered light can be made available in the illumination of the first delay line. To evaluate this approach a Lasermetrics 3079 Pockel's Cell modulator was obtained. This is a KD*P (KD_2PO_4 or potassium deuterium phosphate) crystal, with a clear aperture of 2 mm diameter. The half-wave voltage, V_{HW}, is that voltage required to produce a wave retardation difference between the two optical axes of π radians. For the 3079 cell $V_{H/W}$ is 162 v. Experiments were conducted at 60 MHz using a tuned r.f. driver. This experience shows that it is very difficult to shield the high r.f. power from the subsequent electronics of the system. In particular r.f. feedthrough can be experienced which feeds directly into the optical detector circuit. For this reason, and the general inconvenience of providing high power r.f. at a substantial bandwidth, the alternative of using a semiconductor laser diode was elected.

The use of a semi-conductor laser diode offers a much more convenient signal modulation mechanism, i.e., the diode can be electrically modulated directly. Modulation bandwidths up to 1 GHz are available, as far as the intrinsic response of the device is concerned.

A Hitachi 1600 Ga Al As diode is used in our experiment. This device operates nominally at 830 nm, i.e. the near infra-red region. The diode is mounted on a heat sink to help avoid mode-hopping due to temperature shift. The temperature of this heat-sink is regulated by a thermal feedback control loop to keep the temperature within approximately a 1°C range.

Figure 3-1 shows the vulnerability of this device to mode-hopping with temperature change. Approximately 4 frequency jumps occur over a temperature range of 6°C, covering a wavelength shift of about 1 nm according to Hitachi data. [8]

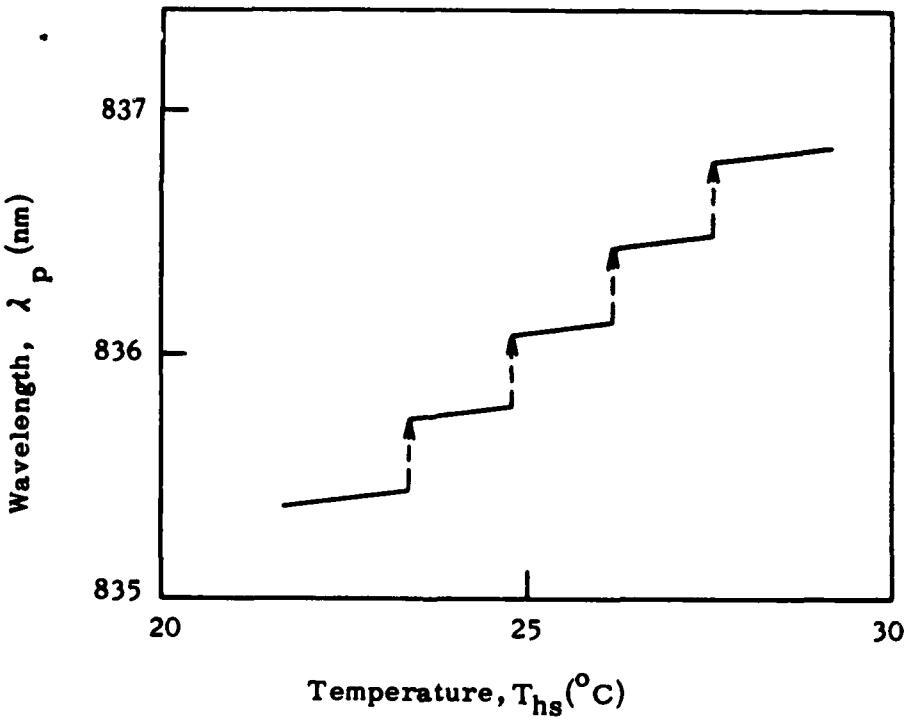

Figure 3-1. Peak Wavelength vs. Heat Sink Temperature of an HLP1000 Diode at a Constant DC Current*

* Taken from Reference [8]

Figure 3-2 is a graph of laser output power as a function of diode forward current, for various temperatures.

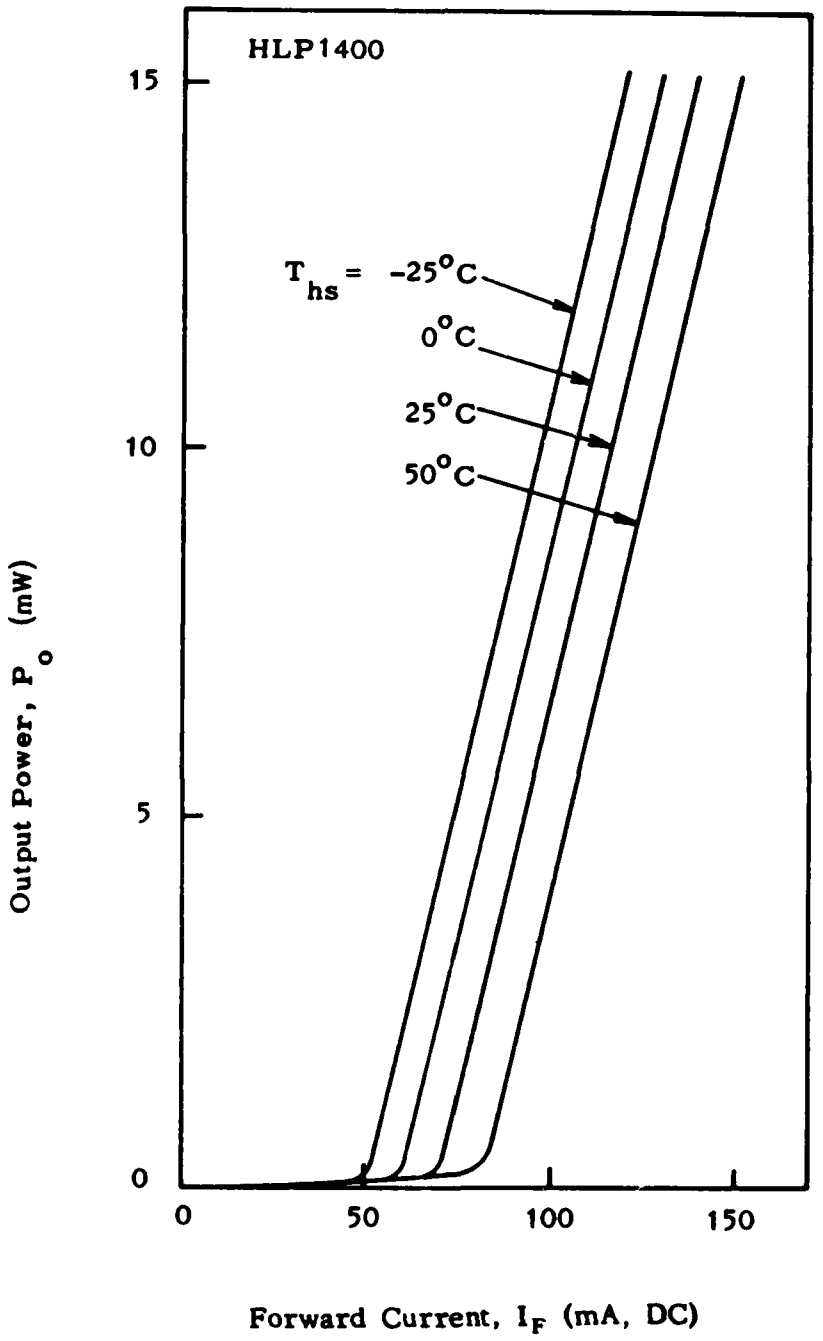

Figure 3-2. Typical Light vs. Current Characteristics of HLP1000 Diodes*

*Taken from Reference [8]

Lasing threshold current for this device is rated to be typically 70 ma. The device was operated in the experiment at a bias current of 80 to 90 ma. It is believed that approximately 2 mw of optical power was thus obtained, with a maximum rating of 10 mw available. Added to this bias current is the r.f. modulation developed by a current gain amplifier, fed by a signal generator with an output of approximately 0 dBm. By crossing the laser threshold on the swings of the carrier cycle, 100% light modulation was observed.

3.1.3 Delay Line

The delay line used for the initial experiment is an Isomet Type 1201 AO modulator. This is a glass unit operating at a center frequency of 37 MHz. It has an aperture of 2 mm × 5 mm. Our tests have been with cw excitation only. The unit is approximately 35 mm thick, which puts it fairly far into the Bragg mode. With an input drive of 1 watt a diffraction efficiency of 50% is easily achieved. The same signal generator output used to drive the laser diode light source was used as the signal for this delay line. The signal generator output is amplified in an ENI 3-watt r.f. amplifier. This is enough to provide 50% of diffraction efficiency, which means that 50% of the input light energy in the optical zero-order is deflected into the first order diffracted order. These two orders are then used to provide an amplitude modulated space carrier on the image intensifier. Since both orders are equal, 100% amplitude modulation is obtained.

3.1.4 Optics

The imaging optics used for the AOAP experiment consist of telecentric systems. A telecentric system uses two lenses with a common front/back focal plane, as shown in Figure 3-3. The imaging then occurs between the front focal plane of the first lens (object plane), to the back focal plane of the second lens. The advantages of this configuration are (1) exceptional freedom from aberrations, since each lens is used at infinite focus, for which it is usually designed, (2) three-dimensional undistorted imaging when the lenses have identical focal lengths, and (3) the provision between the lenses of a true Fourier spatial frequency plane, when coherent light is used. In the present configuration, two Bausch and Lomb 152 mm Baltar f/2.8 lenses were used, as well as a third such lens to accomplish collimation of the laser beam. This provides precise 1:1 imaging between the delay line and the optical integrator/image converter.

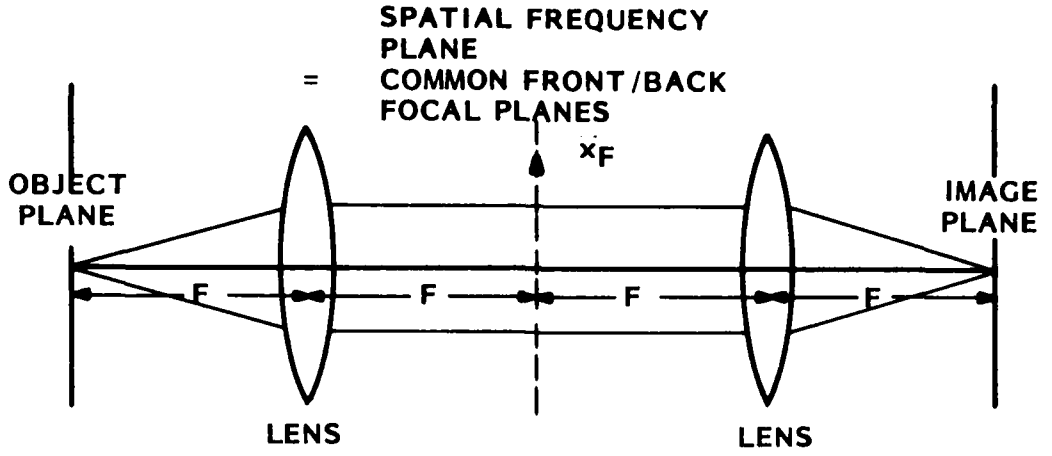

Figure 3-3. Telecentric Imaging Optics

A frequency plane is thus provided, again as shown in Figure 3-3, in which the spatial dimension x_F, is related to the spatial frequency in the delay line, or the output image at the image intensifier by the relation:

$$x_F = F_o \frac{\lambda f_x}{\sqrt{1 - (\lambda f_x)^2}} \qquad (3\text{-}1)$$

where

F_o = focal length

f_x = spatial frequency

For paraxial systems such as this, (meaning all light rays are close to being parallel to the optical axis), the relation reduces to

$$x_F = F_o \lambda f_x \qquad (3\text{-}2)$$

For the acoustic carrier frequency of f_o = 60 MHz, and an acoustic velocity in quartz of 5.95 mm/μsec we have

f_{xol} = spatial frequency of sound carrier in delay line

$$= \frac{f_o}{v_a} = \frac{60 \text{ MHz}}{5.95 \text{ mm/}\mu\text{sec}} \qquad (3\text{-}3)$$

= 10.7 cycles/mm

f_o = acoustic carrier frequency

At 37.5 MHz, and v_a = 3.7 mm/μsec for the Isomet glass line which was used, we have the same spatial frequency.

From (3-2), the spatial separation between the zero order, and the diffracted first order, corresponding to the acoustic carrier frequency is:

$$x_{F1} = F_o \lambda f_{xol} = F_o \lambda \frac{f_o}{v_a} = F_o \frac{\lambda}{\Lambda} \qquad (3\text{-}4)$$

where

F_o = Lens focal length

f_{xol} = Spatial frequency of acoustic wave in delay line

f_o = Acoustic carrier frequency

Λ = Acoustic wavelength

For the case of 10.7 cycles/mm, and λ = 830 nm, one obtains:

$$x_{F1} = 152 \times .830 \times 10^{-3} \times 10.7$$

$$= 1.35 \text{ mm}$$

On this scale, it is quite convenient to sort orders if necessary.

3.1.5 Image Converter

Our original concept has been to use an image intensifier/converter as the optical temporal integrator required for AOAP operation. Such an image converter will accept an input light pattern which is composed of either coherent or incoherent light on its photocathode. Electrons generated from the photo-cathode then are accelerated to a phosphor output screen, where the output image is found. In this AOAP configuration it is being used as a coherent to incoherent converter. The optical wavelength, at the same time, is converted from 830 nm to the mid-visible band, centered in the region of 550 nm.

The desirable range of integration time required for an AOAP system is estimated to be from 3 to 100 milliseconds. The integration time is defined as the time required to reach the 1/e point in the natural exponential decay characteristic of the device. Gain, while not vital, is desirable. The

resolution of the device should be adequate to handle the 10 cycles/mm spatial frequency generated by the delay lines. Thus the MTF curve should be well above 50% at 10 cycles/mm.

Several image intensifier configurations could be selected for the AOAP system. The following discussion covers three major classes of this type of device.

Magnetically focussed. Figure 3-4 shows the three image intensifier configurations presently in use. The first is the magnetically focussed intensifier shown in Figure 3-4a. This configuration consists of a cylindrical envelope, usually made of glass, with windows at each end. The internal surface of the input window is coated with a thin layer of material that emits free electrons, when illuminated with light energy in the acceptance band. Most photoemitters have a response that includes the visible spectrum with several extending a short distance to adjacent bands. These photoemitters are the same surfaces used for photocathodes in photomultiplier tubes. The opposite end of this intensifer envelope contains a window with a phosphor layer. Each window has a transmission reponse matched to the wavelength range of its respective surface. These devices are sometimes called image converters because the input radiation can be in a different wavelength from the output radiation.

Operation of this device proceeds with the input image interacting with the photoemitter, or photocathode to produce an electronic image of low-energy emitted electrons. A large DC potential is maintained between the photocathode and the phosphor coated anode at the other end of the envelope. Thus the low energy electronics are accelerated to provide a high energy input to the phosphor. During this transit from the photocathode to the phosphor plate the electrons are focussed under the action of the magnetic field from the focus coil. In the arrangement as shown, the magnetic focus coil will operate at a magnification of nearly unity and provides an exceptionally high resolution image. It is possible to obtain resolutions as high as 100 cycles/mm with this magnetic focus arrangement.

Proximity focussed. Figure 3-4b shows the proximity focussed diode image intensifier. This is a very simple, but effective device. Here the focus is effected by the same electrostatic field as is used for acceleration. This is of course, a compromise. The resolution cannot be as high as the magnetically focussed intensifier because here there really is no focus action, and the high axial field merely holds off the normal defocussing action due to space charge spreading of the electronic image. Likewise since the plates must be kept very close one cannot use as high an acceler-

ating voltage, and therefore the gain is lower. In spite of these differences the proximity focussed diode intensifier has substantial advantages. It is physically small, lightweight, has few parts, has only two electrodes and one power supply, gives good focussed performance at any voltage in its range. In short, it is simple and reliable and is the lowest cost option.

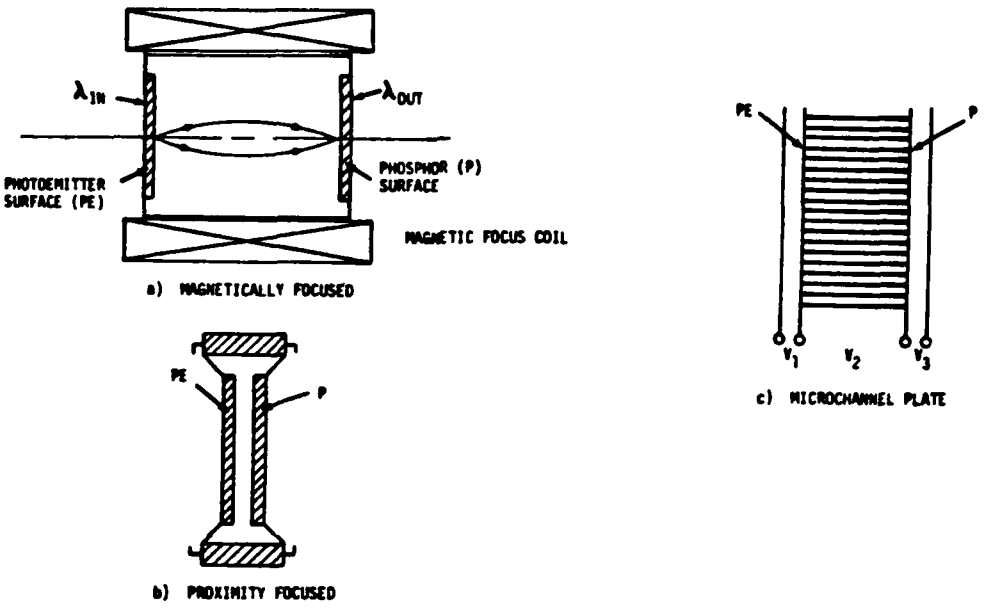

Figure 3-4. Image Intensifier Configurations

Microchannel Plate. The third device is called a microchannel plate because of its construction. This intensifier uses a large collection of parallel microchannel channel to provide an image gain. Each microchannel is a tiny secondary emission amplifier made by coating the thin semiconductor film on the inside of a micro glass cylinder. Under the axial potential generated by contacts at each end of this tube, one entering electron impacts the film on the wall, generating more than one secondary electron. This process repeats many times over as the number of avalanching electrons grow. This type of secondary emission amplifier is a relatively low-noise amplifier capable of gains as high as 10^4 or 10^5.

As shown by the sketch of Figure 3-4c, the microchannel plate image intensifier is arranged to be operated with three power supplies (different voltages). Voltage V1 places a potential between the photocathode and the microchannel input face. This provides proximity focus, as accomplished in Figure 3-4b. The same approach is used to focus the output electronic image to the phosphor plate. At the same time these potentials increase the energy of the initially low-energy electronic image.

Table I shows a device performance comparison for the three configurations. This table is an approximate summary of presently available devices. One can quickly get a general idea of the capability of the different configurations. It is to be noted that in cost the magnetic focussed is the most expensive with the MCP about 3/4 and the proximity focussed about 1/4 this cost.

TABLE I. PERFORMANCE COMPARISON FOR IMAGE INTENSIFIER CONFIGURATIONS

40 MM APERTURE (INPUT/OUTPUT) S-20 Photocathode, P-20 Phosphor				
Device Type	Limiting 2-5% MTF	Resolution (cycles/mm) ~50% MTF	Gain	Cost (Approximate)
1) Magnetically Focussed	85-90	45	60-120	20$K-$25K
2) Proximity Focussed	45	18	20-50	5$K
3) Microchannel Plate (MCP)	20-25	10	10^4	15$K

When comparing gain, the proximity focussed is the lowest gain, with the magnetically focussed about twice this gain. The MCP has the capability of exceedingly high gain and in fact, this is the major advantage of the microchannel plate. The gain of the MCP device is so high that one must exercise care not to exceed some rather low level like 10^{-4} foot-candles or the output is saturated.

Spatial resolution in the MCP is limited by the spatial structure of the microchannel array to about 20 to 25 cycles/mm. In the proximity device, the resolution is limited to nearly 45 cycles/mm by the charge spreading in the proximity focus region between the photocathode and the phosphor plate. Resolution in the magnetically focussed device is limited by the electron optical aberrations of the magnetic focus coil, and this limit is about 100 cycles/mm.

After careful consideration and comparison of the various capabilities of the three intensifier configurations we selected the proximity focussed device. It offers the best tradeoff in performance specifications for the intended AOAP application.

Most of the present-day image intensifiers are intended to intensify an image for direct visual observation or as an input to a TV imaging device such as a vidicon. Consequently these devices are usually sold with the S-20/P-20 combination. For the AOAP system we want a special phosphor to obtain the proper integration time. Table II shows a list of phosphor types and certain charactistic data. Of specific interest are those phosphors with a medium to medium long persistence. We wanted to select a suitable phosphor with a decay to 10% brightness in the range of 5 to no more than 200 milliseconds to yield a decay to 50% in the range of 1 to about 50 milliseconds. As one can see, there are at least 6 choices open. The specific selection was made on more detailed performance features.

The resolution of 10 and 20 cycles/mm is the assumed resolution at a 50% MTF for the MCP and the proximity focussed devices respectively. We see that the MCP does not give sufficient resolution to readily yield 300 or more cycles per side dimension except in the largest apertures. The proximity focussed intensifier of 40 mm is our choice since it can yield the desired resolution in a 40 mm diameter aperture. Larger apertures produce inconveniences in the optical system, as well as requiring more expensive optics.

Figure 3-5 shows the MTF curve for the ITT 40 mm proximity focussed (diode) intensifier. This curve shows the resolution at 50% MTF is about 17-18 cycles/mm.

TABLE II. SUMMARY OF CHARACTERISTICS OF COMMONLY USED "STANDARD" PHOSPHOR SCREENS AS PUBLISHED BY EIA

Type	Color (Kelly Chart)	Spectral Peak (Angstroms)	CIE Coordinates x	CIE Coordinates y	Persistence	Decay To 10% Brightness	Applications
P1	Yellowish Green	5250	.218	.712	Medium	24msec	General Purpose Visual Displays
P2	Yellowish Green	5350	.279	.534	Med. Short	~75usec	Largely Superseded by P31
P4	White	4600 5600	.270	.300	Med. Short	20usec 60usec	60Hz Television
P7	Blue Yellow Green	4400 5550	.151 .357	.032 .537	Med. Short Long	~50usec .35sec	Radar and Oscillography
P11	Blue	4600	.139	.148	Med. Short	~50usec	Photographic Recording
P12	Orange	5900	.605	.394	Long	200msec	Low Frame Rate Displays & Radar
P14	Purplish Blue Yellowish Orange	4400 6000	.150 .504	.093 .443	Med. Short Medium	25usec 5msec	Radar
P16	Bluish Purple	3800	.175	.003	Very Short	.12usec	Flying Spot Scanners & UV Recording
P19	Orange	5900	.572	.442	Long	220msec	Radar
P20	Yellow Green	5600	.426	.546	Med. Short	~.2msec	Bright Visual Displays
P24	Green	5100	.245	.441	Short	~1.5usec	Color Flying Spot Scanner
P25	Orange	6100	.557	.430	Medium	45msec	Radar
P26	Orange	5950	.582	.416	Very Long	~10sec	Radar
P28	Yellow Green	5500	.370	.540	Long	~.5sec	Long Persistence At Low Brightness Only
P31	Green	5200	.193	.420	Med. Short	40usec	Bright Visual Displays Oscillography
P33	Orange	5875	.559	.440	Very Long	~10sec	Radar
P36	Yellow Green	5500	.400	.543	Very Short	.25usec	Flying Spot Scanners
P37	Blue	4700	.143	.208	Very Short	.15usec	Flying Spot Scanners & Photographic Recording
P38	Orange	6000	.561	.437	Very Long	1sec	Low Frame Rate Displays & Radar
P39	Yellowish Green	5250	.223	.698	Long	150msec	Medium Frame Rate Displays & Radar
P40	White Yellow Green	4400 5500	.276	.311	Med. Short Long	150usec ~.5sec	Longer Persistence Version of P4
P41	Greenish Yellow	5900 3800	.541 .175	.456 .003	Long Very Short	200msec .12usec	Low Frame Rate Display With Light Pen
P42	Yellowish Green	5200	.238	.568	Med. Long	10msec	Medium Frame Rate Display
P43	Yellowish Green	5440	.333	.556	Medium	1.2msec	Bright High Contrast Displays with Band Pass Filter
P44	Yellowish Green	5440	.300	.596	Medium	1.2msec	Bright High Contrast Displays with Band Pass Filter
P45	White	**	.253	.312	Medium	1.7msec	Preferred Alternative To P4 For High Brightness White Displays
P46	Yellow Green	5300	.365	.595	Very Short	0.16usec	Flying Spot Scanners, Preferred Alternative to P36
P47	Purplish Blue	4000	.166	.101	Very Short	.080usec	Flying Spot Scanners, Superior To P16 In Most Applications
P48	Yellow Green	4000 5250	.365	.474	Very Short	0.12usec	Color Flying Spot Scanner Superior To P24 In Most Applications
P49	Red 10KV Green 17KV	6150 5150	.672 .315	.327 .615	Medium Medium	1.2msec 30msec	High Resolution Multi Color
P50	Red 8KV Yel. Green 15KV	6200 5450	.655 .398	.340 .548	Medium Med. Short	5msec 20usec	High Resolution Multi Color
P51	Red 6KV Yel. Green 12KV	6225 5450	.675 .414	.325 .514	Medium Med. Short	2.2msec 31usec	High Resolution Multi Color
P52	Purplish-Blue	4000	.157	.075	Med. Short	26usec	Photo Recording

*Obtainable from: E.I.A. (Electronic Industries Association), Type Administration Engineering Department, 2001 Eye Street, N.W., Washington D.C. 20006.
**Multiple Peaks.

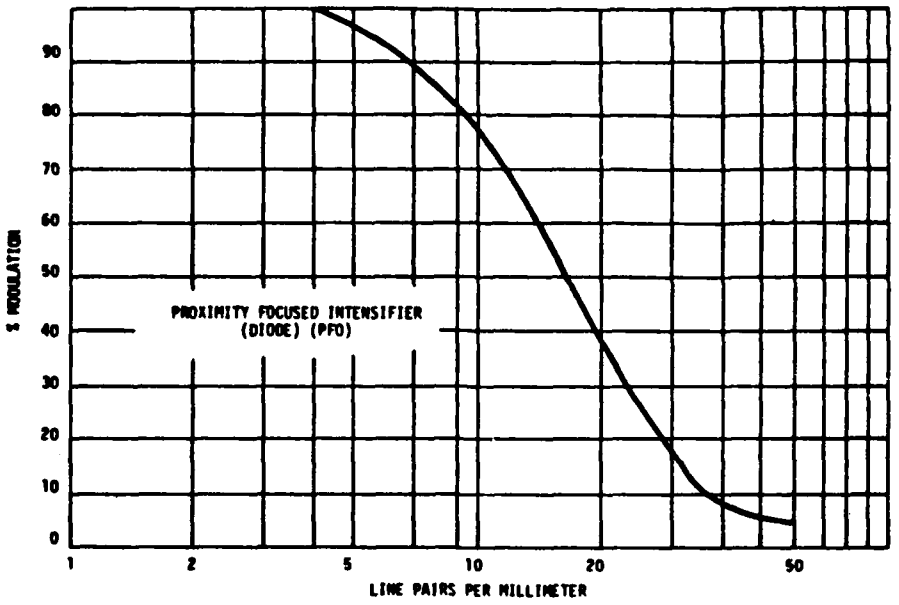

Figure 3-5. Modulation Transfer Function

Two ITT proximity focussed intensifiers were obtained for use in the present experiment.

The first is an ITT F4108 diode. This has a usable aperture diameter of 25 mm. This also has an "extended red" S-20 photoemitter. The spectral response of this emitter is discussed in Section 4.3.1. The design accelerating voltage is 6 kilovolts. At this level the tube has a luminous gain of 100.

The phosphor screen of this device is type P-20. The center color of the emission is yellow-green, peaking at 550 nm. The response time is in the region of 100 μsec. Thus this device does not provide the integration time needed for the AOAP system, but it has proved very useful in testing the time-integrating correlator. It was used to achieve the cw correlation pattern described in the next section.

The second device obtained is an ITT F4109 unit. This device, a non-standard specification, differs from the F4108 unit in three ways:

1) It has a usable aperture of 40 mm, which provides a space-bandwidth product of 70 for the expanded AOAP, corresponding to 7 μsec at 10 MHz bandwidth.

2) It has a P-1 phosphor, which is characterized by a 10 millisecond response, quite adequate for AOAP integration.

3) It does not have a fiber-optic transfer face-plate, used on standard devices for ease of image transfer. This eliminates a slight reduction of MTF, and slight spatial phase distortion encountered in fiber optic faceplates.

3.1.6 Time-integrating Correlator Experimental Results

Using the configuration described in the preceding discussion the auto-correlation of a cw carrrier was developed on the output screen of the F4108 intensifier. A 37 MHz carrier obtained from the signal generator was applied to both the delay line, an Isomet 1201 acousto-optic modulator, and the laser diode light source. The electrical input power to the delay line was 1 watt. The current modulation on the laser diode was approximately 50%.

The moving phase disturbances in the delay line are optically projected on the photocathode of the image intensifier as a moving image. The time modulation favors a particular spatial phase position of this image depending on the phase relation between the laser output and delay line excitation. The phase modulation is converted to amplitude modulation by virtue of the delay line operating in a Bragg mode. When the delay line is carefully adjusted in angle with respect to the input optical beam at the Bragg angle, only one important diffraction beam is developed (a first order). Essentially only this one diffracted order and the zero order exist in the output space. The interference between these two orders develops the desired carrier amplitude modulation. If the delay line were in the Raman-Nath regime, with normal input incidence of the illuminating light beam, a symmetrical pattern of orders would be produced, and, most importantly, these would be the -1, 0, and +1 orders. The phases of these orders would be arranged in accordance with optical phase modulation. One way to produce carrier amplitude modulation from this situation is the elimination of one of the first orders, leaving only the other first order and the zero order. This is then equivalent to the Bragg effect.

The resulting spatial pattern obtained on the output screen of the intensifier for both inputs to the delay line and the laser modulation coming from a 37 MHz sine-wave generator is shown in Figure 3-6. This pattern represents the auto-correlation of the 37 MHz input. The non-uniformity

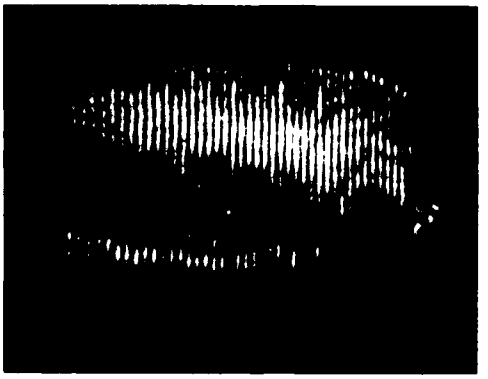

Figure 3-6. Spatial Correlation Function for a Simple R.F. Carrier (Autocorrelation)

of the light pattern is due to the modal structure of the laser beam. This is correctable with a pinhole-spatial filter in front of the laser output.

The grating pattern disappears, as it should, when either the laser modulation drive, or the input to the acoustic transducer on the delay line is removed. If the delay line is moved, the pattern moves a corresponding distance.

It is clear that if a more complex waveform were applied to the laser and delay line the appropriate carrier-borne auto-correlation function would appear as a spatial pattern on the image intensifier.

3.2 SPACE-INTEGRATING CORRELATOR

3.2.1 General

The second optical section of the AOAP, from the image intensifier to the output detector is the space integrating correlator, in which the input to this section is an optical spatial pattern, and this is imaged to a delay line. As the acoustic-borne function travels by the pattern image, a point-by-point spatial multiplication is performed at the delay line. This "continuum" of products is collected by the final lens and the spatial integral of this product is then delivered to the final detector by action of the final lens. Thus the cross-correlation between the spatial pattern on the intensifier, and the function in the delay line is implemented.

3.2.2 Incoherent Experiment

Our original concept was to use the incoherent optical field generated by the image intensifier as the source for the space-integrating correlator. The optical radiation from the image intensifier, which is self-luminous radiation from a phosphor, is totally incoherent, and radiates into an angular hemisphere. Of this, only a small sector of ray direction can be used. Rays in this sector are sufficiently well collimated so as to essentially register in angle with the acoustic wavefront in the delay line. Rays which cross acoustic wavefronts receive very little net modulation in optical phase. Rays which are perfectly aligned with the acoustic wavefronts receive consistent modulation during their entire travel through the delay line. This will be quantitatively discussed in a later section.

If the acoustic wavefronts have significant curvature, it may be that the crossing of wavefronts is unavoidable, and poor modulation will result for all rays.

3.2.3 Delay Line

The incoherent mode was attempted with a delay line built by Andersen Laboratories. This is a fused quartz line with a velocity of approximately 6mm/μsec. Thus at 60 MHz, a spatial frequency is generated which is compatible with 10 cycles/mm produced on the image intensifier. The delay line was tested and shown by Andersen to be capable of 43% diffraction efficiency in the primary Bragg 1st order. This line is 15 mm thick, which classifies it as weakly Bragg. The 43% efficiency implies total optical phase modulation of approximately 1.43 radians, which is to say that the peak optical phase deviation caused by a negative or positive swing of the acoustic carrier corresponds to 1.43 radians. This result assumes strictly Bragg operation.

3.2.4 Optics

The optics used for the space integrating correlator is similar to those used for the time integrating correlator. A telecentric system using two Bausch and Lomb Baltar f/2.8 152mm lenses was used, although this is not explicitly shown in Figure 2-1. This system images the input pattern to the delay line. The telecentric system provides the equivalent of a spatial frequency plane between the two lenses, although a spatial frequency is not displayed here in an incoherent system. Position in this plane corresponds to ray angle in either the object (grating) or image (delay line) planes. Thus the correct sector of angles can be selected here to properly register with the acoustic wavefronts in the delay line.

The optical field produced by the intensifier may be adequately simulated by a photographic grating transparency with a 10 cycle/mm pattern on it. With incoherent illumination through a diffuse screen, the radiation obtained is dispersed into approximately a hemisphere, as it is in the image intensifier. The light level may be easily matched to simulate that of the intensifier. By using a spectral source, such as a mercury vapor lamp, a spectral optical width roughly equivalent to the intensifier output may also be obtained.

3.2.5 Detector

An avalanche photodetector (APD) diode was used as the output detector in the space-integrating correlator. This photodetector was used with a broad-band three-stage transistor amplifier which had current and voltage limiting circuits to protect the diode. The APD has voltage, current and power limits that must be strictly adhered to in order to avoid damaging it.

A constant-current mode was selected as an alternative to temperature compensating the applied diode voltage. The diode itself is an RCA C30817 device, with a rated voltage dependence with temperature of 1/2 volt per °C. This temperature dependence is fairly linear between -40°C and +60°C. The circuitry thus allows one to select the average diode current over fairly wide limits of temperature and average input light intensity.

3.2.6 Space Integrating Correlator Experimental Results

3.2.6.1 Incoherent mode

In the incoherent mode, the frequency plane elimination of all but two diffracted orders, which was the scheme used in the time integrating correlator, cannot be used. Such orders are not separated in the frequency plane since the input radiation is directed in a wide range of angles due to its incoherent nature. An alternative scheme is to convert the optical phase modulation to amplitude modulation in the object plane. This is accomplished by the use of crossed polarizers around the delay line. Then in the absence of acoustic stress, the polarizers cause optical extinction (in the case of an extreme adjustment). In the presence of stress, the optical material becomes birefringent, which alters the polarization state and results in the passage of light through the second polarizer. The result is an amplitude pattern of light which has as a factor the acoustic amplitude function in the delay line.

A calculation shows that a positive signal-to-quantum noise performance should be obtainable with this configuration. In the experiment, no signal could be recovered, even with the achievement of considerable integration gain, using a spectrum analyzer on the output waveform.

It is felt that this lack of output is due to a combination of non-optimum modulation of the delay line, and poor registration between acoustic wavefronts and light rays. This misregistration may be attributable to curvature in the acoustic wavefronts.

3.2.6.2 Coherent Experiment

As an alternative to the foregoing experiment a coherent space-integrating correlator was implemented. This merely requires the substitution of coherent (laser) illumination for the incoherent source behind the input photographic grating transparency. This now causes separation of diffraction orders in the spatial frequency plane as in the first time-integrating section, so that the use of crossed polarizers is not required.

A Spectra-Physics Model 125A 60 mw laser was used. Its 1 mm diameter beam was focussed into a 25 micron pinhole and the resulting expanded beam was collimated with a 162 mm lens. This beam was used to illuminate the grating transparency.

The resulting spatial pattern was imaged on a second delay line, which was a 60 MHz fused quartz line. With a 15 mm interaction length, this line is again a Bragg line. The light from this delay line was collected by a final lens and delivered to an avalanche silicon photodiode. In Figure 3-7 is shown a series of photographs of the r.f. sine wave recovered from the detector. The oscilloscope was synchronized to the r.f. wave applied to the delay line. Each of the traces shown represents a different positional setting of the input grating, in which the grating was moved a physical distance corresponding to 1/3 spatial cycle. The proper corresponding change in temporal phase is demonstrated in Figure 3-7.

3.2.6.3 Summary

Experimental results have been shown which demonstrate the successful operation of a time-integrating correlator, at a wavelength of 830 nm. The operation of a coherent second section correlator, which is required for an adaptive system is demonstrated at 633 nm. The required marriage of the two

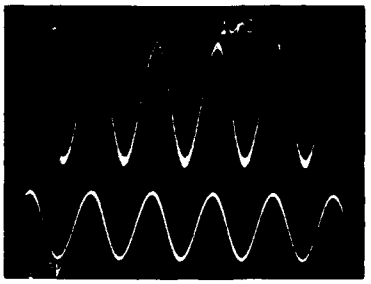

0° grating positional phase

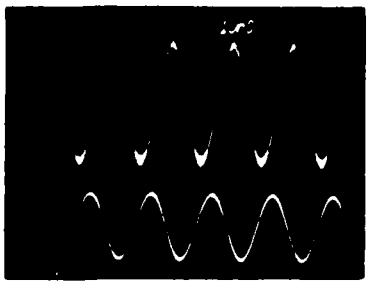

120° grating positional phase

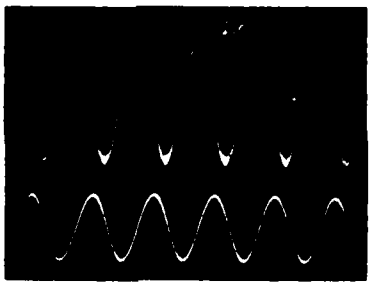

240° grating positional phase

Bottom Traces: Reference oscillator waveform.

Top Traces: Detector signals.

Figure 3-7. Time Signal Recoveries from Coherent Output Correlator for Simple R.F. Carrier

correlators has not as yet been satisfactorily accomplished, due to the poor performance of the incoherent second section. It is expected that with the addition of a coherent optical modulator, which will allow the coherent mode in the second correlator as well as the first, a complete adaptive loop can then be demonstrated.

4 ANALYSIS OF COMPONENT PERFORMANCE

4.1 DELAY LINE PERFORMANCE

4.1.1 Introduction to Bragg Diffraction

We now take up the theory of modulation of light with an AO delay line. One needs to know the amount of optical modulation achieved as a function of the total phase modulation provided by the AO line. Further, the relation between acoustic power in the AO line and the resulting phase modulation is also needed.

In evaluating the performance of diffraction of light by a delay line in the Bragg mode, a fundamental variable is the total phase shift imposed on a light ray assuming that it travels entirely through the line, perpendicular to the direction of acoustic propagation, as shown in Figure 4-1.

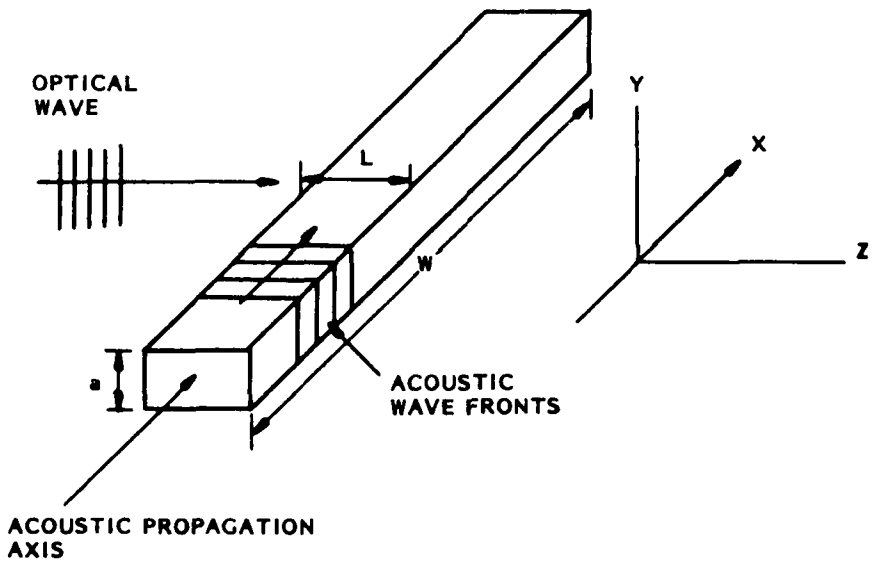

Figure 4-1. A-O Delay Line as Phase Modulator of Perpendicular Light Beam

We define this total phase shift according to the value of the peak amplitude on the positive and negative swings of the sinusoidal variation:

$$\phi_m = \Delta n \cdot \frac{2\pi L}{\lambda} \qquad (4\text{-}1)$$

where Δn is the peak magnitude of the optical index change caused by the acoustic wave, and L is the AO interaction length as shown in Figure 4-1. The variation of ϕ at any point along the delay line is given by

$$\phi = \phi_o + \phi_m \sin 2\pi \left(\frac{x \pm v_a t}{\Lambda}\right) \qquad (4\text{-}2)$$

where Λ = acoustic wavelength.

In Bragg diffraction, incoming light rays do not follow an acoustic wavefront, but rather are correctly oriented at the "Bragg angle", which is given by

$$\theta_B = \sin^{-1} \frac{\lambda}{2\Lambda} \qquad (4\text{-}3)$$

In this position, the diffracted first order is oriented at $-\theta_B$, and the geometry is then such that there is a continuous coherent reinforcement of one wave by the other. This is caused by the volume grating pattern corresponding to the index variation induced by the acoustic wave. This geometry is illustrated in Figure 4-6.

4.1.2 Photo-Elastic Effect.

To understand this type of acoustic modulation one must consider the relation between mechanical stress, strain, and the resulting optical photo-elastic effect. The optical behavior of a stressed solid is very similar to the behavior of the optical behavior experienced in a crystal [9], [10].

In the general case, i.e. anisotropic crystals, the optical behavior varies between the principal axes of such a crystal. The most general crystal is the biaxial crystal in which the behavior is different between three mutually perpendicular principal axes. A somewhat simpler case is the uniaxial crystal in which one axis behaves differently than the other two, which are isotropic between themselves. The simplest case is the isotropic crystal in which behavior is uniform in any direction.

The uniaxial case is of the most interest to us, since when an isotropic material is stressed with a simple compressive (or tensile) stress in some direction, the isotropic material becomes uniaxial in its optical behavior, with its principle uniquely altered axis (sometimes referred to as the extraordinary index axis) coincident with the stress vector.

In a uniaxial crystal, it is convenient to define an ellipsoid of wave normals, or "optical indicatrix". This is given by the equation: [9]

$$\frac{D_x^2}{\epsilon_x} + \frac{D_y^2}{\epsilon_y} + \frac{D_z^2}{\epsilon_z} = \vec{E} \cdot \vec{D} = \text{Electric Energy Density} \qquad (4\text{-}4)$$

where D_x, D_y, and D_z are electric displacement, or "D" vectors. This is the equation of an ellipsoid, and, it can be shown from the Maxwell theory, that the principal directions of the D-vector associated with any wave normal can be obtained from the construction in Figure 4-2.

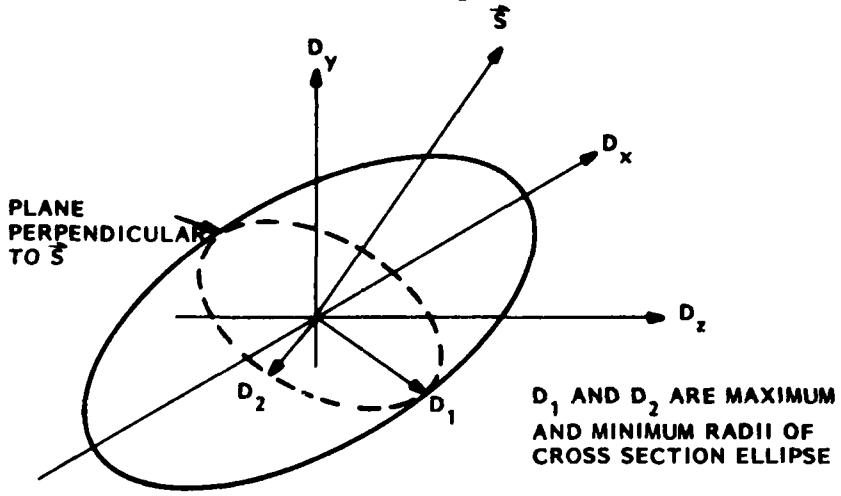

Figure 4-2. Principal Axes of D-Vector as Obtained from Ellipsoid of Wave Normals

For any optical wave normal $\vec{S}$ (not necessarily the ray direction) the origin plane perpendicular to $\vec{S}$ intersects the ellipsoid of wave normals in a plane ellipse, shown in dotted lines in Figure 4-2. The minimum and maximum radii of this ellipse, i.e. the principal axes, define the two perpendicular principal D-vectors associated with $\vec{S}$.

In particular, if $\vec{S}$ is coincident with one of the principal axes, say the z-axis for example, the two D-vectors associated with $\vec{S}$ are the other two principal axes, the x- and y-axes in this case. Thus in this case of principal stress-optical alignment, the D and E vectors are colinear, and are related by ϵ_x in the x-direction and ϵ_y in the y-direction. It follows that the phase velocities v_p of the two waves propagating in the z-direction are $1/\sqrt{\mu\epsilon_x}$ for $\vec{E}$ in the x-direction, and $1/\sqrt{\mu\epsilon_y}$ for E in the y-direction.

The appropriate axis is selected from the ellipsoid according to the E-vector, since in a dielectric $\mu = \mu_o$, $B = \mu_o H$ in all directions. Only the relation of $\vec{E}$ and $\vec{D}$ are affected by the changes in the dielectric constant ε.

Thus, referring to Figure 4-1 if an incident ray traveling in the z-direction is incident on a medium stressed (or strained) in the x-direction, two results are possible.

1) the electric vector is oriented along the y-axis, in which case

$$v_p = \frac{1}{\sqrt{\mu_o \varepsilon_{ORD}}} \qquad (4\text{-}5)$$

where $\varepsilon_{ORD} = \varepsilon_y = \varepsilon_z$

and the ray is called the "ordinary ray".

2) the electric vector is oriented along the x-axis in which case

$$v_p = \frac{1}{\sqrt{\mu_o \varepsilon_x}} \qquad (4\text{-}6)$$

and the ray is called the "extraordinary ray".

The extraordinary ray thus has a different velocity than with rays oriented with E-vectors perpendicular to the x-axis.

In the case of a general ray direction with a general E-orientation, a uniaxial medium refracts two rays, according to the theory previously described. The travel of these two rays are in slightly different directions in this general case. The important consequence to us is that the phase delay of the two rays differ, that of the ordinary ray and that of the extraordinary ray.

The equation of the ellipsoid of wave normals, equation (4-4), is written for the principal optical axes and the x,y,z coordinate system being co-aligned. The coefficients of this equation are $a_x = 1/\varepsilon_x$, $a_y = 1/\varepsilon_y$, and $a_z = 1/\varepsilon_z$. In the case of a biaxial crystal in a general orientation, with a general mechanical stress applied, the change in the a_{ij}'s = $1/\varepsilon_{ij}$'s is given by

$$\Delta a_{ij} = q_{ijkl}\, T_{kl} \qquad \text{(The RH side is summed over k,l)} \qquad (4\text{-}7)$$

where

Δa_{ij} = dielectric impermeability tensor (2nd rank)

T_{kl} = stress tensor (2nd rank)

q_{ijkl} = stress-optical tensor (4th rank)

Each index covers three spatial dimensions. Thus there are nine terms in Δa_{ij} and T_{kl}, and 81 terms in q_{ijkl}.

However, the cross terms of Δa and T are symmetric, and so the 9 terms of each reduces to six. The terms of T_{kl}, for example, are given by

$$T_{xx},\ T_{yy},\ T_{zz},\ T_{yz},\ T_{xz},\ T_{xy}.$$

q_{ijkl} now reduces to 36 independent terms.

In the case of a material which is isotropic when unstressed, it can be shown that this reduces to 2 independent coefficients. We then have, by orienting the coordinates along the principal axes of the stress tensor, and thereby eliminating the cross (shear) terms: [9]

$$\left.\begin{aligned} \Delta a_x &= q_{11}\, T_{xx} + q_{12}\, T_{yy} + q_{12}\, T_{zz} \\ \Delta a_y &= q_{12}\, T_{xx} + q_{11}\, T_{yy} + q_{12}\, T_{zz} \\ \Delta a_z &= q_{12}\, T_{xx} + q_{12}\, T_{yy} + q_{11}\, T_{zz} \end{aligned}\right\} \qquad (4\text{-}8)$$

Coefficients can also be defined which relate the change of $a_i = 1/\epsilon_i$ to the component of strain instead of stress. Thus we have:

s_{ii} = Strain in ith coordinate

$$\left.\begin{aligned} \Delta a_x &= p_{11}\, s_{xx} + p_{12}\, s_{yy} + p_{12}\, s_{zz} \\ \Delta a_y &= p_{12}\, s_{xx} + p_{11}\, s_{yy} + p_{12}\, s_{zz} \\ \Delta a_z &= p_{12}\, s_{xx} + p_{12}\, s_{yy} + p_{11}\, s_{zz} \end{aligned}\right\} \qquad (4\text{-}9)$$

Referring to Figure 4-3 we now consider the special simple case which is of primary interest to us here. If the optical wave is propagating in the z-direction, in an isotropic medium which is stressed in the x-direction, then the medium will act like a uniaxial crystal with the optical axis, (direction of extraordinary index of refraction) in the x-direction.

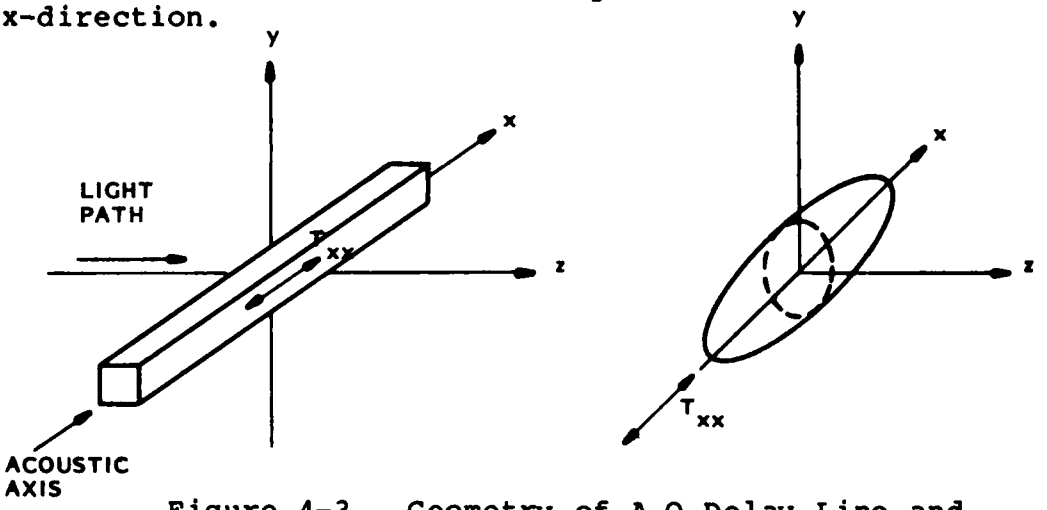

Figure 4-3. Geometry of A-O Delay Line and Longitudinal Stress, T_{xx}, and Corresponding Ellipsoid of Wave Normals

If a longitudinal acoustic wave is traveling in the x-direction, this will cause x-oriented stress, alternating between compression and dilation according to the acoustic wavefronts.

It can be shown that in most cases when an isotropic material is under dilatory or tensile stress, it behaves like a "positive" uniaxial crystal, such as crystalline quartz, and when it is in compressive stress, it behaves like a "negative" uniaxial crystal such as felspar.

A positive crystal has an ellipsoid of wave normals or indicatrix similar in shape to that shown in Figure 4-3, in which the index along the optical x-axis n_e is larger than along the other axes (y or z) which is n_o. Hence a wave in which the electric vector is aligned along the x-axis will undergo more phase delay than a wave in which the E-vector is pointed in the y-direction, in the case of tensile stress. Thus in tension the E_x wave will be retarded with respect to the E_y wave.

Referring to the first two of equations (4-9), and remembering that the a's refer to $1/\varepsilon = 1/n^2$, we see that in tension $(\Delta a_x - \Delta a_y)$ is negative (i.e. $\Delta n_x > \Delta n_y$) for tensile stress in the x-direction. For only x-strain these equations reduce to:

$$\Delta a_x = p_{11}\, s_{xx}$$

$$\Delta a_y = p_{12}\, s_{xx} \qquad (4\text{-}10)$$

$$(\Delta a_x - \Delta a_y) = (p_{11} - p_{12})\, s_{xx}$$

Now, the general effect of tension is to cause a lower molecular density, which lowers the index of refraction, raising the corresponding a coefficient. Thus as defined in (4-9), the p coefficients are positive if s_{xx} represents tensile, rather than compressive strain. If s_{xx} is thus positive for tension, $\Delta a_x - \Delta a_y$ is negative for tension, and the p-coefficients are positive, then we conclude from (4-10) that the value of p_{12} is larger than p_{11}. The p_{12} coefficient relates optical behavior of a wave in which the E-vector is parallel to the y-axis, with strain in the x-direction. This is an "ordinary" wave (the extraordinary index is coaligned with the stress). The p_{11} coefficient, by like reasoning, treats the "extraordinary ray". Thus we conclude that the phase advance (retardation) for a tensile (compressive) stress is greater for the ordinary ray than for the extraordinary ray.

This conclusion is verified by the example of "stress-optical coefficients" associated with fused quartz, which are: [10] [11]

$$C_1 = -.65$$

$$C_2 = -4.2$$

The stress-optical coefficients relate index change rather than the a-coefficients directly to stress. They are like the q's of equations (4-8) in the sense that they are based on stress rather than strain. Thus:

$$\Delta n_e = C_1 T$$

$$\Delta n_o = C_2 T \qquad (4\text{-}11)$$

The coefficient $C_1 - C_2$ is positive, and so we see that in the condition of tensile stress, in an isotropic medium, n_e is larger than n_o, a condition of a positive uniaxial crystal.

The quantity $(C_1 - C_2)$ is called the relative stress-optical coefficient. By multiplying any of the C's by the modulus of elasticity for pure extension, E_a, the strain-optical coefficients, S_1 and S_2 which relate index change to strain can be obtained.

The value of E_a which is used in these calculations pertains to ultrasonic wavefronts, in which the lateral dimension of the wavefront is many wavelengths. Under these conditions a plane compression is not accompanied by lateral expansion (governed by Poisson's ratio). This is called the bulk modulus, and is sometimes denoted as k*. In terms of the Lame' elastic moduli, μ (shearing modulus) and λ, E_a (or k) is given as $\lambda + 2\mu$ whereas Young's modulus for unconstrained lateral dimensions is given by [12]

$$\mu \left(\frac{3\lambda + 2\mu}{\lambda + \mu}\right) \quad .$$

In elasticity theory, λ accounts for volumetric change, and μ for shearing effects. In fact, μ is the modulus of shear commonly denoted by engineers as G. In the case of pure extension, with no lateral strain, the extension is equivalent to 2 shears equal to the longitudinal strain s_{xx} at 45°, one in the x-y plane, and one in the x-z plane, and a volume change equivalent to the longitudinal strain s_x. Thus the total modulus is given by $\lambda + 2\mu$.

From equation (4-4), and the definition of index of refraction $n = \sqrt{\epsilon}$, ϵ is the relative dielectric constant, the Δa_i's can be related to the Δn's as follows:

Since

$$a_i = \frac{1}{\epsilon_i} = \frac{1}{n_i^2} \qquad (4\text{-}12)$$

we have:

$$\Delta a_i = \frac{da_i}{dn_i} \Delta n_i = \frac{-2}{n_i^3} \Delta n_i$$

$$\Delta n_i = \frac{-n_i^3}{2} \Delta a_i \qquad (4\text{-}13)$$

Where the change Δa is related to strain by p, and Δa is related to stress by q, we have defined coefficients S and C which relate the change in index of refraction Δn to strain, s, and stress, T respectively.

Hence:

$$\left.\begin{aligned} S_i &= -\frac{n_i^3}{2} p_i \\ C_i &= -\frac{n_i^3}{2} q_i \end{aligned}\right\} \qquad (4\text{-}14)$$

The interrelations between the p's, q's, C's, and S's are thus found to be as follows:

TABLE III. CONVERSIONS BETWEEN PHOTO-ELASTIC PARAMETERS

	p_i	q_i	S_i	C_i
to: p_i	1	E_a	$-\frac{2}{n_i^3}$	$-\frac{2E_a}{n_i^3}$
q_i	$\frac{1}{E_a}$	1	$-\frac{2}{E_a n_i^3}$	$-\frac{2}{n_i^3}$
S_i	$-\frac{n_i^3}{2}$	$-\frac{n_i^3 E_a}{2}$	1	E_a
C_i	$-\frac{n_i^3}{2\ E_a}$	$-\frac{n_i^3}{2}$	$\frac{1}{E_a}$	1

Multiply by entry in table.

$$\Delta a_i = p_i s_{ii}$$

$$\Delta a_i = q_i T_{ii}$$

$$\Delta n_i = S_i s_{ii}$$

$$\Delta n_i = C_i T_{ii}$$

4.1.3 Acousto-Optic Interaction

The preceding theory relates the changes in the dielectric parameters, and specifically the index of refraction, in a solid material to the stress and strain pattern induced in that solid by an acoustic wave. The next issue is to summarize the resulting optical diffraction behavior in the Raman-Nath and Bragg modes which is caused by the spatially periodic dielectric variations that accompany such an acoustic wave.

4.1.3.1 Raman Nath Diffraction

Assume that an acoustic line is thin enough in the direction of optical propagation so that a light ray essentially stays registered with an acoustic wavefront during its entire transit through the delay line. The physical transit length which is involved has been denoted by L in the previous discussion. The optical behavior of this configuration is commonly referred to as Raman-Nath diffraction. In this case, a differential phase shift is imposed on the optical ray, ϕ_m, which is a coherent accumulation of phase shift caused by the index of refraction change over the interaction length L. Thus the value of the index change Δn which is experienced by the ray is constant over L. The resulting phase shift is then given by $\phi_m = \Delta n\ k\ L$

$$\phi_m = \Delta n\ k\ L \qquad (4\text{-}15)$$

where

k = free space wave number = $2\pi/\lambda_o$.

If the acoustic propagation is along the x-axis, the spatial index variation is then in terms of x. If we assume that a simple cw sinusoidal carrier exists of frequency $\omega_a = 2\pi\ v_a/\Lambda$, resulting in a spatial variation of $n = n_o + \Delta n \cos 2\pi\ x/\Lambda$, then this spatial variation will be imposed as a spatial phase modulation on a collimated input beam passing through the delay line. If this input light beam is given functionally as $E_o\ e^{j(kz-\omega_o t)}$, where the E-vector is assumed to be aligned in the x-y plane, and ω_o is the optical frequency, the light emerging from the delay line will be given by:

$$E = E_o\ e^{\left[j(kz-\omega_o t) + jkL\ \Delta n \cos 2\pi \frac{(x-v_a t)}{\Lambda} \right]} \qquad (4\text{-}16)$$

We now note that $e^{j\phi_m \cos\theta}$ can be mathematically expanded into the following series:

$$e^{j\phi_m \cos\theta} = \sum_{n=-\infty}^{+\infty} j^n J_n(\phi_m)\, e^{jn\theta} \qquad (4\text{-}17)$$

Using this expansion, we find that the optical wave emerging from the delay line can then be described by the following expression: [13]

$$E = E_o \sum_{n=-\infty}^{+\infty} j^n J_n(\phi_m) e^{\left[j(kz-\omega t) + j2\pi n \left(\frac{x-v_a t}{\Lambda}\right)\right]} \qquad (4\text{-}18)$$

Each term in the summation corresponds to an optical diffracted order. In particular, the first order of diffraction has a coherent amplitude which is given by:

$$E_1 = J_1(kL\Delta n) \qquad (4\text{-}19)$$

The behavior described by these expressions is Raman-Nath diffraction, and is for relatively thin lines. For Raman-Nath theory to apply, the diffracted ray must stay essentially registered with the acoustic wavefront, and not cross over to adjacent wavefronts. The situation is shown in Figure 4-4.

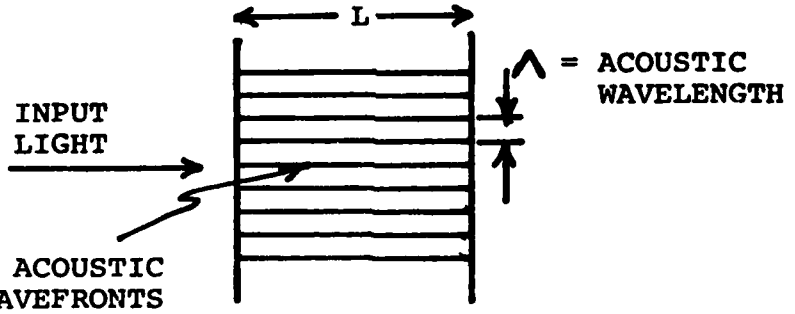

Figure 4-4. Registration of Light Rays with Acoustic Wavefronts

The angle between the zero order and the first diffracted order is given by $\lambda/n\Lambda$. Hence the linear spread between the two orders after passing through L is $\lambda L/n\Lambda$. This should not exceed 1/4 acoustic wavelength. Hence for Raman-Nath operation:

$$\frac{\lambda L}{n\Lambda} < \frac{\Lambda}{4} \Rightarrow L < \frac{n\Lambda^2}{4\lambda} \qquad (4\text{-}20)$$

For small values of ϕ_m, the first order Bessel function can be approximated by 1/2 its argument. Thus:

$$J_1(\phi_m) \cong \frac{\phi_m}{2} \Rightarrow E_1 \cong \frac{kL\Delta n}{2} \qquad (4\text{-}21)$$

From this we see that the coherent amplitude of the first diffracted order is linearly related to the phase modulation.

Thus in Raman Nath diffraction an array of optical orders are obtained, which are symmetrical around the zero order, with amplitudes given by equation (4-17). The strength of the orders depends on the peak phase modulation imparted to the optical beam passing through the AO line. The value of the 0^{th}, 1^{st} and 2^{nd} orders are diagrammed as a function of the phase modulation ϕ_m in Figure 4-5. Here again it is seen that the first order is linear with the phase modulation for small signal.

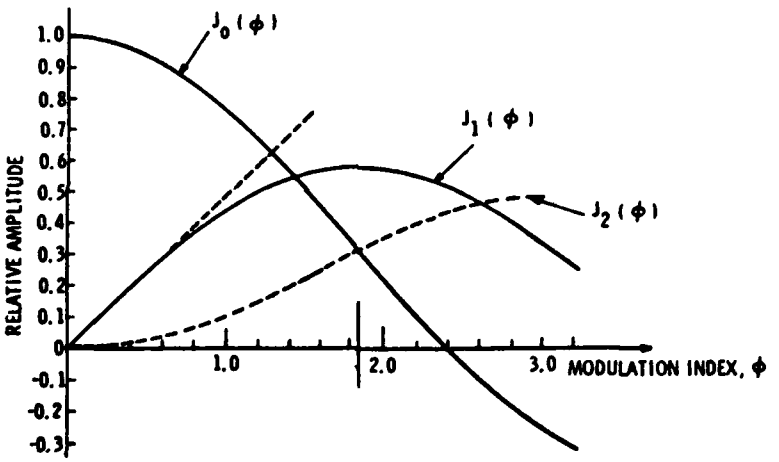

Figure 4-5. Amplitudes of Diffracted Optical Orders

4.1.3.2 Derivation of Bragg Diffraction from Raman-Nath Concepts

We now turn to the case of Bragg diffraction, in which the modulating medium, i.e. the delay line, is so thick that the diffracted orders traverse many acoustic wavefronts. As mentioned before, in this case strong first order diffraction is obtained if the incoming beam is oriented at the Bragg angle, $\lambda/2\Lambda$, instead of exactly perpendicular. With this orientation, one first order is continually reinforced by the diffraction effect throughout the depth of the line. In

other words, the interference between successive diffraction contributions as one proceeds through the interaction length is coherently reconstructive. The interference effect for the other orders is destructive, and hence all other orders are greatly attenuated. For a strong enough signal and resulting strong phase modulation essentially 100% of the input beam can be diffracted into the first order. The situation is pictured in Figure 4-6.

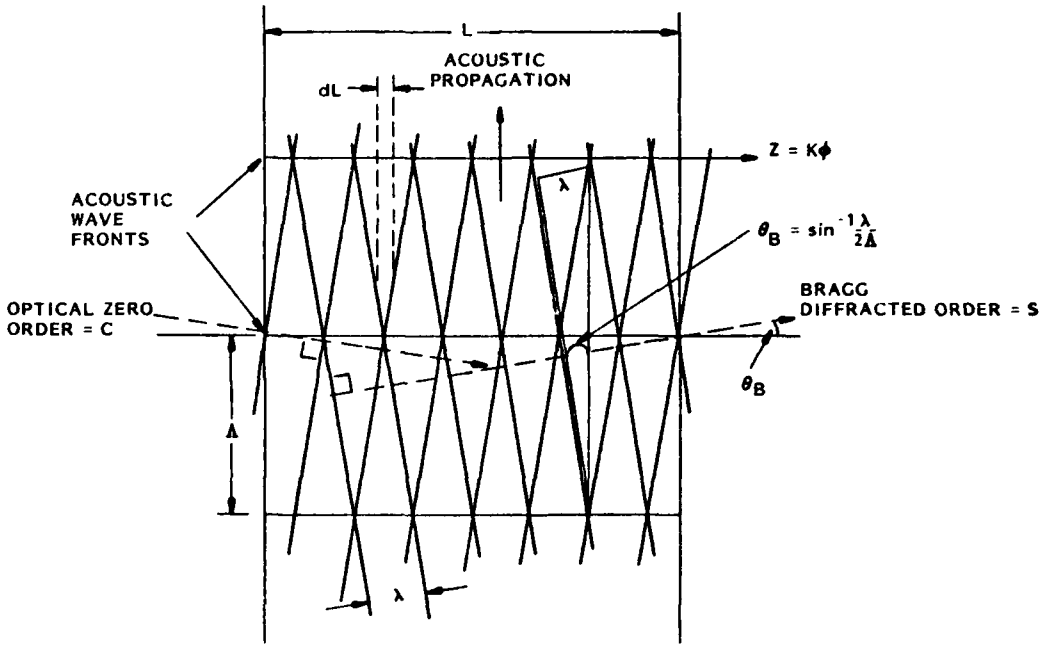

Figure 4-6. Geometry of Bragg Diffraction Showing Alignment of Acoustic and Optical Wavefronts

In Figure 4-6 we indicate a thin slice of delay line medium with width dL. When the strong zero order impinges on this thin slice, Raman-Nath diffraction will occur according to the preceding theory. The resulting array of orders will appear symmetrically around the zero order. Let the amplitude of the zero order be denoted by c (for carrier), and the first order denoted by s (for sideband). The following argument is taken from reference [14].

When the zero order with amplitude c passes through the thin phase grating, the complex amplitude of the emerging wave is given by

$$c\, e^{id\phi \sin \frac{2\pi x}{\Lambda}} \cong c\left(1 + id\phi \sin \frac{2\pi x}{\Lambda}\right)$$

$$\cong c + \frac{c}{2} d\phi\, e^{i \frac{2\pi x}{\Lambda}} - \frac{c}{2} d\phi\, e^{-i \frac{2\pi x}{\Lambda}} \qquad (4\text{-}22)$$

This expression accounts for Raman-Nath diffraction from the thin grating, in which the phase modulation involves a small angle $d\phi = k\, dL\, \Delta n$. The last two terms in the above expression represent the positive and negative first optical orders. Since we assume that only the positive first order has reconstructive interference, this order will build up through successive thicknesses dL, and the other order will have destructive interference and will not appear to any significant degree in the emerging wave. This constitutes the Bragg effect. The differential buildup of the diffracted order s can be expressed in terms of the differential accumulation of phase shift $d\phi$ from equation (4-22) as

$$ds = \frac{c}{2} d\phi \Rightarrow \frac{ds}{d\phi} = \frac{c}{2} \qquad (4\text{-}23)$$

In a like manner, when the diffracted order s builds up to a significant amplitude, it will act like a new zero order and will, by Bragg diffraction, create a sideband which is oriented exactly with the original zero order, and will coherently combine with the original zero order. This argument does not answer the question of the phase relation between the original zero order c, and the sideband of the diffracted order which is combining with c. This problem is resolved indirectly by appealing to the assumption that all the diffraction in the Bragg mode goes into the one first order, and then back again into the zero order, these two orders being symmetrically oriented with respect to the acoustic beam at

$\pm\theta_B$, the Bragg angle (equation 4-3). Under this assumption, all the energy associated with the zero order entering the interaction region at the left hand side of the interaction region must equal the sum of the energies of the two orders at any arbitrary point within the line, or at the plane of emergence on the right hand side as shown in Figure 4-6. Thus we have:

$$c^2 + s^2 = c_o^2 \tag{4-24}$$

where

c_o = amplitude of incident zero order light beam.

Differentiating with respect to ϕ, we have:

$$2c \frac{dc}{d\phi} + 2s \frac{ds}{d\phi} = 0$$

$$\frac{dc}{d\phi} = -\frac{s}{c} \cdot \frac{ds}{d\phi} = -\frac{s}{2} \tag{4-25}$$

Equations (4-23) and (4-25) can be separated into two homogeneous equations in $\underline{c}$ and $\underline{s}$ by the differentation by $d/d\phi$ producing

$$\frac{d^2c}{d\phi^2} = -\frac{c}{4} \quad \text{and} \quad \frac{d^2s}{d\phi^2} = -\frac{s}{4} \tag{4-26}$$

The solutions to these equation are:

$$c = c_o \cos \frac{\phi}{2}$$

$$s = c_o \sin \frac{\phi}{2} \tag{4-27}$$

The relative intensity of the diffracted order to the incident intensity is:

$$\frac{I}{I_o} = \frac{s^2}{c_o^2} = \sin^2 \frac{\phi}{2} \tag{4-28}$$

4.1.4 Imaging with Bragg Diffraction

The two orders developed by the Bragg diffraction in the delay line appear collimated and at a relative mutual angle corresponding to the acoustic spatial frequency in the image plane. Thus the relative spatial phase of the two orders

varies at a spatial rate which is the acoustic spatial frequency. The coherent sum of the two orders can then be expressed as:

$$\text{sum} = c + jse^{j\theta_a} \tag{4-29}$$

$$\theta_a = 2\pi \frac{(x - v_a t)}{\Lambda} + \theta_a$$

$$\theta_a = \text{acoustic signal phase} \tag{4-30}$$

The light waves are detected by the image intensifier (or other detecting device) which can be adequately modeled as a square law detector. The light intensity is given as:

$$I = \frac{1}{2}\left(c + jse^{j\theta_a}\right)\left(c^* + (js)^* e^{-j\theta_a}\right) \tag{4-31}$$

For this argument, we assume that c and s are the real functions derived previously, equation (4-27). Thus we have

$$I = \frac{1}{2}\left(cc^* + ss^* + jc^*s\, e^{j\theta_a} - jcs^*\, e^{-j\theta_a}\right)$$

$$= \frac{c_o^2}{2}\left(1 + 2\cos\frac{\phi_m}{2}\sin\frac{\phi_m}{2}\sin\theta_a\right)$$

Hence:

$$\boxed{\frac{I}{c_o^2} = \frac{1 + \sin\phi_m \sin\theta_a}{2}} \tag{4-32}$$

In the above expression, the presence of the factor sin θ_a tells us that the intensity varies as a linear function of the acoustic carrier, and this variation or carrier is multiplied by sin ϕ_m. The function ϕ_m is here regarded as the signal amplitude (total phase shift across the Bragg line due to the photoelastic effect). If ϕ_m is appreciably less than 1 radian, the modulation amplitude becomes linear with signal amplitude as desired. This variation appears around a bias term equal to 1/2.

The maximum and minimum values of I occur at values of θ_a equal to $(2n + 1)\,\pi/2$ where $\sin\theta_a = \pm 1$. Thus:

$$I_{max} = \frac{1 + \sin\phi_m}{2}$$

$$I_{min} = \frac{1 - \sin\phi_m}{2} \qquad (4\text{-}33)$$

The usual definition of intensity contrast ratio is thus given as:

$$\text{Contrast Ratio} = \frac{I_{max} - I_{min}}{I_{max} + I_{min}} = \sin\phi_m \qquad (4\text{-}34)$$

so that the contrast ratio is also a linear function of ϕ_m for small values of ϕ_m.

4.1.5 Acoustic Wave Propagation

We now address the relation between acoustic power and the resulting phase modulation. For the simplest case, let us assume that a longitudinal acoustic wave exists in the delay line, traveling in the x-direction, as shown in Figure 4-7. A thin slice of medium is indicated with width dx. The

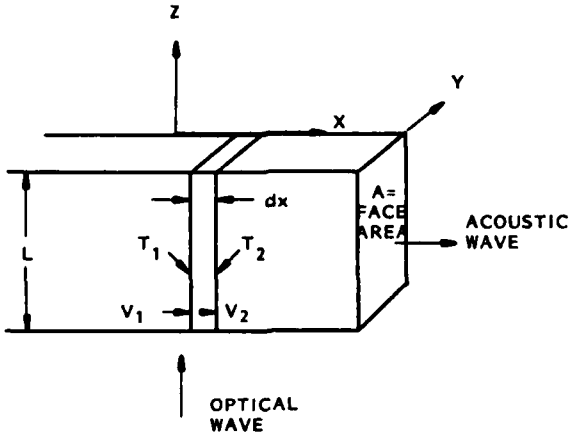

Figure 4-7. Acoustic Longitudinal Wave Propagation Characterized by Stress, T, and Particle Velocity, v on Faces of Thin Slice of Delay Medium

acoustic wave is now characterized by the acoustic sinusoidal pressure on the plane boundaries of the slice dx, and the particle velocity varying sinusoidally in the x direction. The differential force on the slice will accelerate the particles lying within. Thus we can write:

$$T_2 - T_1 = A\,dx\,\frac{\partial T_{xx}}{\partial x} = \rho\,A\,dx\,\frac{\partial v}{\partial t}$$

$$\frac{\partial T_{xx}}{\partial x} = \rho\,\frac{\partial v}{\partial t} \qquad (4\text{-}35)$$

where

T_{xx} = acoustic pressure (stress)

T_1, T_2 = two values of pressure on the boundaries of dx

ρ = density of medium

v = particle velocity

A = face area of slice.

Similarly, we argue that a space gradient in velocity will cause a time rate of change of strain, s. We have:

$$v_2 - v_1 = \frac{\partial v}{\partial x}\,dx = \frac{\partial s}{\partial t}\,dx = \frac{\partial}{\partial t}\left(\frac{T_{xx}}{E_a}\right)dx$$

$$\frac{\partial v}{\partial x} = \frac{1}{E_a}\,\frac{\partial T_{xx}}{\partial t} \qquad (4\text{-}36)$$

where E_a is the appropriate acoustic modulus of elasticity, given by the linear combination of Lame' coefficients $\lambda + 2\mu$ as explained in Section 4.1.2.

Combining equations (4-35) and (4-36) we have the second order equation:

$$\frac{\partial^2 T_{xx}}{(\partial x)^2} = \rho\,\frac{\partial^2 v}{\partial t\,\partial x} = \frac{\rho}{E_a}\,\frac{\partial^2 T_{xx}}{(\partial t)^2} \qquad (4\text{-}37)$$

The most general solution to this equation is

$$T_{xx} \equiv T_{xx}\left(x \pm v_a t\right) \tag{4-38}$$

where

$$\rho v_a^2 = E_a \tag{4-39}$$

4.1.6 Acoustic Energy and Power

The mechanical energy density stored in any microscopic region of the medium is given by 1/2 the product of acoustic pressure and strain. Thus:

$$w_a = \text{Energy Density} = \frac{T_m \; s_m}{2} = \frac{E_a \; s_m^2}{2} \tag{4-40}$$

T_m = Peak value of T_{xx}

s_m = Peak value of strain (s_{xx})

The acoustic power is the time rate of flow of acoustic energy. Thus the acoustic intensity (power density) is the acoustic velocity times the energy density. The result is expanded using (4-39) and (4-40):

$$I_a = w_a \; v_a = \frac{1}{2} \; s_m^2 \; \rho \; v_a^3 \tag{4-41}$$

From equation (4-14) and Table III we have:

$$\Delta n_i = S_i \; s_m = \frac{p_i \; n_i^3}{2} \; s_m \tag{4-42}$$

Referring to equation (4-1) we have a relation between the peak phase shift and the peak shift in index of refraction. Combining this with the above produces:

$$\phi_m = \frac{2\pi L}{\lambda} \; \frac{p_i \; n_i^3}{2} \; s_m \tag{4-43}$$

$$= \pi \sqrt{\frac{2L^2}{\lambda^2} \left(\frac{p^2 \; n_i^6}{\rho \; v_a^3}\right)} \; I_a \tag{4-44}$$

All of the quantities contained within the brackets of the above are parameters of the medium material. These are

popularly combined into a material "figure of merit." This particular mix of parameter values is known as M_2. If, in the above derivation, instead of solving for ϕ_m, we solve for the acoustic intensity I_a, there results: [14]

$$I_a = \frac{P_a}{A} = \frac{1}{2} \times 4(\Delta n_i)^2 \times \frac{\rho\, v_a^3}{p_i^2\, n_i^6}$$

$$\frac{P_A}{A} = 2\left(\frac{\phi_m}{2\pi}\right)^2 \frac{\lambda^2}{L^2 M_2} \qquad (4\text{-}45)$$

$$M_2 = \frac{p_i^2\, n_i^6}{\rho\, v_a^3}$$

It will be recalled that from (4-34),

$$\phi_m = \sin^{-1}(\text{contrast ratio}) \qquad (4\text{-}46)$$

so that for imaging with Bragg diffraction, ϕ_m may be taken as the contrast ratio for values of this quantity substantially less than unity.

4.1.7 Power Calculations for Various Optimized Geometries

To achieve minimum power, for a given diffraction efficiency, we minimize the expression for P_A. This is achieved by maximizing L and minimizing a. There is no real limitation for a single acoustic frequency and an unlimited incident light power. However, a more sensible constraint results, if a definite acoustic bandwidth Δf is considered. Such a bandwidth implies a spatial element length along the acoustic wave, (along the y-direction in Figure 4-3) given as

$$b = \frac{v_a}{\Delta f} \qquad \Delta f = \text{acoustic bandwidth} \qquad (4\text{-}47)$$

Assume the acoustic beam is roughly distributed over a rectangular cross section (corresponding to a rectangular acoustic transducer), of dimensions a in the y-direction, and L in the z-direction (interaction length). This results in an acoustic cross-section area of aL, and equation (4-45) can be written:

$$P_a = 2\left(\frac{\phi_m}{2\pi}\right)^2 \frac{\lambda^2 a}{L M_2} \qquad (4\text{-}48)$$

The next question involves the permissible geometry of the Bragg diffractor. First, there is a limit to the length of the interaction region, i.e. the dimension L in the z-direction. This is because the incoming light and the acoustic beam have to be related by the Bragg angle, which from equation (4-3) is seen to be sensitive to the acoustic frequency. If a wide-band acoustic frequency is being used for diffraction, this implies an angular spread in the orientation angle. This spread of angle must be within the range of Bragg compatibility. A convenient way of looking at this problem is to consider the far-field divergence of both the optical angular spectrum diffracted by the acoustic signal, and the far-field acoustic divergence of the acoustic beam. For valid Bragg diffraction of all the frequency components of the signal in the acoustic beam, the far field divergence of the acoustic beam must be at least as large as the divergence of the optical diffracted beam. Thus we have:

$$\Delta\theta_B = \text{Divergence of the diffracted optical beam} = \frac{\lambda}{nb} \qquad (4\text{-}49)$$

where b = spatial dimension (in x) of acoustic resolution element as limited by the acoustic bandwidth
$= v_a/\Delta f$

Δf = acoustic bandwidth.

Let the far field divergence of the acoustic beam, as limited by the transmitting aperture dimension L, which is also the interaction length, be denoted as $\Delta\theta_A = \Lambda/L$.

Hence:

$$\Delta\theta_B < \Delta\theta_A \Rightarrow \frac{\lambda}{nb} < \frac{\Lambda}{L}$$

$$L < \frac{nb\Lambda}{\lambda} = \frac{n\, v_a^2}{\lambda\, \Delta f\, f_o} \qquad (4\text{-}50)$$

The next geometrical constraint to consider is the vertical extent of the acoustic beam, a. This must be large enough so that no appreciable acoustic diffraction spreading of the beam occurs in this direction, which would cause curved wavefronts, and would cause the acoustic beam to intercept the side-walls of the delay line. Thus, in essence, we want the spreading to be less than the original size of the acoustic beam. Hence:

$$\text{Vertical acoustic beam spread} = \frac{\Lambda W}{a} < a \qquad (4\text{-}51)$$

$$\Rightarrow a > \sqrt{\Lambda W} = \sqrt{\Lambda\, v_a T} = v_a \sqrt{\frac{T}{f_a}} \qquad (4\text{-}52)$$

where W is the length of the delay line in the direction of acoustic propagation, and

Λ = acoustic wavelength.

Now consider the case of a simple acoustic modulator, in which no specific delay time is required. In this case the optical aperture need only subtend an acoustic resolution element, $\underline{b}$. Now equation (4-51) becomes

$$\frac{\Lambda b}{a} < a \Rightarrow a > \sqrt{b\Lambda} = \frac{v_a}{\sqrt{\Delta f\, f_a}} \qquad (4\text{-}53)$$

The relaxation of the acoustic spreading constraint now means that the optical spreading associated with $\underline{a}$ becomes the important limitation. If we demand that the optical spreading is restricted to $\underline{a}$ we have:

$$a > \sqrt{\frac{\lambda L}{n}} \quad \text{and from (4-50)} \quad a > \sqrt{b\Lambda}$$

which is the same result as (4-53).

The limitation on the ratio a/L is now given as:

$$\frac{a}{L} > \frac{\dfrac{v_a}{\sqrt{\Delta f\, f_o}}}{\dfrac{n\, v_a^2}{\lambda\, \Delta f\, f_o}} = \frac{\lambda \sqrt{\Delta f\, f_o}}{n\, v_a} \qquad (4\text{-}54)$$

where $\delta = \Delta f / f_o$ = fractional bandwidth.

Substitution of this limiting result in equation (4-48) produces the minimum acoustic power required for optimum delay line geometry,

$$P_a > 2 \left(\frac{\phi_m}{2\pi}\right)^2 \frac{\lambda^2}{M_2} \cdot \frac{\lambda \sqrt{\Delta f \, f_o}}{n \, v_a} \qquad (4\text{-}55)$$

In this expression we see that a new grouping of the material parameters appears: [14]

$$n \, v_a \, M_2 = M_3 \qquad (4\text{-}56)$$

The required acoustic power for a given amount of optical modulation is related to this new figure of merit, M_3, for the case of optimized delay line geometry. Using this notation, equation (4-55) can be written

$$\frac{P_a}{\Delta f} > 2 \left(\frac{\phi_m}{2\pi}\right)^2 \frac{\lambda^3}{M_3 \sqrt{\delta}} \qquad (4\text{-}57)$$

where

$$\delta = \frac{\Delta f}{f_o}$$

i.e., the fractional acoustic bandwidth.

It is clear that minimum drive power is achieved, for the single element acoustic modulator, when the fractional bandwidth is made its maximum value, 1. We will take this maximum value to be 1, although theoretically the value is 2 for a base-band situation. If $\delta = 1$, we have for the required power:

$$\frac{P_a}{\Delta f} > 2 \left(\frac{\phi_m}{2\pi}\right)^2 \frac{\lambda^3}{M_3} \qquad (4\text{-}58)$$

Now consider a delay line modulator in which a total delay time T is required. Equations (4-50) and (4-52) are used to evaluate the minimum value of a/L as follows:

$$\frac{a}{L} > \frac{v_a \sqrt{\frac{T}{f_o}}}{\frac{n\, v_a^2}{\lambda\, \Delta f\, f_o}} = \frac{\lambda \sqrt{\Delta f\, f_o\, T\, \Delta f}}{n\, v_a}$$

$$= \frac{\lambda\, \Delta f}{n\, v_a} \sqrt{\frac{N}{\delta}} \qquad (4\text{-}59)$$

Substituting this into equation (4-48) we have:

$$\frac{P_a}{\Delta f} > 2 \left(\frac{\phi_m}{2\pi}\right)^2 \frac{\lambda^2}{M_2} \cdot \frac{\lambda}{n\, v_a} \sqrt{\frac{N}{\delta}} = 2 \left(\frac{\phi_m}{2\pi}\right)^2 \frac{\lambda^3}{M_3} \sqrt{\frac{N}{\delta}} \qquad (4\text{-}60)$$

where δ = fractional bandwidth, as before, and

N = time-bandwidth product of delay line

$= \Delta f \cdot T$

As before, the minimum power is achieved with the maximum fractional bandwidth. Thus one should select the fractional bandwidth in due regard for the avoidance of spectral folding or aliasing in the active band. For the present experiment a fractional bandwidth of 1/6 was chosen, corresponding to a required bandwidth of 10 MHz, and a selected center acoustic frequency of 60 MHz, when using a quartz line with an acoustic velocity of 5.95 mm/sec. Alternatively, a frequency of 37 MHz was used with a flint glass line with a velocity of 3.7 mm/sec. Thus in either case a spatial frequency of 10 cycles/mm was achieved.

4.1.8 Delay Line Medium Comparisons

We will now use these results to calculate the required acoustic power level for various delay line materials. For the purposes of comparison, the maximum modulation level will be assumed, providing a contrast ratio of unity from the image intensifier, according to equation (4-46). As seen from this relation this implies a peak phase deviation of $\pi/2$. A reinforcement of this conclusion may be gained from equation (4-28). From this relation, it is seen that if the peak phase deviation is $\pi/2$, half the intensity (power) of the incoming light beam, I_o, is transferred to the

diffraction order I. With equal amplitude 1st order and zero order light beams being used for imaging of the acoustic carrier, total nulls will be developed at points of maximum interference, and amplitude doubling will be obtained at points of opposite phase relation. Thus the image varies in intensity from total blackness to maximum brightness, corresponding to 100% modulation.

Substituting $\phi_m = \pi/2$ in the expression for a simple modulator, with no total delay requirement, equation (4-57), we have $(\phi_m/2\pi)^2 = 1/16$, and

$$\frac{P_a}{\Delta f} > \frac{\lambda^3}{8M_3\sqrt{\delta}} \qquad (4\text{-}61)$$

which for a fractional bandwidth of 100% becomes

$$\frac{P_a}{\Delta f} > \frac{\lambda^3}{8M_3} \qquad (4\text{-}62)$$

For the delay line with a total delay time requirement of T, corresponding to a time-bandwidth of $T\,\Delta f = N$, we have, from equation (4-60)

$$\frac{P_a}{\Delta f} > \frac{\lambda^3}{8M_3}\sqrt{\frac{N}{\delta}} \qquad (4\text{-}63)$$

In Table IV we show the values of the important physical parameters of candidate materials for the delay lines, as pertains to acoustic-optical performance, index of refraction, acoustic velocity, and the figures of merit M_2 and M_3, in MKS units.

We repeat the definitions of the figures of merit, M_2 and M_3

$$M_2 = \frac{n^6\,p^2}{\rho\,v_a^3}$$

$$M_3 = n\,v_a\,M_2$$

where p = photo-elastic constant

ρ = density.

TABLE IV. PHYSICAL PARAMETERS OF CANDIDATE MATERIALS FOR AO DELAY LINES, MKS UNITS

	n	v_a meters/sec	M_2 sec^3/kg	M_3 sec^2-meter/kg
Quartz	1.46	5950	1.51×10^{-15}	1.31×10^{-11}
Dense Flint Glass	1.92	3100	18.9×10^{-15}	11.2×10^{-11}
$LiNbO_3$	2.2	6570	6.95×10^{-15}	10.0×10^{-11}
$PbMoO_4$	2.39	3660	35.8×10^{-15}	31.3×10^{-11}
TeO_2	2.27	617	793×10^{-15}	111.0×10^{-11}
Water	1.33	1500	158×10^{-15}	31.4×10^{-11}

In Table V we show the acoustic attenuation for several candidate materials. These are given for the proposed parameters of the AOAP system, i.e. a center frequency of 60 MHz and a total delay of 7 μsec. Also tabulated is the required length for 7 μsec., and the acoustic wavelength at 60 MHz.

TABLE V. PROPAGATION PARAMETERS AND ATTENUATION OF DELAY LINE CANDIDATE MATERIALS

	Acoustic Velocity meters/sec	Acoustic Λ for 60 MHz	Length for 7 μs	Attenuation at 60 MHz, 7 μs
Fused Quartz	5950	100 microns	41.6 mm	.015 dB
$LiNbO_4$	6570	109.5	46	2.45×10^{-3} dB
$PbMoO_4$	3660	61.7	25.6	.140 dB
TeO_2	617	10.3	4.32	.450 dB

Equation (4-62) is used to generate Table VI, which tabulates the minimum acoustic power required in geometrically optimized delay lines of various materials, for 100% Bragg modulation, using 100% fractional bandwidth for Δf = 10 MHz. Values are shown for the two optical wavelengths of 633 nm (HeNe laser) and 830 nm (GaAlAs semiconductor laser). Also the optimum dimensions a and L are shown as calculated from equations (4-53) and (4-50).

TABLE VI. ACOUSTIC POWER AND GEOMETRY FOR 100% BRAGG MODULATION, 100% FRACTIONAL BANDWIDTH, Δf = 10 MHz, AND NO TIME DELAY REQUIREMENT, FOR OPTIMIZED GEOMETRY

	λ = 633 mm			λ = 830 mm		
	Power	a	L	Power	a	L
Quartz	24.2 mw	.595 mm	816 mm	54.6 mw	.595 mm	623mm
Dense Flint Glass	2.83	.3100	291	6.38	.310	222
$LiNbO_3$	3.17	.657	1500	7.15	.657	1144
$PbMoO_4$	1.01	.366	506	2.28	.366	386
Slow Shear TeO_2	.286	.0617	13.7	.644	.0617	10.4

Thus Table VI shows the theoretically minimum acoustic power (for 100% modulation, Δf =10 MHz) with the delay line geometry totally optimized. As can be seen, this implies somewhat bizarre geometry. For example, in the case of fused quartz, the interaction length is almost 1 meter, and the vertical dimension (perpendicular to both acoustic and optical propagation) is only 1/2 millimeter.

The values of the required power shown in this table, which vary from 1/4 to 50 milliwatts, are so low, that it becomes apparent there is little reason to deal with these extreme geometries since it is easy to achieve substantially larger power levels.

In a more realistic vein, we now tabulate the required electrical power under the constraints of providing 7 μs delay, 10 MHz bandwidth, 60 MHz center frequency, and under the assumption that the electrical to acoustic efficiency is 10%, which is a fairly good number for most cases. Equation (4-63) now becomes

$$P_a > \Delta f \cdot \frac{\lambda^3}{8M_3} \sqrt{\frac{N}{\delta}} \cdot \frac{1}{\rho_E} \qquad (4\text{-}64)$$

where ρ_E = electrical to acoustic efficiency.

Placing the parameters:

$\rho_E = .1$

$\Delta f = 10$ MHz

$f_o = 60$ MHz $\quad \Rightarrow \quad \delta = 1/6$

$T = 7\ \mu s \qquad N = 70$

into the above equation we obtain:

$$P_E(\text{coherent}) = 10^7 \times \frac{\lambda^3}{8M_3} \sqrt{\frac{70}{1/6}} \times \frac{1}{0.1} = 2.05 \times 10^9 \frac{\lambda^3}{8M_3} \qquad (4\text{-}65)$$

with all parameters in the MKS system.

The required value of the vertical dimension a is given by equation (4-52), and the interaction length L is given by equation (4-50). With the above parameters these become

$$a = v_a \sqrt{\frac{T}{f_o}} = v_a \sqrt{\frac{7 \times 10^{-6}}{60 \times 10^6}}$$

$$a\ (\text{millimeters}) = v_a \left(\frac{\text{meters}}{\text{sec}}\right) \times .3416 \times 10^{-3} \qquad (4\text{-}66)$$

$$L < \frac{n v_a^2}{\lambda\ \Delta f\ f_o} = \frac{n\ v_a^2}{\lambda \cdot 10 \times 60 \times 10^{12}} \qquad (4\text{-}67)$$

Using equations (4-65), (4-66), and (4-67) we generate Table VII.

TABLE VII. ELECTRICAL POWER AND GEOMETRY FOR 100% BRAGG MODULATION, 1/6 FRACTIONAL BANDWIDTH, f = 10 MHz, T = 7 SEC, ELECTRICAL TO ACOUSTIC EFFICIENCY = 0.1, FOR OPTIMIZED GEOMETRY

λ = 633 nm

	Electrical Power	a	L	W
Fused Quartz	4.96 watts	2.03 mm	136 mm	41.6 mm
Dense Flint Glass	.58	1.06	48.6	21.7
$LiNbO_3$	.65	2.24	250	46
$PbMoO_4$	.207	1.25	84.3	25.3
Slow Shear TeO_2	.0586	.21	2.27	4.32

λ = 830 nm

	Electrical Power	a	L	W
Fused Quartz	11.2 watts	2.03 mm	103.8 mm	41.6 mm
Dense Flint Glass	1.307	1.06	37.1	21.7
$LiNbO_3$	1.46	2.24	191.0	46
$PbMoO_4$	.467	1.25	64.3	25.6
Slow Shear TeO_2	.132	.21	1.73	4.32

The entries in Table VII still imply some rather expensive crystals. For example, the required interaction length for quartz is now 136 mm, and for $LiNbO_3$ is now 250 nm. With the exception of quartz, the required electrical drive powers are less than 1 watt for 633 nm, and less than 2 watts for 830 nm. It may be that to achieve less expensive crystal dimensions that the interaction length L should be reduced from these optimum values, with an attendant increase in drive power.

Table VII, however, provides an excellent basis of comparison of the candidate materials. Clearly, TeO_2 is the best choice for low drive power. The extremely small value of acoustic wavelength (10 microns) and the small aperture (4 mm) may cause some optical problems associated with the required magnification. $PbMoO_4$ runs a close second in drive power, with more reasonable optical size, and this is also a strong contender, especialy if a non-optimum geometry is considered.

4.2 INCOHERENT OPTICAL OPERATION

4.2.1 Optical Response of Birefringent Modulator

Our original concept was to use the optical output pattern developed by the image converter directly in the second optical section. With this approach the image converter output is imaged on the second delay line, and the light is collected by a lens-detector combination. Since the optical output from the image converter is radiated from a phosphor screen, it is totally incoherent. In an optically incoherent system no spatial frequency plane is available, and thus the phase modulation imparted by the delay line cannot be converted to amplitude modulation by manipulation of the optical frequency plane. Instead, the birefringent effect in the delay line is utilized, which, with the correct orientation, causes a shift in phase difference between the orthogonally polarized components of the optical beam. When used in conjunction with a polarization analyzer, this causes a variation in optical amplitude.

In a region of birefringence, the optical phase is shifted by the active material, according to the direction of polarization of the light with respect to the crystal axes in the direction transverse to the light beam. If the light is resolved conceptually into components in which the polarizations are aligned with the crystal axes, the two components become the ordinary and extraordinary rays of the resulting birefringent behavior. Linearly polarized light, then, will be equally shared between these two orientations if the

direction of polarization of the incident light is 45° to each of the orthogonal axes of the crystal, in the manner shown in Figure 4-8.

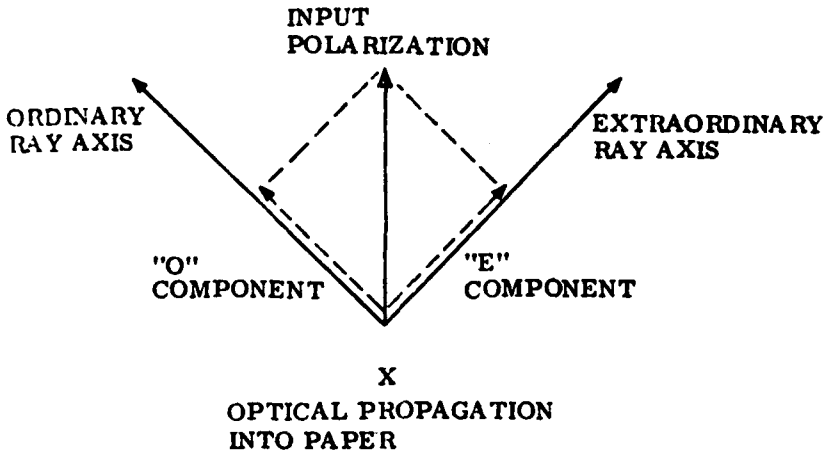

Figure 4-8. Relation of Input Optical Polarization to Crystal Axes

In order to convert the optical phase shifts induced by birefringence into intensity variations, an optical polarizer is inserted after the active crystal, oriented in a direction perpendicular to the unmodulated direction of optical polarization of the input beam. Thus, the output polarizer is crossed, i.e. it is perpendicular to any existing input polarizer. The input polarizer can be omitted if the input light is already polarized, such as from a laser. With this arrangement no light will be translated by the second polarizer in the absence of any birefringence in the crystal. When the material becomes birefringent the light becomes elliptically polarized, so that there is then a component in the crossed direction that will pass through the second polarizer.

This effect can be analyzed in the following way. Consider Figure 4-9, which illustrates the relations between crystal orientation and input light polarization. The light, of amplitude A_o, is shown polarized at 45° to the two crystal axes, the ordinary axis "O" and the extraordinary axis "E". Conceptually, we may resolve A_o into two mutually perpendicular components, aligned with axis E and O as shown. It is obvious that the amplitude of each of these components will then be $A_o/\sqrt{2}$.

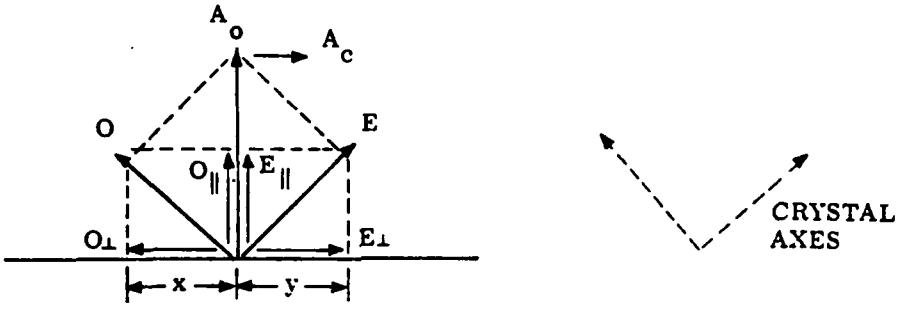

Figure 4-9. Resolution of Input Polarization into Parallel and Perpendicular Components

It is assumed that the output polarizer is oriented perpendicular to A_O, or horizontally in the figure. This polarizer will pass an "O" component labeled x and an "E" component labeled y. These components are analytically created by performing a second resolution of the E and O vectors into orthogonal components, this time breaking each of these into two components, one aligned with the original A_O vector and one perpendicular to this vector. These latter perpendicular components then become the x and y vectors. It can be appreciated (from the figure) that the magnitude of the output light amplitude will be the magnitude of the difference between x and y,

$$A_C = |x - y| \ . \qquad (4\text{-}68)$$

We now account for the birefringent effect as an optical phase shift between the components aligned in the E and O directions, say ϕ radians. From inspection of Figure 4-9, we see that the x-component is given as the 45° component of the "O" component, and the y-component is given as the 45° component of the "E" component. Also (from the figure) we see that both the E and O vectors will generate 45° components along the original A_O axis, and these two components will add with, in general, the same phase difference of ϕ. However, this resultant, whatever its time phase, is polarized at right angles to the output polarizer and, hence, will be rejected by the system.

From the preceding discussion, we conclude that the E and O components of the A_o input can be written as the following phasors, where we assume that no phase shift is imparted by the ordinary polarization (reference phase) and that all the differential phase shift is vested in the E polarization.

$$\left.\begin{aligned} O &= \frac{A_o}{\sqrt{2}}\ e^{j\omega_o t} \\ E &= \frac{A_o}{\sqrt{2}}\ e^{j(\omega_o t - \phi)} \end{aligned}\right\} \qquad (4\text{-}69)$$

where ω_o = optical radian frequency.

Hence x and y are evaluated as:

$$\left.\begin{aligned} x &= \frac{1}{\sqrt{2}} \cdot O = \frac{A_o}{2}\ e^{j\omega_o t} \\ y &= \frac{1}{\sqrt{2}} \cdot E = \frac{A_o}{2} \cdot e^{j(\omega_o t - \phi)} \end{aligned}\right\} \qquad (4\text{-}70)$$

The desired cross-polarized output component, which is that passed by the output polarizer, is then,

$$A_c = |x - y| = \frac{A_o}{2} \left| e^{j(\omega_o t - \phi)} - e^{j\omega_o t} \right|$$

$$= A_o \left| \frac{e^{j\frac{\phi}{2}} - e^{-j\frac{\phi}{2}}}{2_j} \right| \cdot \left| -je^{j(\omega_o t - \frac{\phi}{2})} \right|$$

$$A_c = A_o \sin\left(\frac{\phi}{2}\right) . \qquad (4\text{-}71)$$

The output light intensity is the magnitude squared of the preceding result.

$$I = |x - y|^2 = I_o \sin^2 \frac{\phi}{2} \qquad (4\text{-}72)$$

$$I_o = A_o^2$$

or

$$I = \frac{I_o}{2} (1 - \cos \phi) \; . \qquad (4\text{-}73)$$

Equation (4-72) will be recognized as identical to equation (4-28). Thus imaging by Bragg diffraction produces the same modulation level as birefringent polarized readout.

It will be appreciated that the above function approaches zero as the birefringent phase shift, ϕ, approaches zero. For small values of ϕ this behavior is approximated by a square-law variation, with the normal light intensity equal to zero (dark field).

In the present application a linear variation in intensity is desired, and this can be provided (approximately) by biasing the phase shift with a fixed amount of birefringence in the system. Thus, for example, if a quarter-wave birefringent plate is sandwiched with the active material, the value of ϕ in equation (4-73) is altered by 90°, and (4-73) becomes

$$I = \frac{I_o}{2} (1 + \sin \phi) \; . \qquad (4\text{-}74)$$

The result is approximately linear with ϕ, with the approximation that $\sin \phi = \phi$.

This result essentially squares with the Bragg analysis, equations (4-32) and (4-33). The conclusion is that with the proper birefringent bias, polarized readout of a sine-wave induced phase modulation of amplitude ϕ_m produces the same intensity variation as Bragg imaging, in which the two orders are interfered to produce the image. In either case ϕ_m represents the peak value of phase variation in the delay line modulator. As seen from equation (4-33) for Bragg imaging, if ϕ_m is $\pi/2$ the image intensity varies from black to maximum brightness (unity), which is also true of polarized readout in equation (4-74), as the value of ϕ varies from $-\pi/2$ to $+\pi/2$.

The only difference between the two results is a slight non-linearity in the polarized readout. If ϕ varies sinusoidally along the delay line as induced by the acoustic wave, and we denote the phase of the acoustic wave by θ_a as before, (4-74) becomes

$$\frac{I}{I_o} = \frac{1}{2} \left(1 + \sin \left(\phi_m \sin \theta_a\right)\right) \qquad (4\text{-}75)$$

The non-linearity caused by the outer sine function disappears for small ϕ_m, of course. At such small phase deviations, equations (4-32) and (4-75) become identical.

4.2.2 Power Calculation for Incoherent Case

To evaluate the acoustic power requirements for the incoherent case, using polarized readout, the question of a figure of merit must be addressed. In Sections 4.1.6 and 4.1.7, the figure of merit is based on the appropriate photo-elastic constant, i.e. one of the p's of the photo-elastic tensor described in 4.1.2. The single appropriate p is used in the calculation of the figure of merit, since only the optical phase modulation along a single axis is of interest there. In the present incoherent case, the relative phase between two perpendicular stress-induced optical axes determine the amount of light that passes the crossed polarizer. Thus with stress along the x-axis in the delay line, the phase difference is desired between light passing through with polarization in the y-direction (ordinary ray) and light polarized in the x-direction (extraordinary ray).

In other words, under tensile or compressive stress, the delay line medium acts as a positive or negative uniaxial crystal respectively, and the relative phase modulation corresponding to the difference of the indices of refraction n_o and n_e is the pertinent quantity determining the optical response. Thus instead of a single photoelastic coefficient, the difference between two p's is used. This is the quantity $p_{11} - p_{12}$, in the manner of equation (4-10). The desired acousto-optical figures of merit can be defined just as before, including both M_2 and M_3, except that $p_{11} - p_{12}$ is used as the appropriate photo-elastic constant.

As is pointed out in the discussion following equation (4-10), the amount of phase modulation experienced in the ordinary wave is substantially larger than for the extraordinary ray. For fused quartz the respective stress-optical coefficients are 4.2 compared to 0.65. Thus one concludes that a reasonably accurate approximate result can be obtained

by using the single photo-elastic constant associated with the ordinary ray to represent the relative photo-elastic constant required here. This single photo-elastic constant is the one most widely tabulated, and is the basis of the published values of M_2 and M_3 which have been used in the previous section.

In the incoherent case, the evaluation of geometrical constraints is similar to the previous calculations. As before, the spreading of the acoustic beam in the y-direction must be less than the near-field height of the acoustic beam leaving the transducer in this direction. Thus the constraint as expressed by equation (4-52) stands for this case.

The determination of the limiting value of the interaction length L, however, is somewhat different. The general notion of the limitation in this case is that the optical spreading caused by diffraction by the acoustic wave, as the optical propagation proceeds through the interaction length L of the delay line, must not become large enough so that adjacent acoustic periods are involved. Such mixing of the optical ray into a range of acoustic phases means that the phase modulation of the optical ray will be degraded. The spreading between orders, inside the medium by the acoustic wave is:

$$\Delta\theta_o = \frac{\lambda}{n\,\Lambda} \qquad (4\text{-}76)$$

The requirement is that this be less than order Λ, the acoustic wavelength. Hence

$$L \cdot \Delta\theta_o = \frac{\lambda L}{n\,\Lambda} \lesssim \Lambda$$

Hence L must be less than order

$$L \lesssim \frac{n\,\Lambda^2}{\lambda} \qquad (4\text{-}77)$$

A more precise conclusion can be gained by considering the transition from Raman-Nath diffraction to Bragg diffraction, as the interaction length becomes longer. Raman-Nath diffraction is defined as resulting from modulation that effectively occurs in a single plane. This means that the acoustic wavefronts are aligned with the light rays throughout the interaction region. On the other hand, as discussed in Section 4.1.3.2, Bragg diffraction depends on a continuous

coherent contribution of energy transfer from one order to another as the ray travels through the interaction region. Implicit is the traverse of at least one acoustic cycle by the optical rays. Thus the definition of the Bragg regime is such that the optical ray cannot be constrained to a particular value of acoustic phase, and hence the Raman-Nath condition is required in the incoherent case.

Figure 4-10 shows the diffraction amplitude as a function of modulation index ϕ_m for various values of the interaction length expressed in normalized form, L/L_o. These curves were calculated by W.G. Hoefer of the General Electric Company Electronics Laboratory. [15] The reference length is defined as follows:

$$L_o = \frac{n_o \Lambda^2}{\pi \lambda} \tag{4-78}$$

Consider the first order response. For normalized length of value .316 and less the response corresponds very closely to the Bessel function $J_1(\phi_m)$ associated with Raman-Nath diffraction. For normalized length 3.16 and larger, the response is very close to sin $(\phi_m/2)$ associated with Bragg diffraction. In the curve shown for $L/L_o = 1.0$, the response is well-situated in between these limits. This is particularly clear in the region of the first null in the J_1 response. Thus the value $L/L_o = 1.0$ can be taken to be the effective limit of ray registration with the acoustic wavefront for the entire length of the interaction region. From the definition of the reference length we have:

$$L \leq L_o = \frac{n \Lambda^2}{\pi \lambda} = \frac{n}{\pi \lambda} \frac{v_a^2}{f_o^2} \tag{4-79}$$

Hence for this case, the limiting value of a/L is:

$$\frac{a}{L} > \frac{\dfrac{v_a \sqrt{\dfrac{T}{f_o}}}{n v_a^2}}{\dfrac{\pi \lambda f_o^2}{}} = \frac{\pi \lambda f_o \sqrt{f_o T}}{n v_a} \tag{4-80}$$

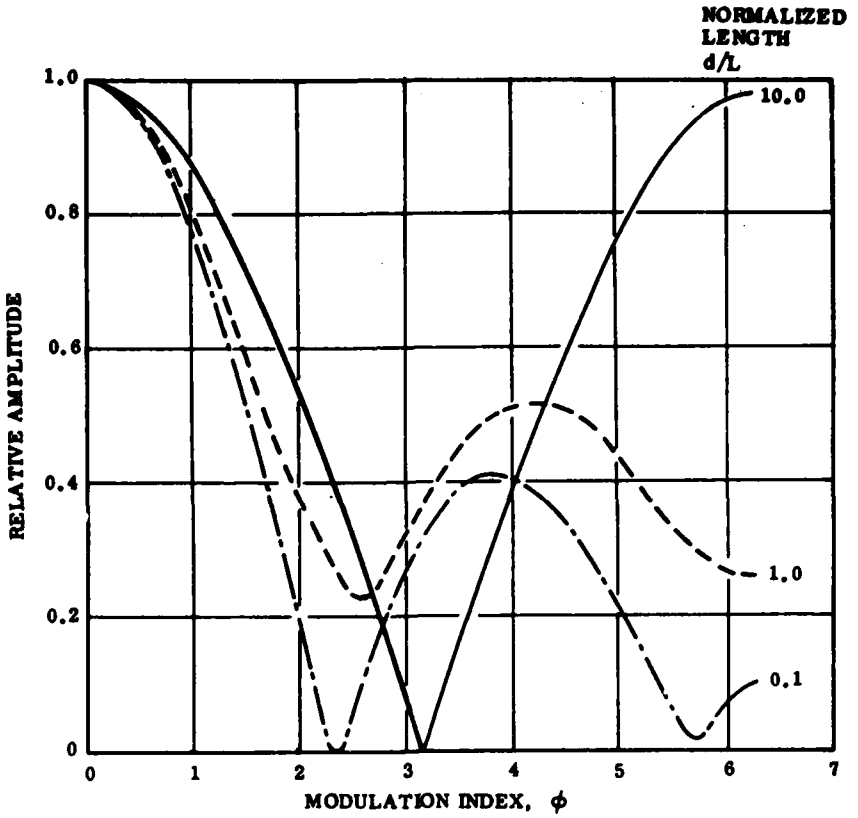

Figure 4-10a. O-Order AO Delay Line Diffraction

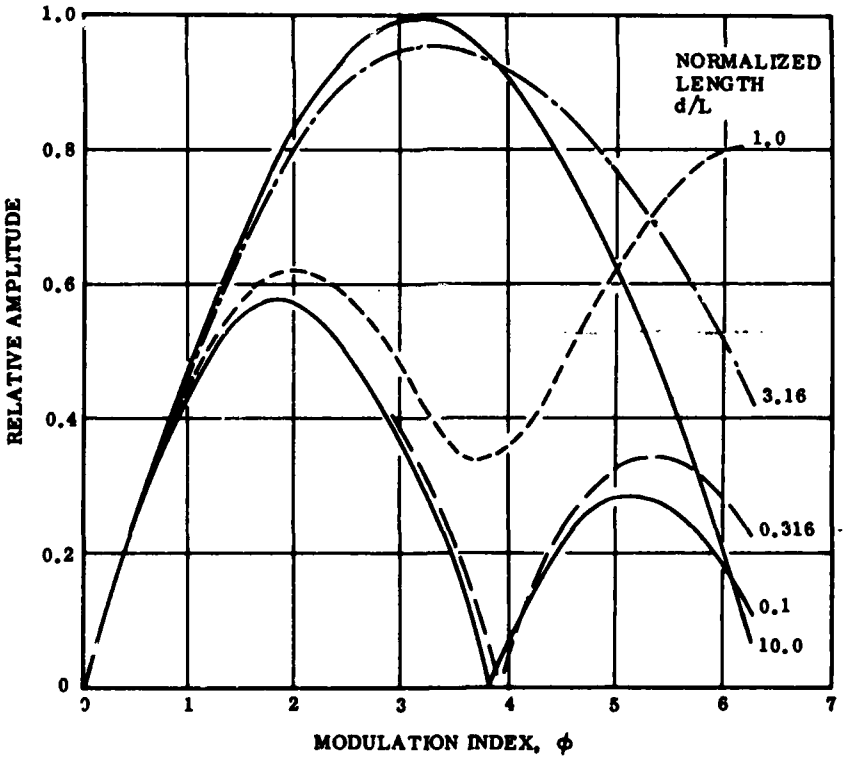

Figure 4-10b. 1st-Order AO Delay Line Diffraction

Substituting this result into equation (4-48), with $\phi_m = \pi/2$, as before, for 100% modulation:

$$P_a = \frac{\lambda^2}{8\ M_2} \quad \frac{a}{L} = \frac{\lambda^2\ \pi\ \lambda}{8\ n\ v_a\ M_2} \quad f_o \sqrt{f_o T} = \frac{\pi\ \lambda^3}{8\ M_3} \quad f_o \sqrt{f_o T}$$

This result may be rearranged into a form which is similar to equation (4-64) as follows:

$$P_{E_{incoh}} = \frac{\pi\ \lambda^3}{8\ M_3} \quad \Delta f \ \frac{f_o^{\ 3/2}}{(\Delta f)^{3/2}} \quad \frac{\sqrt{(\Delta f)T}}{\rho_E}$$

$$P_{E_{incoh}} = \boxed{\frac{\pi\ \lambda^3}{8\ M_3} \quad \Delta f \ \frac{\sqrt{N}}{(\delta)^{3/2}} \cdot \frac{1}{\rho_E}} \qquad (4\text{-}81)$$

Using the values of the parameters, N = 70, δ = 1/6, and ρ_E = 0.1, as before:

$$P_{E_{incoh}} = \frac{\pi\ \lambda^3}{8\ M_3} \times \ 10 \times 10^6 \ \frac{\sqrt{70}}{(1/6)^{3/2}} \cdot 10$$

$$P_{E_{incoh}} = \frac{\lambda^3}{M_3} \times 4.83 \times 10^9 \qquad (4\text{-}82)$$

Using the results expressed by equations (4-52), (4-79) and (4-82) we can construct the following table (Table VIII).

TABLE VIII. ELECTRICAL POWER AND GEOMETRY FOR 100% BRAGG MODULATION, 1/6 FRACTION BANDWIDTH, BW = 10 MHz, T = 7 MICROSEC., ELECTRICAL TO ACOUSTIC EFFICIENCY = 0.1, FOR OPTIMIZED GEOMETRY

		λ = 514 nm		
	Electrical Power	a	L	W
Quartz	50 watts	2.03 mm	8.9 mm	41.6 m
Dense Flint Glass	5.9	1.06	3.2	21.7
$LiNbO_3$	6.6	2.24	16.3	46
$PbMoO_4$	2.1	1.25	5.5	25.6
TeO_2 (Slow Shear)	0.59	0.21	0.15	4.32

It is seen that the power requirements are substantially more for the polarized readout than were the case for Bragg imaging, due to the more restrictive condition on the maximum permissible interaction length.

In the experimentation, we had only two delay lines that were anywhere near the short interaction length required for sufficiently small optical spreading. These were the quartz lines previously described, with an interaction length of 15 mm, and an $LiNbO_3$ line with an interaction length of 5 mm. We now evaluate the 100% modulation acoustic power required for these two lines. With specific geometrical dimensions, without optimization, we have to go back to equation (4-48), using the assumed electrical efficiency as an additional multiplier. In this way we calculate the acoustic power for

1) Quartz line: a = 2 mm L = 15 mm

$$P_E = \frac{\lambda^2}{8M_2} \cdot \frac{a}{L} \cdot \frac{1}{\rho_E} = 30 \text{ watts}$$

2) $LiNbO_3$ line: a = 5 mm L = 5 mm

P_E = 47.5 watts

From these results, it is apparent that we were able to achieve only a small optical modulation index. The 30 watts for quartz is slightly deceptive, since its interaction length is slightly more than the allowable value from Table VIII. The power entry in the table is the more appropriate value, i.e. 50 watts. The equipment that was at hand for the experiment was only capable of delivering 3 watts. Thus from equation (4-48) we can calculate the following values of ϕ_m with the corresponding contrast ratios calculated from equation (4-34), as being induced by 3 watts for the two lines:

1) Quartz line, at 3 watts
   ϕ_m = 0.5 radians, contrast ratio = 0.48

2) $LiNbO_3$ line, at 3 watts
   ϕ_m = 0.4 radians, contrast ratio = 0.39

The results imply a somewhat limited intensity modulation of the light passing through the second delay line, i.e. the delay line associated with the space integrating correlator, in the incoherent mode. This, together with other limitations which will be discussed shortly has resulted in disappointing operation of this part of the system.

4.2.3 Requirements of Ray Registration

As has been previously stated, for proper efficiency in the incoherent optical mode, with polarized readout, it is necessary that the light rays entering the delay line stay collimated or registered with the acoustic wavefronts through the entire interaction thickness of the line. We have already investigated the limitation this imposes on the interaction length because of the diffraction spreading of the optical rays. In addition to this, the orientation of all optical rays entering the delay line must be within strict angular limits to satisfy this registration requirement. Thus if the light rays cross more than 1/2 acoustic spatial cycle by having the wrong angular orientation, or by diffraction spreading, the modulation efficiency is proportionally degraded. The situation is pictured in Figure 4-4.

Thus, the incoherent configuration demands a very large loss of light in the system. Of the approximate full hemisphere of angular radiation from the output surface of the image converter, only that narrow range of angle can be used which properly aligns with the acoustic wavefronts. This angle is approximately given by the ratio of 1/2 acoustic wavelength to the interaction thickness. In the case of the Andersen line, this is 1/150 radians. The selection of this range of angle is accomplished by a stop in the second optical correlator frequency plane. This narrow selection has to

occur in only one dimension, and the full speed of the lenses can be used in the orthogonal direction, which in our experiment is 1/4 radian. Thus the system is equivalent to a circular aperture system in which the aperture diameter is the geometrical mean of these two numbers, or is equivalent to approximately a f/24 optical system, which is very slow. With the maximum intensity level available from the image converter (ITT Model 4108) a theoretical calculation shows that with the parameters that have been suggested, a positive signal to quantum noise ratio should be available at the detector. With marginal theoretical performance, and additional degradation encountered in the practical realization, satisfactory performance of the incoherent section has not been achieved. Part of the reason for the poor performance of this section is believed to be curvature of the acoustic wavefronts, so that optical registration cannot occur. It must be remembered that at the 60 MHz carrier selected, the interaction length is 120 times the half wavelength of the acoustic propagation.

4.3 LIGHT BUDGET ANALYSIS

We now consider the light budget analysis of the system, and the compatibility of the light levels generated by each of the components of the system with the light requirements of the next stage.

4.3.1 Time Integrating Correlator

The illumination of the system was provided by the GaAlAs laser diode. The radiation obtained from this device was used without any spatial filtering with a pinhole. Use of such a pinhole matched in size to the diffraction-related divergence of the beam would produce a uniform beam without significant light power loss.

The effective beam spread of this device is stated by the manufacturer to be $10^\circ \times 25^\circ$. This corresponds to 0.076 steradians. The output wavelength is 830 nm. The maximum rated output power of the diode is 10 mW. As can be seen from Figure 3-2 the output power for a given drive current is strongly temperature dependent. Nevertheless, the output should be kept to 10 mW, regardless of the temperature. To exercise a comfortable safety margin, the device was biased in actual operation to produce an average of 5 mW. This corresponds to a solid angular power density of

5 mW / .076 steradians = .066 watts/steradian.

Referring to Figure 2-1 we see that the light collected by the first collimator in the system is projected as a parallel beam to the first delay line. This plane, in turn, is

imaged to the image intensifier. The light power density at the delay line is found from the above value divided by the square of the focal length of the first collimator, which is approximately 15 cm. Thus:

$$I_{DL1} = .066/15^2 = 293 \times 10^{-6} \text{ watts/cm}^2 \qquad (4\text{-}83)$$

Since, in a Bragg modulator, all the light is essentially delivered to the zero and first order, and these orders are both used to produce an image, the average light level at the image intensifier will be equal to the above value. We now calculate the response of an intensifier to a given input light level. The first issue is the conversion efficiency of the light to emitted photocathode current, which is released to the accelerating field in the device by the photoemitting film.

A standard material which is used for this purpose is the "S-20" photocathode. Since we are using infra-red light at 830 nm to illuminate the intensifier, the device was provided with an "extended red" photocathode, which is essentially an S-25 film. The spectral response of these two materials are shown in Figure 4-11. These curves were taken

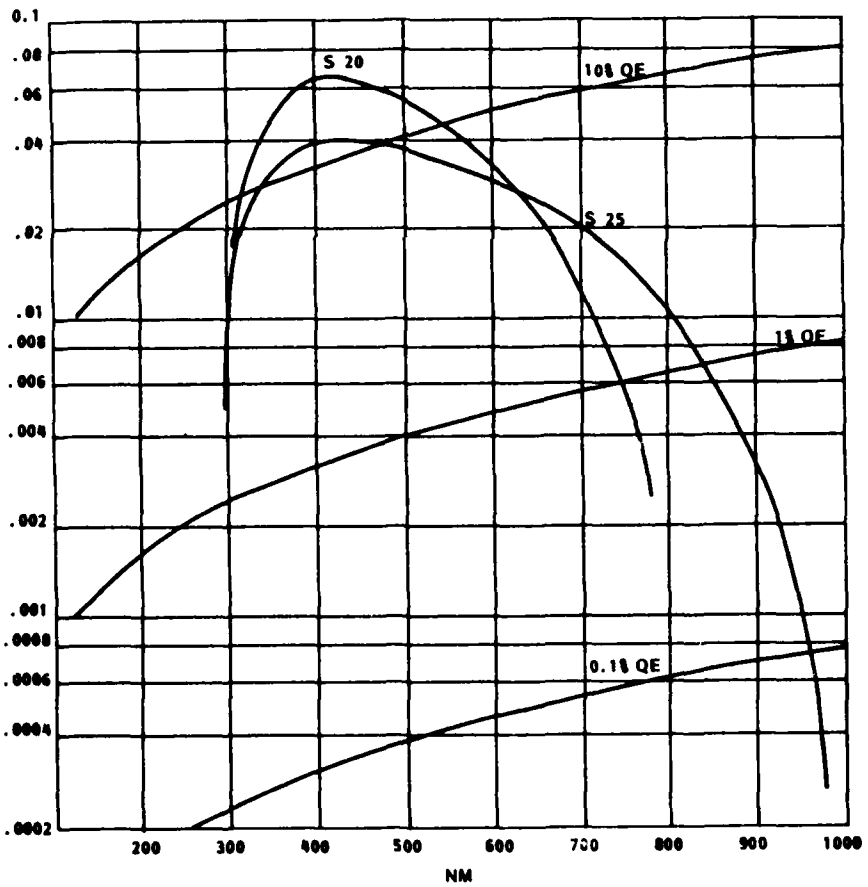

Figure 4-11. Spectral Response Curves for S-20 and S-25 (extended red) Photocathodes. Data taken from Reference [16]

from data published by ITT [16]. In this figure, the sensitivity, in emitted amperes per incident optical watt, is plotted vs. the optical wavelength in nm. The locus of various values of quantum efficiency in units of electrons/photon are also plotted on the same graph. It is seen that while the quantum efficiency is in excess of 10% in the wavelength region of 400 nm, at 830 nm, the S-20 photocathode is nearly inactive, and the S-25 photocathode exhibits a QE of approximately 1%. The following table summarizes the QE and sensitivity in A/W for the important laser wavelengths.

TABLE IX.

		QE	S(A/W)
S-25 at	515 nm	.08	.035
	633 nm	.05	.027
	830 nm	.01	.0067

The sensitivity is given in terms of the QE = η by the following formula, which can be regarded as the definition of QE:

$$S = \frac{\eta\, q}{h\, \upsilon} = \frac{\eta\, q\, \lambda}{h\, c} \quad \text{amperes/watt} \qquad (4\text{-}84)$$

Thus, for example, at 830 nm, we have:

$$S = \frac{.01 \times 1.6 \times 10^{-19} \times .830 \times 10^{-6}}{6.6 \times 10^{-34} \times 3 \times 10^{8}} = .0067 \text{ amps/watt}$$

agreeing with the entry in Table IX.

Having this value, we may now find the maximum allowable average light power density incident on the photocathode of the intensifier, in terms of the allowable photocathode current density. The latter is the best quantity to properly define the onset of destructive levels of operation for the device. For the 4108 intensifer, ITT recommends operating the photocathode current density to a value equal or less than 0.1 microamperes/cm^2. Since the sensitivity, S, as defined before relates the the incident light power density I_{image} to the current density i_{cath}, we have

$$I_{image} = \frac{i_{cath}}{S} \qquad (4\text{-}85)$$

For $i_{cath} = 0.1 \times 10^{-6}$ amperes/cm^2, the result is

$$I_{image} = \frac{0.1 \times 10^{-6}}{.0067} = 15 \times 10^{-6} \text{ watts/cm}^2$$

This amount of light is approximately 20 times less than the level as calculated to be available from the diode laser, through the optics and first delay line DL1. Thus the incident light provided by the system is well in excess of the maximum that can be properly used by the intensifier. The proper match is provided by simple optical attenuation.

The next question pertains to the amount of optical power that the maximum photocathode current will produce. This question is resolved with the help of Figure 4-12. The

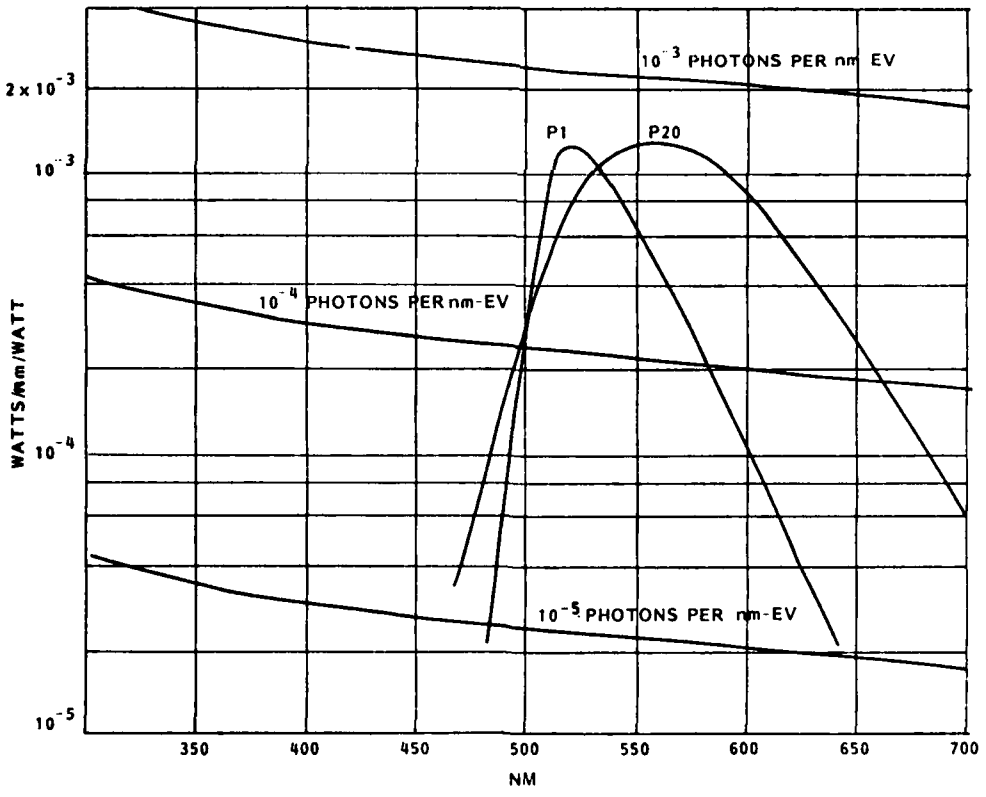

Figure 4-12. Spectral Response Curves of P1 and P20 Phosphors. (Data taken from Reference [16])

information presented in this figure is basically the emission efficiency of the phosphor screen of the intensifier expressed in optical watts radiated per watt impinging on the screen in the form of electron flow. This is shown as a function of optical wavelength. The actual number plotted on the chart is watts/nm-watts. This data was taken from data published by ITT [16].

Two phosphors are shown on the chart, P-1 and P-20. The P-1 phosphor is the material used on our larger 40 mm device, and is the choice that provides a good integration time (>10 milliseconds). The P-20 is used on the smaller device (25 mm) and this device is the one which has been used to report the present results.

As seen from the chart, at the most favorable wavelengths, electron energy is being converted to light at better than 50% efficiency (10^{-3} × 500 nm). Over the active optical band, the average efficiency can be estimated to be better than 10^{-4} photons/nm-ev, or .05 photons/ev. In fact, the overall efficiency published by ITT is .063 photons/ev. Remembering that 1 coulomb-volt/sec. = 1 watt, we can calculate the output optical power density in the following way:

$$P_o = \frac{\text{Output Optical}}{\text{Power Density}} = i_{cath}\left(\frac{\text{coulombs}}{\text{sec-cm}^2}\right) \times \frac{1}{q\,\frac{\text{coulombs}}{\text{electron}}}$$

$$\times V_{bias}\ (\text{volts}) \times K_p\,\frac{\text{photons}}{\text{electron-volt}} \times \frac{hc}{\lambda}\,\frac{\text{watts/sec}}{\text{photon}} \qquad (4\text{-}86)$$

where i_{cath} = photocathode current density (amps/cm^2)

q = electronic charge in coulombs/electron

V_{bias} = accelerating potential across the cathode-phosphor screen gap in the intensifier.

K_p = conversion efficiency of the phosphor in photons/ev

h = Planck's constant = 6.6×10^{-34} joule-sec.

c = velocity of light = 3×10^{8} meters/sec.

Thus for the P-20 photocathode:

$$P_o = i_{cath}\, V_{bias}\, K_p \times \frac{hc}{\lambda q}$$

$$= 10^{-7} \times 6000 \times .063 \times \frac{6.6 \times 10^{-34} \times 3 \times 10^{8}}{1.6 \times 10^{-19} \times .55 \times 10^{-6}}$$

$$= 85 \times 10^{-6} \text{ watts/cm}^2 \qquad (4\text{-}87)$$

Comparing with 4-85, the optical power gain is seen to be 5.7.

This result may be checked by using the published photometric data for the device. The rated optical gain of the device at the favorable input wavelength of 550 nm is 50 ft-lamberts/ft-candle. This means that the total output light, if integrated over the entire solid angle of a hemisphere, is 50 lumens/ft^2 for an illumination of 1 lumens/ft^2. The rated photocathode sensitivity in microamperes/lumen is 225. Thus assuming a maximum photocathode current as before of 0.1×10^{-6} amperes, we have:

$$I_{image} = \frac{10^{-7}}{225 \times 10^{-6}} = 444 \times 10^{-6} \text{ lumens/cm}^2 \text{ incident}$$

Therefore,

$$I_{out} = I_{image} \times 50 = .022 \text{ lumens/cm}^2$$

Over the effective optical wavelength band of the P-20 phosphor, the conversion between lumens and watts is 500. Thus the optical output power density can be calculated as:

$$I_{out} = .022 \text{ lumens/cm}^2 \times \frac{1}{500} \text{ watts/lumen}$$

$$= 44 \times 10^{-6} \text{ watts/cm}^2 \qquad (4\text{-}88)$$

This amount of power corresponds to the photometric level of 20.6 ft-lamberts.

This result is reasonably close to that result expressed by equation (4-87). Conservatively, we will use 44 microwatts/cm^2 as the allowable output level of the device.

4.3.2 Space Integrating Correlator, Incoherent Mode

With the intensifier optical output level calculated in the previous section, we now evaluate the amount of light that reaches the final optical detector, and the resulting SNR, based on quantum noise, or the NEP (noise equivalent power) of the final detector.

The radiation from the phosphor screen can be modelled as a Lambertian surface, which means that the radiation in any direction is proportional to the projected surface area causing the radiation. Thus the optical flux is proportional to cos θ, where θ is the angle from normal to the surface.

The subtense of a sphere in solid angle is 4π steradians, and into a hemisphere is 2π steradians. If the 2π angle is integrated with a weighting function cos θ, the result is π. Thus the radiation normal to the surface is as strong per steradian, as if all the radiation were being directed uniformly into a solid angle of π steradians. Hence the power luminance, B in watts/steradian-cm^{-2}, is given by

$$B = \text{Power Luminance} = \frac{I_{out}}{\pi} \quad \text{watts/steradian-cm}^2 \qquad (4\text{-}89)$$

where I_{out} is the power density being radiated by the surface, i.e. the output screen of the intensifier.

Due to the requirements of waveform registration which has been explained in Section 4.2.3, only a small part of this radiation can be accepted in angle. The desired angle is stopped in the frequency plane of the space integrating correlator, and this amounts to an effective optical speed of f/22.

The optical f/ - number is based on a circular aperture, and is equal to the ratio of the focal length to the diameter. The solid collection angle is thus equal to the area of

such an aperture divided by the square of the focal length:

$$\text{Solid Collection Angle In Space-Int. Correlator} = \Omega_S = \frac{(\pi/4)D^2}{F^2} = \frac{\pi}{4(f/)^2} \qquad (4\text{-}90)$$

where f/ = optical f/ - number of apertured lens.

The power density in the image reaching the second delay line DL2 is then the product of the solid collection angle and the luminance B:

$$I_{DL2} = B\,\Omega_S = \frac{I_{out}}{4(f/)^2} \qquad (4\text{-}91)$$

We are now interested in the amount of light that passes through the delay line corresponding to a spatial degree of freedom, as determined by the bandwidth of the acoustic signal propagating in the delay line. As denoted in the earlier discussion on delay line modulation, the spatial element is b, which if the bandwidth is 10 MHz and the carrier frequency is 60 MHz, is 6 acoustic wavelengths. Thus the area of the spatial element is ab.

Each time a period passes equal to the reciprocal of the signal bandwidth, another independent time sample has been achieved. Thus the single degree of freedom in both space and time is associated with the spatial area ab, and the time increment 1/BW. We may now calculate the number of electrons, corresponding to quantum events from the final detector as the image power density at DL2 times the space and time elements, divided by the energy per photon, or quantum, times the quantum efficiency of the final detector. Thus we have:

$$N_e = \frac{\text{No. Circuit Electrons}}{\text{Degree of Freedom}} = \frac{I_{DL2} \times ab \times \eta_D}{h\,\upsilon\,(BW)} = \frac{I_{out}\,ab\,\lambda\,\eta_D}{4(f/\,)^2\,h\,c\,(BW)} \qquad (4\text{-}92)$$

The notation follows that given in equation (4-86).

For the dimensions of the space integrating correlator being described we have:

$$N_e = \frac{44\times 10^{-6}\times .2\times .06\times (.55\times 10^{-6})\times .1}{4\times 22^2\times 6.6\times 10^{-34}\times 3\times 10^8\times 10\times 10^6}$$

$$= 8 \text{ electrons/degree of freedom}$$

I_{out} watts/cm^2

a = .2 cm
b = .06 cm

The power SNR based on quantum-limited noise is simply the number of events per degree of freedom. Thus the result of 8 electrons per degree of freedom corresponds to an SNR of 9 dB. This result assumes a detector which is quantum noise limited such as a photomultiplier, and the assumed QE of 0.1 is typical for this device.

The foregoing analysis is based on a detector like a photomultiplier which can sense groups of quanta, according to its QE. If a conventional solid state detector is used the available optical power must be compared to the NEP (noise equivalent power) of the device. From the preceding analysis the optical power into the final detector per spatial degree of freedom is clearly given by:

$$\text{Power/spatial degree of freedom} = P_o = I_{DL2} \times ab = \frac{I_{out}\, ab}{4(f/\ )^2}$$

$$= \frac{44 \times 10^{-6} \times .2 \times .06}{4 \times 22^2} = 2.7 \times 10^{-10} \text{ watts}$$

(4-93)

The rated NEP of a typical avalanche detector-amplifier combination, such as the RCA Type C30818 is 3.6×10^{-14} watts/$\sqrt{\text{Hz}}$.

Hence, for a bandwidth of 10^7 Hz, we have:

$$\sqrt{BW}\ NEP = 3.6 \times 10^{-14} \times \sqrt{10^7} = 1.14 \times 10^{-10} \text{ watts}$$

Thus for $P_o = 2.7 \times 10^{-10}$ watts, the SNR is

$$SNR = \frac{2.7}{1.14} = 2.4 \Rightarrow 4 \text{ dB} \qquad (4\text{-}94)$$

In an effort to pick up a signal in the incoherent configuration, a spectrum analyzer was used on the detector output. The frequency resolution of this analyzer was approximately 10^3 Hz. Under these conditions the SNR on the spectrum analyzer display should have been

$$SNR = \frac{P_o}{NEP\ \sqrt{BW}} = \frac{2.7 \times 10^{-10}}{3.6 \times 10^{-14}\ \sqrt{10^3}} = 237 \Rightarrow 24 \text{ dB} \qquad (4\text{-}95)$$

Even with this narrow band, a signal was not observable. This result helped convince us that the curved acoustic wavefront problem described earlier is the most likely explanation of a lack of signal.

As equation (4-95) indicates, the SNR of a Johnson noise-limited detector-amplifier varies as $1/\sqrt{BW}$, not $1/BW$ as in a quantum-limited detector. However, for a high enough BW the device eventually becomes QN limited, when the quantum noise exceeds the Johnson noise. This happens when:

$$NEP\ \sqrt{BW} = \frac{h\ c\ (BW)}{\lambda\ \eta_D} \Rightarrow BW = \left(\frac{\lambda\ \eta_D\ (NEP)}{h\ c}\right)^2$$

Assuming $\eta_D = 0.5$ for the RCA detector, and $\lambda = 550$ nm, we have a cross-over bandwidth of 2.5 GHz.

4.3.3 Coherent Light Modulator Option

As mentioned earlier, it is believed that the difficulties with the coherent optical mode in the space integrating correlator can be resolved with the use of coherent light. This will require that the incoherent light developed by the image intensifier is converted to coherent light, or that the coherent light delivered to the intensifier by the time-integrating correlator be integrated and transformed to a coherent output.

AD-A141 445 ACOUSTO-OPTIC ADAPTIVE PROCESSING (AOAP)(U) GENERAL ELECTRIC CO SYRACUSE NY ELECTRONICS LAB W A PENN ET AL. DEC 83 RADC-TR-83-156 F30602-81-C-0264 2/2

UNCLASSIFIED F/G 20/1 NL

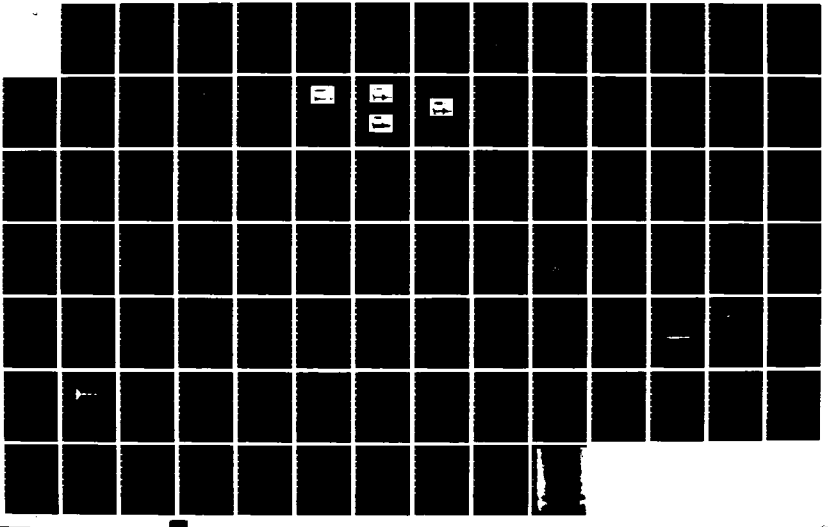

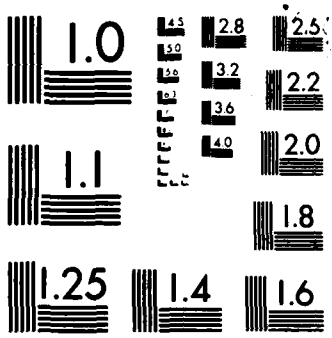

In this section we investigate the use of a coherent modulator to perform the functions of integration and the relaying of the spatial information in optically coherent form to the space-integating correlator. Two devices which are candidates for this purpose are the Liquid Crystal Light Valve (LCLV) made by Hughes Aircraft, and the Itek Pockel's Readout Optical Modulator (PROM). The difficulty with using these devices directly, without an image intensifier in the system, is that neither the LCLV nor the PROM is sensitive to the infrared wavelength generated by the input laser (830 nm). With this input wavelength, the intensifier is still needed to convert the 830 nm pattern to light in the 550 nm, region, which can then energize either the LCLV or the PROM.

It is believed that the LCLV is the most suitable of the two devices for this application, being a simpler device, and having a moving time integration window, rather than the "store and dump" mode used by the PROM. Hence, we will here analyze the compatibility of the LCLV with the rest of the proposed system.

Figure 4-13 shows a cross section of the LCLV. The device is in two sections which are optically isolated from

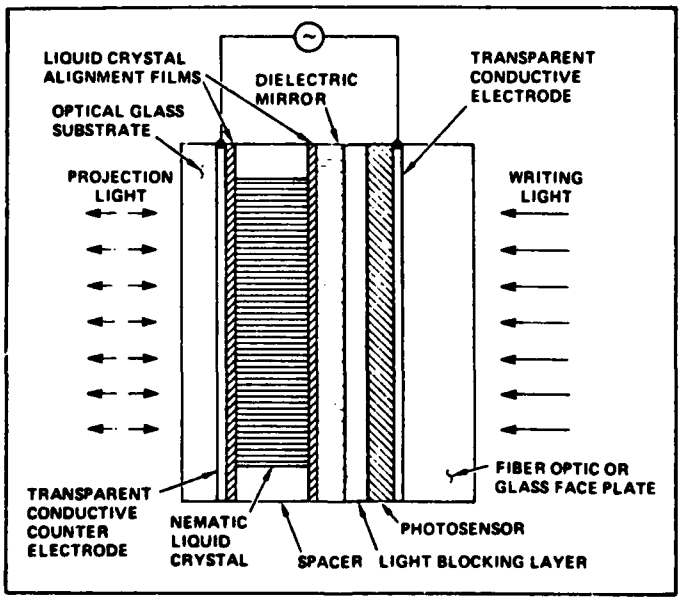

Figure 4-13. Cross-sectional Schematic of the Liquid Crystal Light Valve (Taken from Reference 17)

each other. The writing light comes in from the right and falls on a CdS photoconductive layer. This layer interacts with a bias voltage (a.c.) to produce an electric field across the liquid crystal in the second section, which is an image of the written pattern.

This field causes a change in the polarization of the coherent light which is reflected into and out of the liquid crystal layer. This effect is depicted in Figure 4-14. It is called by Hughes a "hybrid field effect mode" which involves both the effect of optical activity due to the twisted nematic effect in the liquid crystal and a birefringent effect. A detailed description of this process is contained in Reference 17.

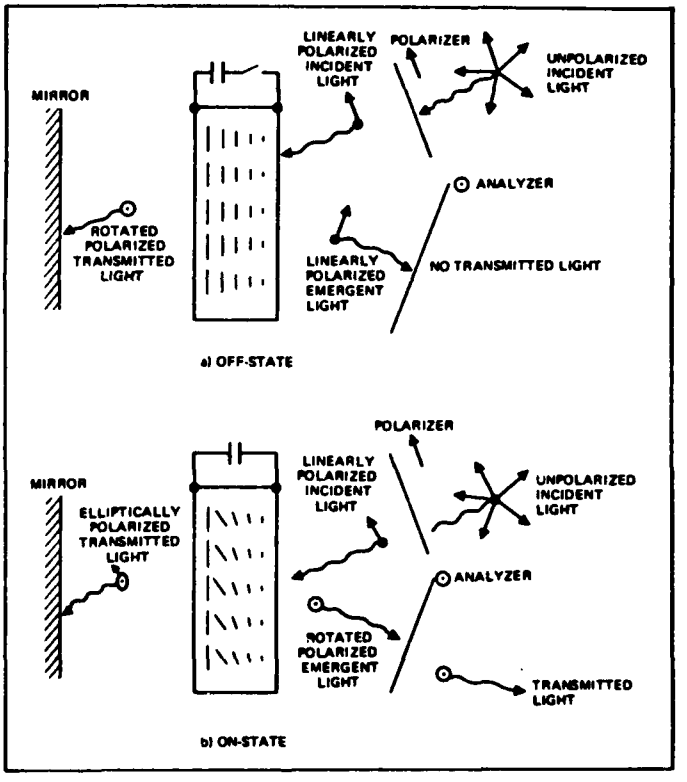

Figure 4-14. Operation of the Hybrid Field Effect Mode Light Valve: (a) the off-state; (b) the on-state (Taken from Reference 17)

Figure 4-15 shows the spatial frequency response of the LCLV (MTF curve) as measured by the first order diffraction in a coherent readout. A grating of variable spatial frequency was written into the device, and the value of this spatial frequency is the abscissa of this graph. The intensity of the diffracted order is down by a factor of 1/2 (3 dB) at approximately 18 cycles (line pairs) per mm. Thus the performance of the device at 10 cycles/mm, which is the grating frequency generated by the image of the delay line, should be excellent.

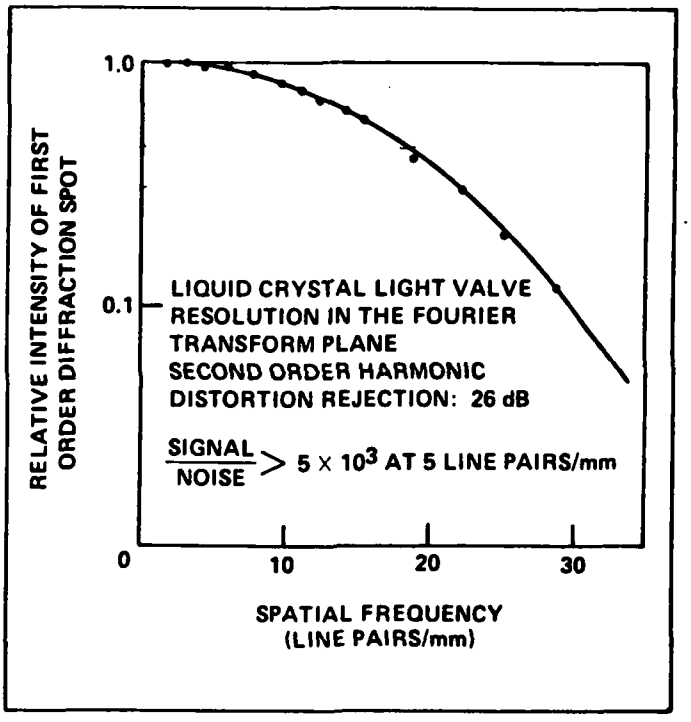

Figure 4-15. Relative Intensity of the First Order Diffraction Spot as a Function of Spatial Frequency. (Intensity is normalized to one at zero spatial frequency. One square inch of LCLV was used in the measurement. Second order diffraction spot intensity was <1% of first order at all frequencies. Readout wavelength = 514.5 nm. (Taken from Reference 17)

Finally, the sensitometry of the LCLV is shown in Figure 4-16. Both scales in this presentation are log-intensity in the manner of a sensitometry curve for photographic film. The curve exhibits a threshold knee somewhat below 1 microwatt/cm^2 and a saturation shoulder in the region of 100 microwatts/cm^2. For the best and most linear operation, the normal light level without signal modulation should be in the middle of the linear range of this curve, which is approximately 10 microwatts/cm^2. Thus the 44 microwatts/cm^2 which was found to be available from the intensifier (and which may be substantially higher) in the previous section, should be quite adequate to drive the LCLV. This should be true whether the direct coupling through the fiber optic faceplates of the two devices is used, or the output screen of the intensifier is optically imaged with a reasonably fast lens to the input screen of the LCLV. To image with a loss of 1/4 would require an f/1 lens. This is fast, and with high resolution would be a relatively expensive lens, but it is quite practical for incoherent imaging.

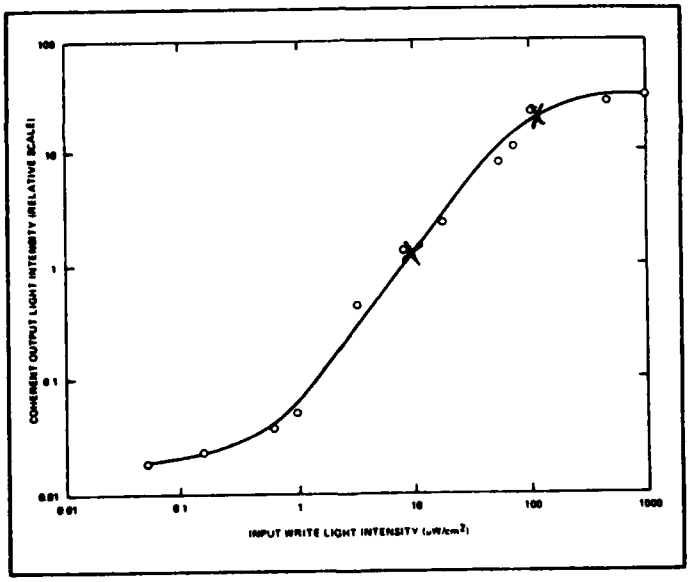

Figure 4-16. Sensitometry Curve for LCLV over a 3 mm Diameter Region of Aperture
(Taken from Reference 17, by Casasent)

5 RECOMMENDED AOAP DESIGN

5.1 COHERENT AND NON-COHERENT OPTIONS

In the previous sections we have considered both optically incoherent and coherent operation of the space-integrating correlator of the AOAP.

The incoherent mode is a rather natural conceptual possibility, since the input optical pattern to this section of the AOAP is developed on the phosphor screen of the image intensifier, which radiates totally incoherent light. The original hope was that an optically incoherent correlator could accept this input directly and thus transmit a carrier borne correlation function to the output detector as an intensity modulation.

It was found that with the maximum intensity that can safely be derived from the output screen of the intensifier, there is a fundamental light loss which results in an output SNR of 9 dB, for a bandwidth of 10 MHz, and a photomultiplier detector with a QE of 10%. Alternatively an SNR of 4 dB is achieved with a sensitive avalanche silicon detector.

These SNR's come about because of the narrow restriction on light rays that can be used in the acoustic delay line modulator, and the requirement of ray registration with the acoustic wavefronts. The indicated SNR's were not achieved in the experiment. Narrow band tests were also performed on the system to enhance the SNR in the incoherent mode, also without success. Even if the incoherent mode can be made to work according to the theoretical SNR, it appears the performance will be marginal.

On the other hand, it has been found to be easy to achieve good performance with a coherent optical system. To show this, an optical grating of the same spatial frequency as the correlation pattern achieved on the image converter was placed in the position of the image converter and illuminated with an expanded HeNe laser beam. Now little or no light has to be sacrificed to match the required angular registration with the acoustic wavefronts. A Bragg optical delay line can be used, as was done in the first optical section, and with the generation of only two optical orders, the full potential of the Bragg thickness can be used to generate an amplitude-modulated signal. A slight curvature of the acoustic wavefronts does not degrade the amount of diffraction, but merely causes a slight curvature of the diffracted optical wavefronts. The concept is essentially that of a volume hologram. The signal in both the incoherent

and coherent cases is generated by the action of a moving grating (the acoustic wave) passing by the image of the correlation pattern (a fixed grating). In the coherent case the signal carrier can be alternatively thought of as being generated by a heterodyne action. This is the interference between an optical order not diffracted by the delay line becoming coincident with an order which is diffracted by both the input grating and the delay line. The light which is diffracted by the delay line has a doppler shift equal to the acoustic frequency, and the acoustic carrier recovered in the detector is the beat frequency between the two orders. The device which we have selected to provide spatial modulation of a coherent optical beam, thus serving the role of the optical grating in the experiment which has been described, is the liquid crystal light valve.

An important restriction on the use of an LCLV in the AOAP system is the spectral range of the photoconductor used as an input receptor for the device. In the case of the Hughes LCLV this is a film of cadmium sulfide, which does not respond well at optical wavelengths much longer than 550 nm. Thus if an infrared illumination is used, as has been done with the present configuration, in which a GaAlAs laser diode is the light source operating at 830 nm, there is no possibility that the LCLV can respond to this.

However, we have already noted that the required level of input light for this device is well matched to the expected output level of the image intensifier which has already been used in the experiments performed. An output level of at least 44 microwatts/cm^2 is obtainable from the image intensifier, and an input level of 10 microwatts/cm^2 puts one in the middle of the linear range of operation of an LCLV.

Thus since the input level of the LCLV and the output level of the image intensifier are compatible, the retention of the intensifier in the optical design offers a solution to the wavelength compatibility problem. The intensifier, as explained in Section 4.3.1, uses an S-25 photoemitter, which is an "extended red" material, and, as indicated in Figure 4-11, responds quite satisfactorily to input radiation at 830 nm. Also as previously noted, an abundance of optical power at 830 nm is available from the time integrating correlator, being a coherent system, with a high degree of light utilization efficiency from input to output.

It is estimated that the output of the image intensifier can be relayed to the input plane of the LCLV by either a fast high quality 1:1 lens, or by intimate contact between the fiber optical faceplates provided on both devices. In

either case, the coupling should be possible with a loss of not more than 4:1, a result which is compatible with the optical power levels cited above.

It has been shown that both the spatial frequency response of the image intensifier and the LCLV are well within the carrier spatial frequency developed by the AO delay lines of 20 cycles/mm.

Finally, the spectral response of the LCLV and the output optical spectrum of the image intensifier phosphor are well matched. In Figure 5-1 we show a spectral response curve of the cadmium sulfide as measured by its effect on the LCLV. It is seen that the primary response band is between 500 and 600 nm. Referring to Figure 4-12 it can be observed that the emission of both the P-1 and the P-20 phosphors are well matched to the LCLV photoconductor. In particular, the P-1 phosphor straddles almost precisely the band of the LCLV.

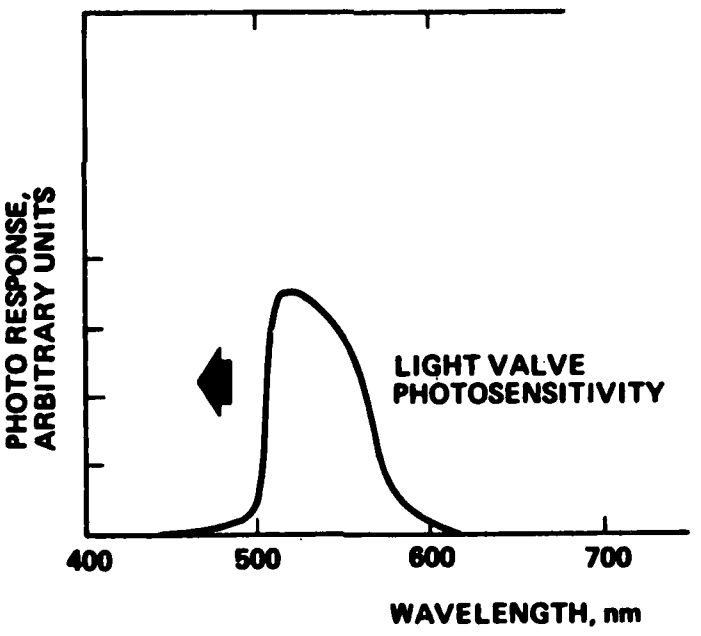

Figure 5-1. Light Valve Photo Response Characteristics

In view of these considerations, our conclusion is that a coherent optical mode for the space-integrating correlator will produce far superior performance of the AOAP system, and this is the configuration that is planned for the next experiment.

5.2 PROPOSED REDESIGN OF THE AOAP OPTICAL CHANNEL

In the next phase of this effort, we will implement the system shown in Figure 5-2. This design is very similar to the experiment which has been accomplished, with the important addition of a liquid crystal modulator to convert the space integrating correlator to an optically coherent mode.

A spatial filter has been added to the GaAlAs laser to produce a "clean" spatial illumination for the first delay line. Imaging from the first delay line to the image intensifier will be accomplished by a telecentric system as before. Wollensak f/4.5, 241 mm lenses obtained for this purpose will be used. Again, no spatial optical stop will be required in the frequency plane, since the delay line operates in the Bragg mode, and the resulting two diffraction orders provide the required spatial carrier based on light amplitude variation. In the first phase of the new experiment, an Isomet glass Bragg cell will be used as before for an initial demonstration, since a high degree of modulation can be obtained with these devices. They do not provide the 7 microseconds time window that is the goal of this effort, but that will be achieved later with the Andersen lines previously obtained, or with new lines, possibly constructed of $PbMoO_4$. In any case, a spatial carrier frequency of 10 cycles/mm will be used. For the glass or the $PbMoO_4$ lines this required a temporal carrier frequency for the acoustic signal of approximately 35 MHz. The delay line will be mounted on a transverse slide with a differential micrometer control for careful phase adjustment.

For the initial experiment the 25mm diameter image converter will be used, which has the P-20 phosphor, and a fiber-optic faceplate for coupling from the phosphor screen to the next device.

Following the image converter will be the LCLV, to be obtained from Hughes Aircraft. Although the P-20 phosphor is not quite as good a spectral match to the LCLV as the P-1, it is a reasonably good match. The P-1 can be used in later experiments. The P-20 does not provide any significant time integration (on the order of microseconds), but the response characteristics of the LCLV will provide a very satisfactory integration time.

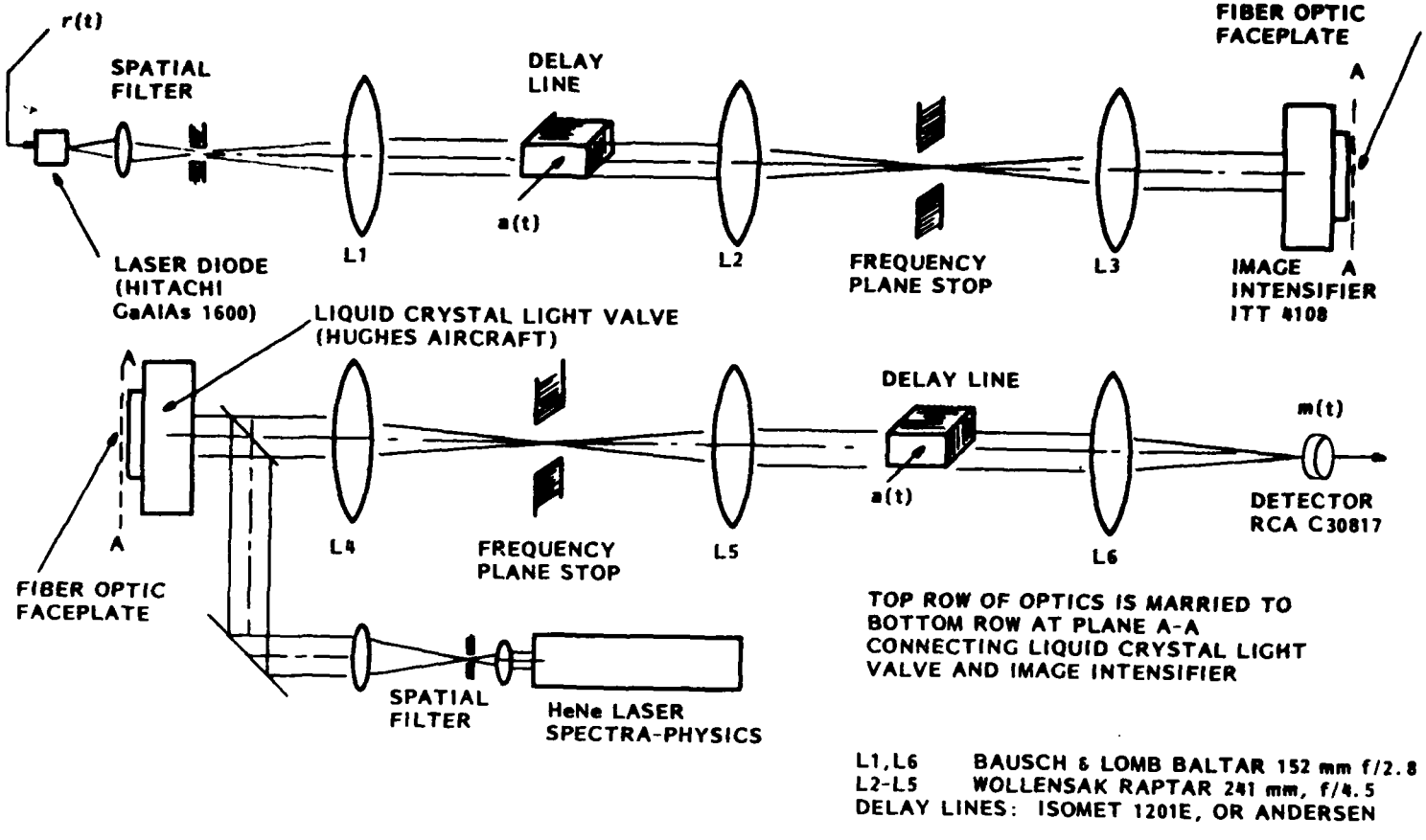

Figure 5-2. Proposed Redesign of AOAP Optical System

The readout liquid crystal plane is located on the other side of the LCLV device from the input photoconductor. A collimated laser beam (expected to be a HeNe laser providing 633 nm) will be introduced into this layer with a beam splitter oriented at 45° to the optical axis, as shown in Figure 5-2. This will inject the beam parallel to the optical axis into the liquid crystal (i.e. perpendicular to the liquid film) and the light will be reflected and will pass out of the liquid film. The passage through the liquid film, and a polarizer, will provide the desired amplitude modulation in accordance with the pattern relayed from the image converter. The beam carrying this pattern will be travelling parallel to the optical axis once again and will pass through the second delay line DL2, which is expected to be identical to the first delay line. Bragg modulation will occur in this delay line as in the first, and the product beam will then pass to the output detector. Imaging from the LCLV to DL2 will occur by means of a telecentric optical system identical to the first section, using two more Wollensak lenses. Again, no stop will be required in the frequency plane, because of the Bragg operation of DL2.

Of course, in closed loop operation, the output of the final detector will be electronically subtracted from the main channel signal which was used to modulate the laser source, to complete the adaptive loop. As pointed out in Section 4.1.4 all of the operations described are theoretically linear. With the introduction of the two diffracted orders from the Bragg line to the image intensifier, a linear carrier frequency is realized in the intensity variation. The image intensifier is sensitive to input intensity and converts this to an emitted intensity. This, in turn is preserved as an intensity variation into the photoconductor of the LCLV. Here the linear intensity variation is scaled into a coherent light amplitude modulation of the laser beam passing through the liquid crystal. This is multiplied in amplitude by the diffraction effect of DL2, and the final product is summed and delivered to the final detector. This detector is, like the intensifier, sensitive to input intensity, and the carrier realized by the interference of the two diffracted orders becomes a linear function in the detector current output. It is obvious that the loop gain can be controlled over wide limits by electronic control in the feedback path.

6 AOAP SYSTEM TEST STUDY

6.1 TRANSIENT RESPONSE OF AN ADAPTIVE LINEAR PREDICTION FILTER TO A SINUSOID IN NOISE

6.1.1 Introduction

Linear prediction filters have many applications in diverse fields, such as spectral analysis, system modeling, speech encoding, and noise cancellation [18]-[21]. One application of interest is the cancellation of a sinusoidal interference in white noise. A comprehensive steady-state analysis of this problem appears in [2]. Of interest here, however, is the transient response to sinusoid in noise. In particular, the behavior of the transient response will be examined as the number of taps N approaches infinity, but the total delay remains constant. The motivation for this investigation stems from a desire to characterize the transient performance of the AOAP which realizes a continuum of adaptive weights [4]-[6]. The transient response in the noise-free case was described on a very simplified basis in Section 2-2, and the conclusions here will reinforce the essentials of that discussion.

A general discussion of the ALP filter and its analytical properties will be presented first, followed by a transient analysis for the case of a sinusoid in white noise. A particular example will then be considered and the asymptotic behavior examined as the number of taps increases to infinity. Experimental results are also obtained using a real time ALP filter which was previously designed and constructed [18].

6.1.2 General

Figure 6-1 shows an adaptive transversal filter structure whereby an output

$$y(t) = x(t) - \sum_{n=1}^{N} W_n x(t-T_n) \qquad (6\text{-}1)$$

is formed by subtracting from the input x(t), a sum of N delayed input signals $x(t-T_n)$, n = 1,2,...,N, weighted by the adaptive weights $W_1, W_2, \ldots W_N$. The weighted sum is denoted by x(t) and is intended to form a least-mean-square estimate of the present value of x(t) using a linear sum of past values. Hence, this configuration is known as an adaptive linear predictor (ALP) filter [18]. The adaptive weight algorithm by which this is accomplished is known as the "least-mean-square" (LMS) algorithm [19], which, in discrete time, can be written [18]

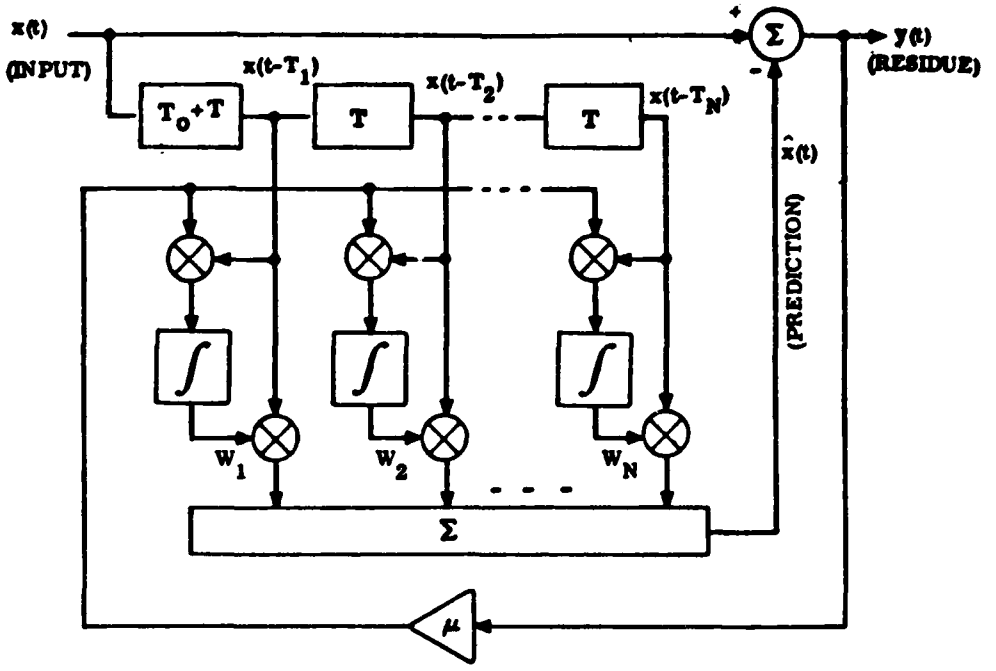

Figure 6-1. Block Diagram of Adaptive Linear Prediction Filter Using Correlation Cancellation Loops

$$W_n(t+1) = W_n(t) + \mu\, y(t)x(t-T_n),\ n=1,2,\ldots,N. \quad (6\text{-}2)$$

As is well-known in linear estimation theory, LMS estimation error requires that the error, or output y(t), in this case, be uncorrelated with each auxiliary signal, and is known as the "orthogonality condition" [23]. This is exactly the condition that (6-2) converges to in mean, and hence is also known as a "multiple correlation cancellation loop" [18]. Substituting (6-1) into (6-2) and solving for this condition then determines the mean steady-state weight vector

$$E\,\underline{W}_\infty = \underline{R}^{-1}\,\underline{r} \quad (6\text{-}3)$$

where $\underline{R}$ is an N × N covariance matrix with elements

$$R_{ij} \triangleq E\left\{x(t-T_i)x(t-T_j)\right\} \quad (6\text{-}4)$$

and $\underline{r}$ is an N × 1 column vector with components

$$r_i \triangleq E\{x(t)x(t-T_i)\} \quad . \tag{6-5}$$

The mean transient solution of (6-2) can be written [18]

$$E\,\underline{W}(t) = (\underline{I}-\mu\underline{R})^t\,\underline{W}(0) + \underline{R}^{-1}[\underline{I}-(\underline{I}-\mu\underline{R})^t]\,\underline{r}\ , \tag{6-6}$$

which can be shown to converge to (6-3) provided

$$0 < \mu < 2/\lambda_{max}, \tag{6-7}$$

where λ_{max} is the largest eigenvalue of the covariance matrix $\underline{R}$. The eigenvalues of $\underline{R}$ also characterize the transient solution (6-6), each one being associated with an exponential convergence mode of the form $e^{-\mu\lambda_i t}$ [19]. Thus, the convergence time constant of the i^{th} mode is given by

$$\tau_i = \frac{T_s}{\mu\lambda_i}\ , \tag{6-8}$$

where T_s is the sampling interval.

In many cases of practical interest, the so-called "clipped-LMS" algorithm is employed whereby (6-2) becomes*

$$W_n'(t+1) = W_n'(t) + \mu\ y(t)\ \mathrm{sgn}\,[x(t-T_n)]. \tag{6-9}$$

In this variation, the correlation multiplication only involves the sign of the auxiliary tap signal, and results in a simplified hardware implementation. It can be shown that for sinusoidal signals and/or Gaussian processes, the weights will converge to exactly the same steady state values, provided that

$$\mu < \frac{2}{\sqrt{\frac{2}{\pi}}\ \frac{\lambda_{max}}{\sigma_x}} \tag{6-10}$$

---

* An apostrophe (') will be used throughout to indicate quantities associated with the clipped-LMS algorithm.

However, the modal time constants in this case are modified to [24]

$$\tau'_i = \frac{T_s}{\mu \sqrt{\frac{2}{\pi}} \frac{\lambda_i}{\sigma_x}} \qquad (6\text{-}11)$$

6.1.3 Transient Response for Sinusoid in Noise

An analysis of the transient response of an ALP filter to a sinusoid in white, or uncorrelated, noise appears in [25] and will be summarized here. A single sinusoid of frequency $f_o = \omega_o/2\pi$ in white noise can be expressed as

$$x(t) = A \cos \omega_o t + n(t), \qquad (6\text{-}12)$$

where $n(t)$ is white noise with variance σ^2. Substituting this expression into (6-4) and (6-5) then gives the elements of the covariance matrix as

$$R_{ij} = \gamma \cos[\omega_o(T_i - T_j)] + \sigma^2 \qquad (6\text{-}13)$$

and

$$r_i = \gamma \cos(\omega_o T_i), \qquad (6\text{-}14)$$

where $\gamma \overset{\Delta}{=} A^2/2$ is the power of the sinusoid. If the taps are uniformly spaced as

$$T_n = T_o + nT, \qquad (6\text{-}15)$$

the eigenvalues of (6-8) can be simply expressed as [24]

$$\lambda_{1,2} = \frac{N\gamma}{2}(1 \pm \beta) + \sigma^2 \qquad (6\text{-}16a)$$

$$\lambda_i = \sigma^2, \quad 2 < i < N, \qquad (6\text{-}16b)$$

where

$$\beta = \frac{\sin N\omega_o t}{N \sin \omega_o t}. \qquad (6\text{-}17)$$

It is also shown in [24] that the sinusoidal component of the output corresponds to the convergence modes associated with the two largest eigenvalues (6-16a). If $\beta \neq 0$, then the composite convergence will be dominated by the smaller of these two eigenvalues. Therefore, combining (6-8) and (6-16a) gives the dominant time constant as

$$\tau_{max} = \frac{T_s}{\mu \left[\frac{N\gamma}{2}(1-|\beta|) + \sigma^2\right]} \quad . \tag{6-18}$$

For the clipped-LMS algorithm, a similar expression is obtained from (6-11) as

$$\tau'_{max} = \frac{T_s \sqrt{\gamma + \sigma^2}}{\mu \sqrt{\frac{2}{\pi}} \left[\frac{N\gamma}{2}(1-|\beta|) + \sigma^2\right]} \quad . \tag{6-19}$$

Special cases of the above occur for a noiseless sinusoid, for which

$$\tau_{max} = \frac{T_s}{\mu N \frac{\gamma}{2}(1-|\beta|)} \quad , \sigma_n = 0 \tag{6-20}$$

and

$$\tau'_{max} = \frac{T_s}{\mu N \sqrt{\frac{\gamma}{2\pi}(1-|\beta|)}} \quad , \sigma_n = 0 \quad . \tag{6-21}$$

Examination of these last two expressions incidentally shows how the clipped-LMS algorithm reduces the variation of time constant with γ.

It does not appear to be analytically tractable, at least within the scope of the present effort, to extend this analysis to the case of a sinusoid in correlated noise. Therefore, examination of this effect will be deferred to the section on experimental results.

6.1.4 An Example

An example will now be given to illustrate the foregoing theory. Suppose that the tap delays are chosen such that $f_o T_1 = 1/8$ and $f_o T_N = 3/8$, i.e., the taps span 90 degrees of phase, as illustrated in Figure 6-2. Then, the spacing between taps T is determined by the expression

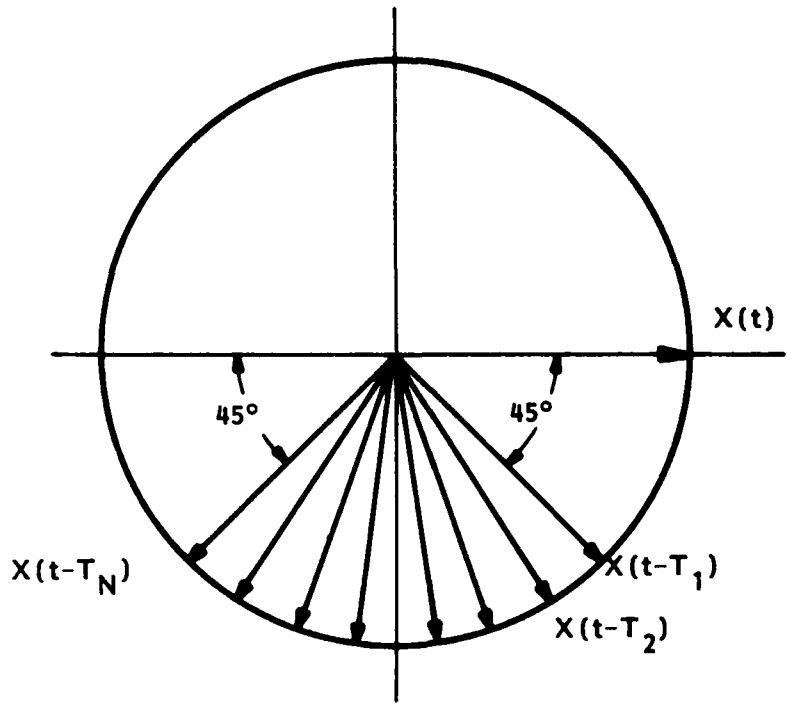

Figure 6-2. Phasor Diagram of Main and Auxiliary Tapped Delay Line Signals

$$f_o T = \frac{1}{4(N-1)} \quad . \tag{6-22}$$

Substitution into (6-17) then gives

$$\beta = \frac{\sin\left(\frac{\pi N}{2(N-1)}\right)}{N \sin\left(\frac{\pi}{2(N-1)}\right)} \xrightarrow{N \to \infty} \frac{2}{\pi} \quad . \tag{6-23}$$

Equation (6-16a) shows that in the limit as $N \to \infty$, the eigenvalues increase to infinite values, which will eventually result in instability according to (6-8) or (6-11). Therefore, in reality the gain must be reduced as N increases so as to keep the value of μN a constant. This is also a natural physical constraint for an implementation involving a continuum of weights such as AOAP. It can be seen from (6-20) and (6-21) that if μN is a constant, then the time constant for the noiseless sinusoid varies with N only as a function of β which approaches the asymptotic value of $2/\pi$ given in (6-23).

Consider, for example, the clipped-LMS algorithm operating with a noiseless (σ=0) sinusoid of rms value 0.1 corresponding to γ = 0.01, a loop gain μN = 1/160 and sampling frequency of 6500 Hz. Substitution of these values into (6-23) and (6-21) then gives the values in Table X for various values of N.

TABLE X. CALCULATED VALUES FOR γ = 0.01, σ_n = 0, $N\mu$ = 1/160, T_s = 1/6500

N	β	λ_{min}	τ'_{max}
2	0	0.0100	0.6170
4	.4330	0.0113	1.0882
8	.5477	0.0181	1.3641
16	.5946	0.0324	1.5222
∞	.6366	∞	1.6980

As expected, the time constant approaches a limiting value as $N \to \beta$.

6.1.5 Experimental Results

The ALP filter hardware described in [18] was restored to operation and was used to obtain the experimental results reported here. The purpose of these experiments was to verify the analytical results obtained in the last section for uncorrelated noise and to determine the effects of correlated noise on this performance.

Figure 6-3 shows the experimental transient response obtained using the same parameters as the example in the last section (f_o=446.43 Hz, T_1=0.28 ms, T_N=0.84 ms, γ=0.01, μN=1/160, T_s=1/6500). The upper trace shows the adaptive weight trajectories for N=8 and N=2, respectively, referred to a 10V reference (2 cm/unit). These curves can be seen to approach the theoretical steady state values given in [22]. For N=2, these values are simply $\pm \sqrt{2/2} \cong \pm$ 0.707, as can be appreciated from the diagram in Figure 6-2.

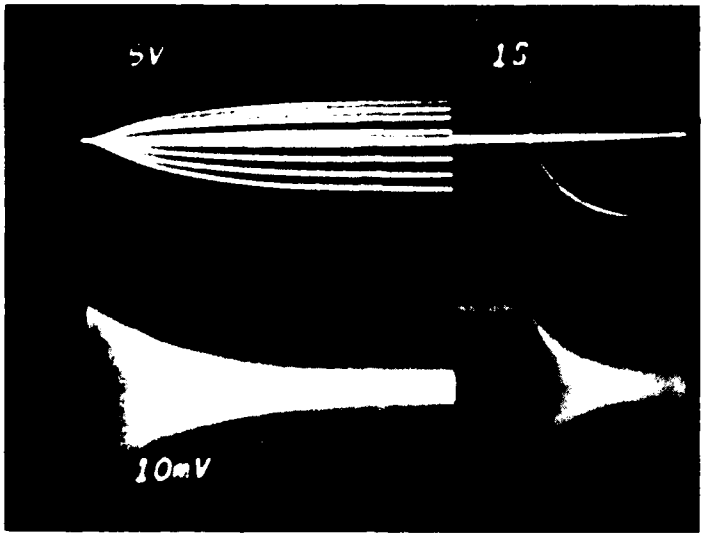

Figure 6-3. Transient Response for μN=1/160, Noiseless Case

The lower trace in Figure 6-3 shows the transient response of the output, which starts initially at the input level of 0.1V rms ≅ 282 mV peak-to-peak*, and decays down to a residual noise level caused by digital processing noise which was inadvertently picked up (for a noiseless sinusoid, the output voltage should ideally converge to zero).

Both of the exponential curves in Figure 6-3 exhibit a time constant which can be seen to be in rough agreement with the theoretical values in Table I for N=8 and N=2.

For the remaining experiments, it was more convenient to maintain the same loop gain which was held constant at μ=1/320. Figure 6-4 shows a replay of Figure 6-3 with constant loop gain, and will be used to compare with plots to follow.

Figure 6-5 shows the convergence for the signal plus noise case. The noise level was 31.6 mV rms (-30 dBV) which corresponds to a 10 dB SNR. The noise bandwidth for this equipment was 5 kHz, which resulted in nearly uncorrelated

*The calibration shown for the lower traces in Figures 6-3 through 6-6 is in error; the actual value should be 100 mV/cm.

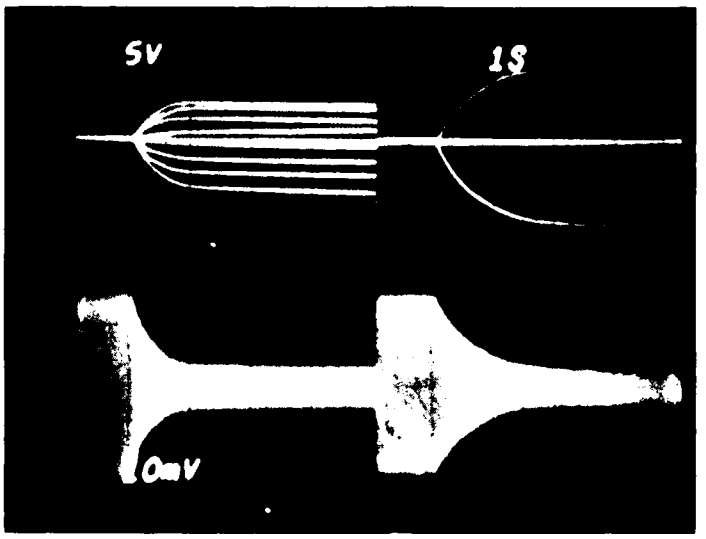

Figure 6-4. Transient Response for μ=1/320, Noise Case

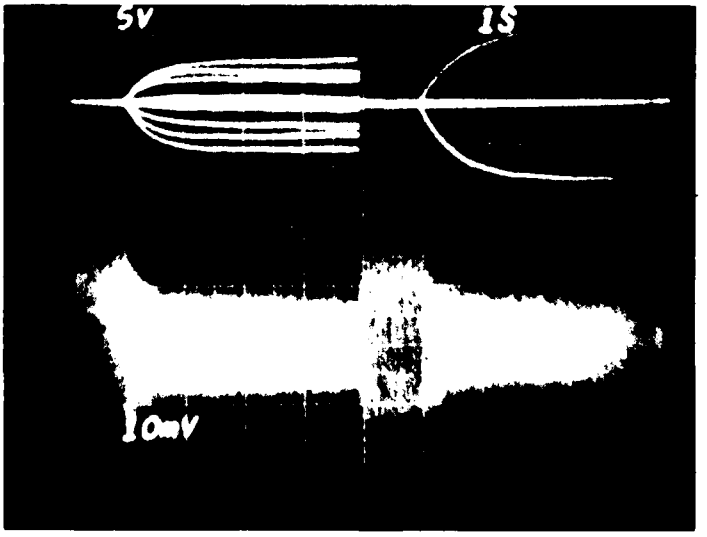

Figure 6-5. Transient Response for μ=1/320, SNR=10 dB, 5 kHz Noise Bandwidth

noise for the tap spacing employed. As can be seen, the adaptive weight convergence is not greatly affected and the output converges to essentially the noise level (31.6 mV rms ≅ 160 mV peak-to-peak).

Figure 6-6 shows the transient response for noise of 5 Hz bandwidth. The mean weight trajectory does not seem to be greatly affected by the correlation of the noise in this case.

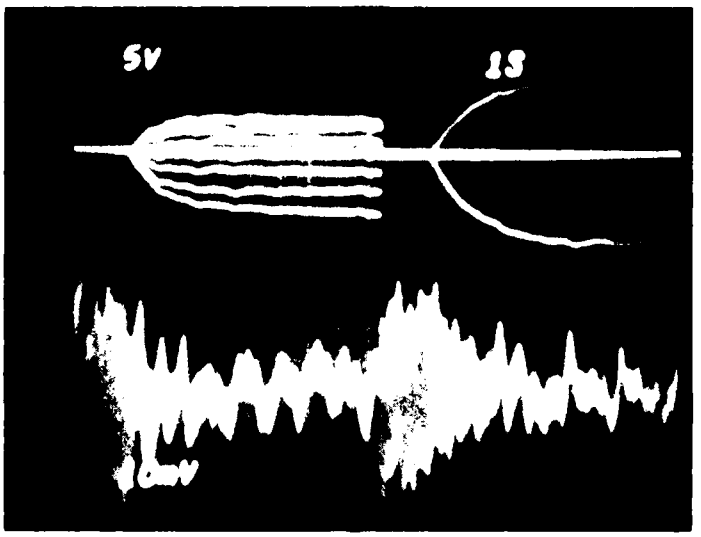

Figure 6-6. Transient Response for μ=1/320, SNR=10 dB, 5 Hz Noise Bandwidth

6.2 STEADY-STATE PERFORMANCE OF A REAL ADAPTIVE PROCESSOR IN A MULTI-PATH ENVIRONMENT

6.2.1 Introduction

The multiple "correlation cancellation loop" (CCL) [1],-[2] or "least-mean-square" (LMS) algorithm [3] [26] [27] technique is widely employed in adaptive arrays for radar, sonar, and communication systems as well as in many other signal processing applications, such as adaptive data compression [28], adaptive echo cancellation [29], adaptive equalization [30], adaptive noise cancellation [19], adaptive linear prediction [18] and adaptive multipath cancellation [31].

Typical radar systems employ multiple CCL's as sidelobe cancellers to null the effects of interfering signals. In some cases, the interfering signals are received over multiple transmission paths due to reflections from terrain features and/or man-made objects such as towers or buildings. Sidelobe cancellation in the multipath environment is then complicated by the increased degrees of freedom required to cancel each path. However, in this case, the multiple received signals are correlated in time and can therefore be removed by incorporating tapped delay lines in each auxiliary channel and providing an adaptive cancellation loop for each tap.

The question naturally arises as to what length of delay line and how many taps are required for effective cancellation of multipath narrowband or wideband interference. Several ad-hoc studies have been performed to partially answer this question for specific applications. However, no one to the authors' knowledge, has undertaken a definitive study of the problem or has derived any general guidelines to aid in this question. It is the purpose of this report to develop a methodology for dealing with this important problem and to provide a simple model for understanding the behavior of cancellation performance and how it relates to the various parameters involved.

It is emphasized that this study concerns the behavior of a CCL processor for real signals as opposed to complex baseband signals derived from in-phase and quadrature demodulation of a narrowband signal, as is usually encountered. The reason for this departure relates to the optical configuration of the AOAP, in which the optical analog signals are inherently real quantities. The "continuum" of signals or weights are contained on an optical traveling spatial carrier frequency, reflecting the character of the narrow band

signals being processed. In this way, the real-signal optical channel becomes equivalent to a complex signal processor, handling the equivalent of in-phase and quadrature components.

As will be seen, the chief distinction in this case is that more delay line taps must be employed for adequate quadrature sampling. This is, however, no hardship to bear for the AOAP which realizes an almost infinite effective number of taps, limited only by optical resolution.

The organization of this section is as follows: A brief description of the multiple CCL technique is given in Section 6.2.2. In Section 6.2.3, adaptive cancellation is studied for wideband and narrowband jammers in a single multipath environment. An impulse response model is also developed in order to qualitatively explain the performance. Section 6.2.4 presents a few representative computer simulation results and Section 6.2.5 contains conclusions and generalizations of the multiple CCL simulation study. Several appendices are included for various special analysis topics, additional simulation plots, and computer program listings.

6.2.2 General Theory

A diagram of a multiple real CCL processor to be used for interference cancellation in a radar or sonar system is shown in Figure 6-7. For simplicity, only a single auxiliary channel with multiple taps is considered here; the techniques and results derived can be readily extended to the multiple auxiliary case.

The output signal r(t) is formed by subtracting from the main input m(t) a weighted sum of N delayed versions of the auxiliary signal a(t), viz.,

$$r(t) = m(t) - \sum_{i=0}^{N-1} w_i \, a(t - iT/N), \qquad (6\text{-}24)$$

where T is the length of the delay line. Cancellation of the main signal is achieved by adjusting each adaptive weight so as to reduce the correlation between the corresponding delayed auxiliary signal and the residue. This procedure can be written as

$$\dot{w}_i(t) = \mu \, r(t) \, a(t-iT/N), \qquad (6\text{-}25)$$

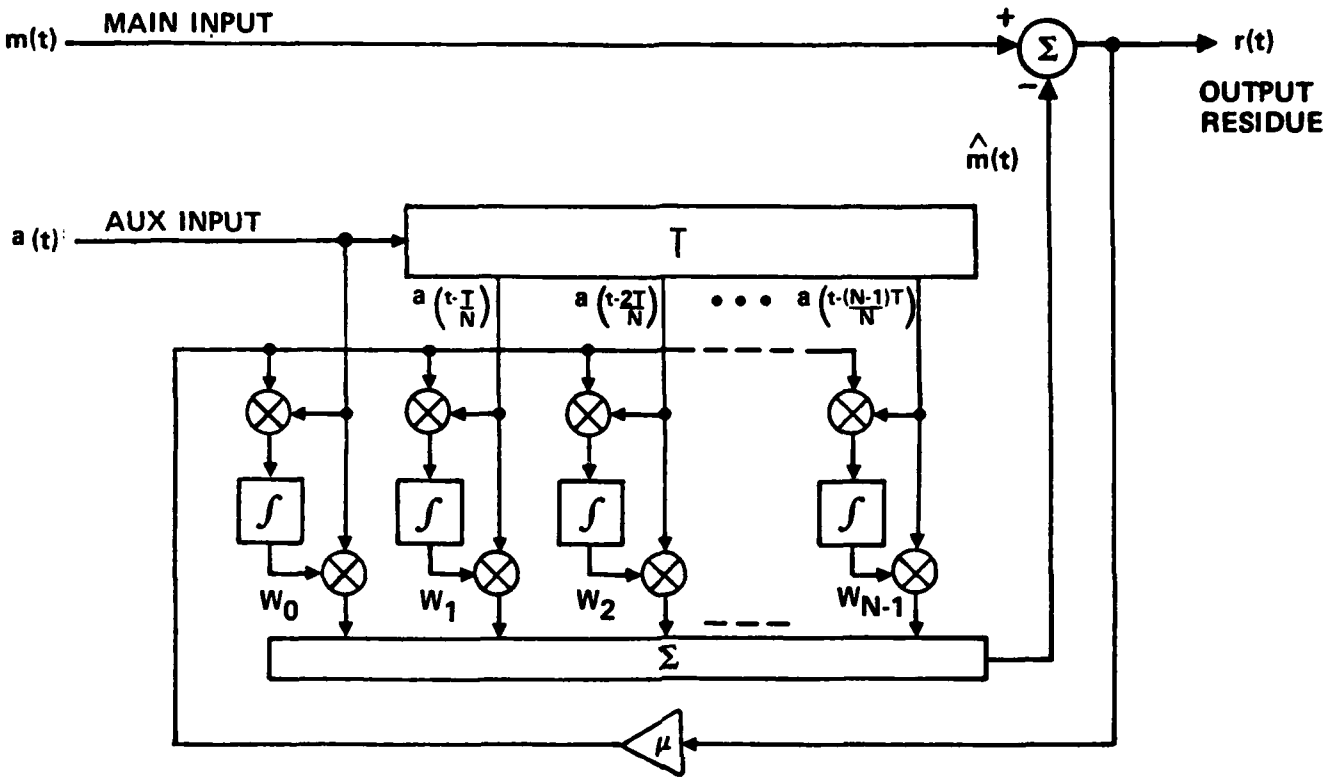

Figure 6-7. Adaptive Array Processor with a Single Auxiliary Tapped Delay Line

where μ is the loop gain constant. Adaptation then proceeds until the residue is uncorrelated with each auxiliary signal, i.e.,

$$E\{r(t)\ a(t-iT/N)\} = 0, \qquad i = 0,1,\ldots,N-1. \quad (6\text{-}26)$$

This process is equivalent to applying the orthogonality principle [23] which minimizes the rms residue power. Substitution of (6-24) into (6-26) then determines the optimal steady state adaptive weights (denoted by the subscript ∞) as the solution to

$$\sum_{j=0}^{N-1} r_{ij}\, w_{\infty j} = r_i \qquad i = 0,1,\ldots,N-1 \ , \tag{6-27}$$

where

$$r_{ij} = E\left[a\left(t - \frac{iT}{N} \right) a\left(t - \frac{jT}{N} \right) \right] \overset{\Delta}{=} R_a\left[(i-j)\, \frac{T}{N} \right] \tag{6-28a}$$

$$r_i = E\left[m(t)\, a\left(t - \frac{iT}{N} \right) \right] \overset{\Delta}{=} R_{ma}\left(- \frac{iT}{N} \right) \ , \tag{6-28b}$$

and $R_a(\tau)$ and $R_{ma}(\tau)$ are the autocorrelation and cross-correlation functions of the processes.

In matrix notation (6-27) becomes

$$\underline{R}\, \underline{w}_\infty = \underline{r} \ , \tag{6-29}$$

where $\underline{R}$ is the $N \times N$ auxiliary signal covariance matrix with elements r_{ij} and $\underline{r}$ is $N \times 1$ column matrix with elements r_i, appropriately defined in (6-28). Since uniform tap spacing was assumed, the matrix $\underline{R}$ is Toeplitz, i.e., its element values r_{ij} are a function of i-j only. Also, since $\underline{R}$ is a covariance matrix, it is positive definite and hence nonsingular. Therefore, a unique solution exists for the weight vector which can be obtained as

$$\underline{w}_\infty = \underline{R}^{-1}\, \underline{r}. \tag{6-30}$$

The most common computational approach in solving (6-29) is the Levinson-Robinson technique [32] which requires only $O(N^2)$ computations, and is the one employed here. However, for large N, R becomes so ill-conditioned that computations even with double precision computer arithmetic can at times lead to inaccurate results. Therefore, care must be exercised in applying these calculations.

6.2.3 Adaptive Cancellation in a Multipath Environment

6.2.3.1 General

A major goal of this report was to define a multipath interference cancellation test simulation that encompasses all the important parameters of the problem, yet is simple enough so that the effect of various parameters on the multiple CCL processor cancellation performance can be effectively studied.

A simplified system diagram in the presence of a wideband or narrowband jammer in a single multipath environment is shown in Figure 6-8. Each weight w_i is calculated by a correlation cancellation loop as shown in Figure 6-7, such that the output signal r(t) is uncorrelated with the delayed auxiliary signals a(t-iT/N), i=0,1,...,N-1. Without loss of generality, the noise entering the main channel can be neglected since it will be uncorrelated with the auxiliary signals and therefore will propagate, unaffected, to the output of the processor. The processor receiving front end contains a bandpass filter of bandwidth B and center frequency f_o such that the noise n(t) entering the auxiliary channel is colored with power spectrum $S_n(f)$ shown in Figure 6-8 and given as

$$S_n(f) = \frac{1}{B} \text{ rect } \left(\frac{f-f_o}{B}\right) , \qquad (6\text{-}31a)$$

where rect(x) is defined as

$$\text{rect}(x) \overset{\Delta}{=} \begin{cases} 1 & |x| < 1/2 \\ 0 & |x| > 1/2 \end{cases} .$$

Taking the inverse Fourier transform of the power spectrum then gives the noise autocorrelation function

$$R_n(\tau) = \text{sinc } B\tau \cos \omega_o \tau , \qquad (6\text{-}31b)$$

where $\omega_o = 2\pi f_o$, sinc(x) is defined as

$$\text{sinc}(x) \overset{\Delta}{=} \frac{\sin \pi x}{\pi x} ,$$

and for convenience the noise power is normalized to unity, i.e., $R_n(0) = 1$.

The received signal in the main channel m(t) is given by

$$m(t) = s(t) + \alpha_m \, s(t-\tau_o) \qquad (6\text{-}32)$$

where α_m is the multipath component strength (normally $\alpha_m < 1$) and τ_o is the excess time delay relative to the direct path. The corresponding received signal in the auxiliary channel is given by

$$a(t) = s(t) + \alpha_a \, s(t-\tau_o-\tau_1) + n(t), \qquad (6\text{-}33)$$

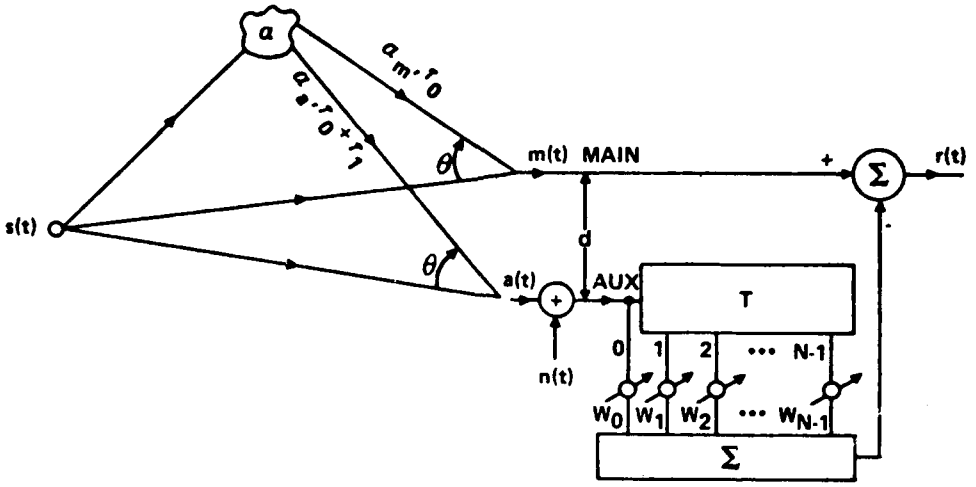

(a)

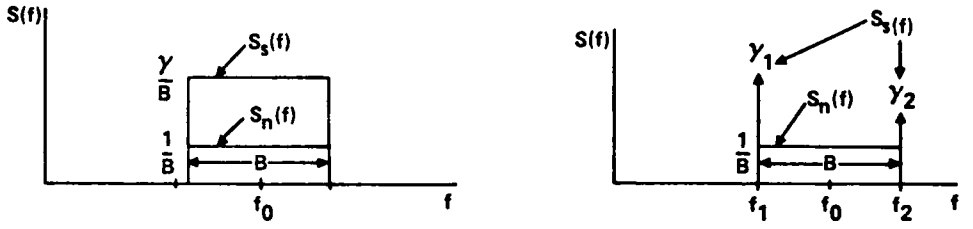

(b)

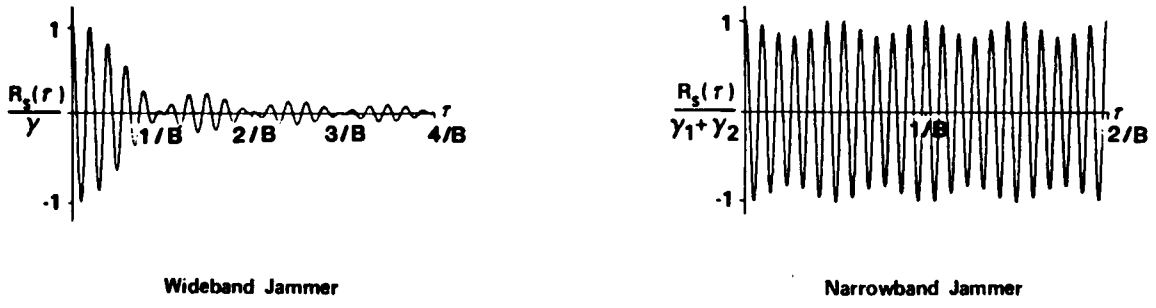

(c)

Figure 6-8. Simplified Adaptive Array Processor in Multipath Environment. (a) Block Diagram, (b) Noise and Jammer Spectra, and (c) Autocorrelation Functions

where α_a is the multipath component strength (normally $\alpha_a<1$), and

$$\tau_1 = \frac{d}{c} \sin\theta \qquad (6\text{-}34)$$

is the delay across the array, with θ being the angle between the direct and received signal components, c, the propagation velocity, and d the separation of the two antennas. Note that in general $\alpha_a \neq \alpha_m$ since the main antenna is typically of high gain with a narrow mainlobe, whereas the auxiliary antenna has an omnidirectional pattern.

Elementary calculations with (6-32) and (6-33) determine the main and auxiliary channel autocorrelation and cross-correlation expressions as

$$R_m(\tau) \stackrel{\Delta}{=} E\{m(t)m(t+\tau)\}$$

$$= (1+\alpha_m^2)R_s(\tau) + \alpha_m R_s(\tau-\tau_o) + \alpha_m R_s(\tau+\tau_o) \qquad (6\text{-}35)$$

$$R_a(\tau) \stackrel{\Delta}{=} E\{a(t)a(t+\tau)\}$$

$$= (1+\alpha_a)^2 R_s(\tau) + \alpha_a R_s(\tau-\tau_o-\tau_1) + \alpha_a R_s(\tau+\tau_o+\tau_1) + R_n(\tau) \qquad (6\text{-}36)$$

and

$$R_{ma}(\tau) \stackrel{\Delta}{=} E\{m(t)a(t+\tau)\}$$

$$= R_s(\tau) + \alpha_a R_s(\tau-\tau_o-\tau_1) + \alpha_m R_s(\tau+\tau_o) + \alpha_m\alpha_a R_s(\tau-\tau_1) , \qquad (6\text{-}37)$$

where $R_s(\tau)$ is the autocorrelation function of the interference signal s(t). A solution for the steady state vector $\underline{w}_\infty$ is then obtained from (6-27)-(6-30) and (6-36)-(6-37).

An expression for the total steady-state output power is obtained from (6-24) as

$$P_r = E\{[m(t) - \sum_{i=0}^{N-1} w_i\, a(t-iT/N)]^2\} \qquad (6\text{-}38a)$$

$$= P_m + \sum_{i=0}^{N-1}\sum_{j=0}^{N-1} w_i w_j R_a[(i-j)T/N] - 2\sum_{i=0}^{N-1} w_i R_{ma}\left(\frac{-iT}{N}\right) , \qquad (6\text{-}38b)$$

where $P_m = R_m(0)$ is the power in the main channel, and R_a and R_{ma} are defined in (6-36) and (6-37). In vector form, (6-38) can be expressed as

$$P_r = P_m + \underline{w}^T (\underline{R}\,\underline{w} - 2\,\underline{r}),$$

where use of (6-28) was employed. The residue power is minimized for $\underline{w} = \underline{w}_\infty$ as defined in (6-29) giving

$$P_{r_{min}} = P_m - \underline{w}_\infty{}^T\,\underline{r}\ . \qquad (6\text{-}39)$$

6.2.3.2 Wideband Jammer

For a wideband jammer, the interfering signal s(t) can be represented as a random process with a flat bandpass power spectrum

$$S_s(f) = \frac{\gamma}{B}\ \text{rect}\left(\frac{f-f_o}{B}\right) \qquad (6\text{-}40a)$$

as shown in Figure 6-8. Its corresponding autocorrelation function $R_s(\tau)$, which is the inverse Fourier transform of $S_s(f)$, is given by

$$R_s(\tau) = \gamma\ \text{sinc}\ B\tau\ \cos\omega_o\tau\ . \qquad (6\text{-}40b)$$

6.2.3.3 Narrowband Jammer

Under the narrowband jammer assumption, the interfering signal s(t) is represented as two sinusoids of corresponding signal-to-noise power ratios γ_1, γ_2, that is,

$$s(t) = \sqrt{2\gamma_1}\cos\omega_1 t + \sqrt{2\gamma_2}\cos\omega_2 t\ , \qquad (6\text{-}41)$$

where $f_1 = \omega_1/2\pi$, $f_2 = \omega_2/2\pi$ are frequencies contained in the bandpass filter of bandwidth B. The corresponding one-sided power spectrum is given as

$$S_s(f) = \gamma_1\delta(f-f_1) + \gamma_2\delta(f-f_2)\ . \qquad (6\text{-}42a)$$

Taking the inverse Fourier transform of the two-sided power spectrum, the autocorrelation function $R_s(\tau)$ is given as

$$R_s(\tau) = \gamma_1\cos\omega_1\tau + \gamma_2\cos\omega_2\tau\ . \qquad (6\text{-}42b)$$

The total output power can be obtained as in (6-38)-(6-39). However, in this case, an alternate expression can be obtained by substituting (6-32), (6-33), (6-41) in (6-38a) and taking Fourier transforms, giving

$$P_r = P_{r_1} + P_{r_2} + P_{r_o} \quad , \tag{6-43}$$

where

$$P_{r_k} = \gamma_k \left| 1 + \alpha_m e^{-j\omega_k \tau_o} - \sum_{i=0}^{N-1} w_i \left[e^{-j\omega_k \frac{iT}{N}} + \alpha_a e^{-j\omega_k \left(\frac{iT}{N} + \tau_o + \tau_1 \right)} \right] \right|^2 , \quad k=1,2 \tag{6-44}$$

are sinusoidal components of the output power and

$$P_{r_o} = \sum_{i=0}^{N-1} \sum_{j=0}^{N-1} w_i \, w_j \, R_n \left[(i-j) \, T/N \right] \tag{6-45}$$

is the noise output power. The function $R_n(\tau)$ in (6-45) is evaluated using (6-31).

6.2.3.4 Impulse Response Model

An equivalent representation of (6-32), (6-33) is given as

$$m(t) = s(t) * h_m(t) \tag{6-46a}$$

$$a(t) = s(t) * h_a(t) + n(t) \quad , \tag{6-46b}$$

where

$$h_m(t) = \delta(t) + \alpha_m \delta(t - \tau_o) \tag{6-47a}$$

$$h_a(t) = \delta(t) + \alpha_a \delta(t - \tau_o - \tau_1) \tag{6-47b}$$

represent the corresponding main and auxiliary channel impulse responses. The corresponding channel frequency responses $H_m(f)$, $H_a(f)$ are the Fourier transforms of $h_m(t)$, $h_a(t)$ in (6-47), and are given as

$$H_m(f) = 1 + \alpha_m e^{-j\omega\tau_o} \qquad (6\text{-}48a)$$

and

$$H_a(f) = 1 + \alpha_a e^{-j\omega(\tau_o + \tau_1)} , \qquad (6\text{-}48b)$$

where $\omega = 2\pi f$.

An ideal processor with knowledge of the channel frequency responses $H_m(f)$ and $H_a(f)$ would process the auxiliary signal a(t) by first applying the inverse filter H_a^{-1} in order to remove the effect of multipath in the auxiliary, and then apply the filter H_m to introduce the multipath components associated with the main signal m(t). Thus, the composite filter that would be applied to the auxiliary signal can be written

$$H(f) = H_a^{-1}(f)\, H_m(f), \qquad (6\text{-}49a)$$

or in the time domain

$$h(t) = h_a^{-1}(t) * h_m(t). \qquad (6\text{-}49b)$$

Finally, subtraction of the resultant signal from m(t) would give the output signal r(t) as shown in Figure 6-9. Also shown are the corresponding filter impulse responses $h_m(t)$, $h_a(t)$, $h_a^{-1}(t)$ and h(t), where

$$h_a^{-1}(t) = F^{-1}[H_a^{-1}(f)] = \sum_{n=0}^{\infty} (-\alpha_a)^n \, \delta[t - n(\tau_o + \tau_1)] \, . \qquad (6\text{-}50)$$

For $\tau_1 = 0$, substitution of (6-50) and (6-47a) into (6-49b) gives

$$h(t) = \delta(t) + (\alpha_m - \alpha_a) \sum_{n=1}^{\infty} (-\alpha_a)^{n-1} \, \delta(t - n\tau_o) \, . \qquad (6\text{-}51)$$

This response will be appropriate as an approximation to the ideal filter for an actual system if $B\tau_1 << 1$, a condition that is almost always realized in practice.

The actual adaptive CCL processor on the other hand has no knowledge of the channel filters H_m and H_a but adapts the weights w_i such that the estimate

$$m(t) = \sum_{i=0}^{N-1} w_i \, a\left(t - \frac{iT}{N}\right)$$

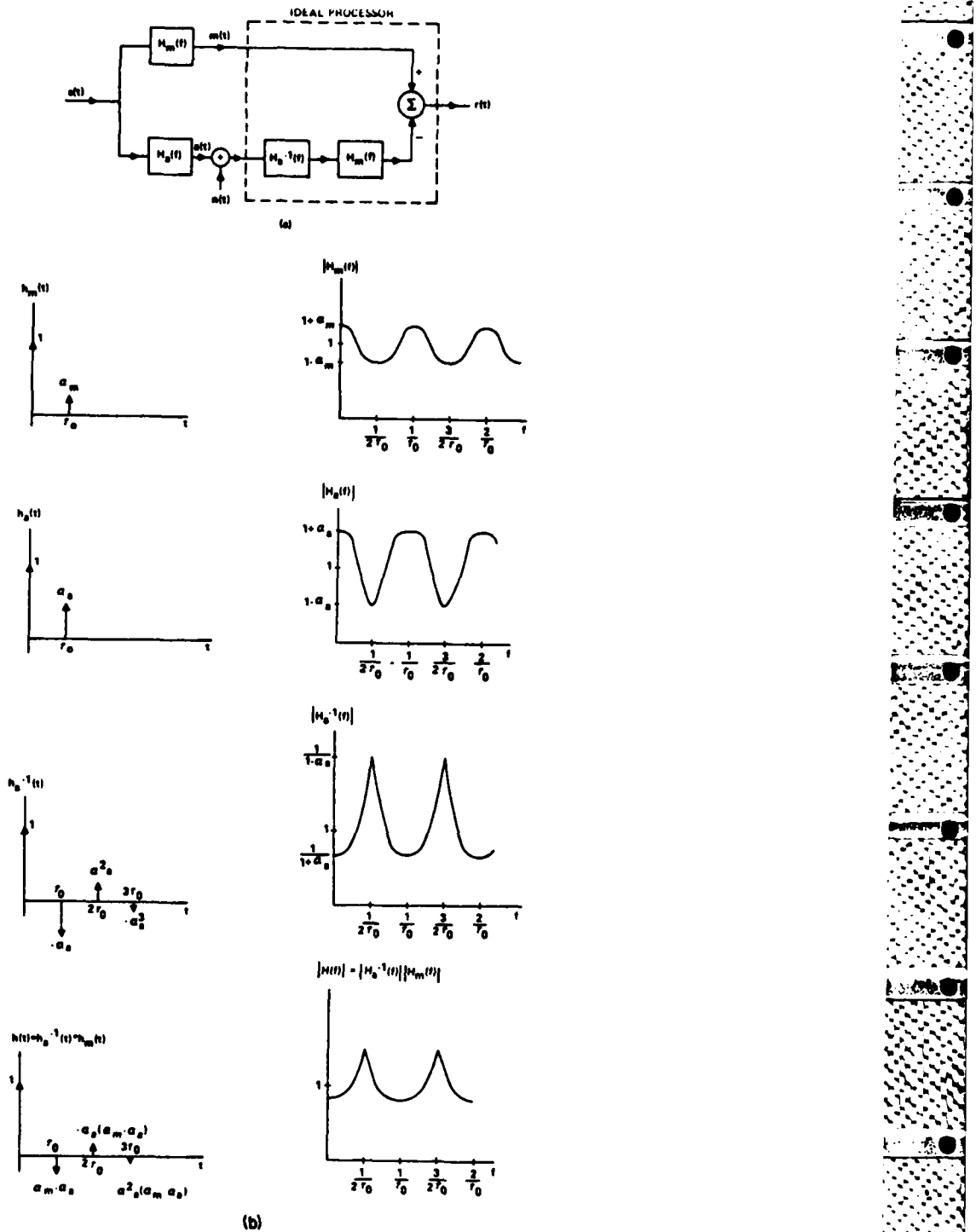

Figure 6-9. Ideal Multipath Cancellation System. (a) Block Diagram, (b) Filter Impulse Responses

is optimum in the sense of minimizing the mean-squared error. In the absence of multipath, the steady state performance of the processor would be the limiting behavior of (6-39), being a function of the jammer signal s(t), and the number of adaptive taps N. In the presence of multipath, the processor in essence approximates the impulse response of the infinite impulse response (IIR), or recursive, filter of (6-51) with the finite impulse response (FIR), or nonrecursive, N tap filter

$$\hat{h}(t) = \sum_{i=0}^{N-1} w_i \, \delta\left(t - \frac{iT}{N}\right). \tag{6-52}$$

Thus, the problem can be visualized as matching $\hat{h}(t)$ to h(t) such that the output power is minimized.

Comparison of (6-51) with (6-52) shows that the best filter match that can be achieved is when $\hat{h}(t) = h(t)$, $0 < t < T$. This ideal will be approximately realized if the number of taps N is large enough for good interpolation of the multipath signal components located at multiples of τ_o*. Thus, under these conditions, and neglecting the additive noise, the residue will be approximated by the expression

$$\begin{aligned} r(t) &\cong m(t) - \hat{h}(t) * a(t) \\ &= [h(t) - \hat{h}(t)] * a(t) \\ &\cong (\alpha_m - \alpha_a) \sum_{n=M+1}^{\infty} (-\alpha_a)^{n-1} \, a(t - n\tau_o) \quad , \end{aligned} \tag{6-53}$$

where M is a function of τ_o defined by

$$M\tau_o < T < (M+1)\tau_o \, , \tag{6-54a}$$

i.e.,

$$M = [T/\tau_o] \tag{6-54b}$$

where $[x]$ is defined as the greatest integer less than or equal to x.

---

* An analysis of interpolation of a bandlimited random process appears in Appendix B.

The residue power can then be expressed using (6-53) as

$$P_r = E\{r^2(t)\}$$

$$\cong (\alpha_m-\alpha_a)^2 \sum_{n,m=M}^{\infty}\sum (-\alpha_a)^{n+m} R_a[(n-m)\tau_o] \qquad (6\text{-}55a)$$

$$= \alpha_a^{2M} \frac{(\alpha_a-\alpha_m)^2}{1-\alpha_a^2}\left[P_a + 2\sum_{p=1}^{\infty}(-1)^p \cosh(p\,\ell n\alpha_a) R_a(p\tau_o)\right], \qquad (6\text{-}55b)$$

where R_a is defined in (6-36).

Examination of (6-55) shows that this expression can be usefully applied to determine most of the behavioral characteristics of adaptive cancellation in multipath. First of all, it can be seen that in the unlikely event that $\alpha_m = \alpha_a$, the residue power reduces to zero as would be expected since both signals are exactly matched. Furthermore, if $\alpha_a = 0$, P_r also reduces to zero as would be expected since in this case there is no inverse auxiliary multipath filter to approximate.

A special case of the above for the wideband jammer occurs for $B\tau_o >> 1$ and $\tau_1 = 0$, for which

$$R_a[(n-m)\tau_o] \cong [(1+\alpha_a^2)\delta_{mn}+\alpha_a\delta_{m,n+1}+\alpha_a\delta_{m,n-1}]\,P_s, \quad B\tau_o>>1, \qquad (6\text{-}56)$$

and therefore, (6-55) reduces to

$$P_r \cong \alpha_a^{2M}(\alpha_m-\alpha_a)^2 P_s, \quad B\tau_o>>1. \qquad (6\text{-}57)$$

In this case, the residue power will increase from one plateau to the next as τ_o is increased, where each successive level change occurs with an integer value change of $M=[T/\tau_o]$. A non-mathematical way of viewing this behavior is to realize that the approximating FIR filter $\hat{h}$ is equivalent to the IIR filter h depicted in Figure 6-9 over a window of fixed length T. Thus, as τ_o is increased, the number of impulses contained in the window will fall off one-by-one. These transitions will occur for τ_o/T = 1, 1/2, 1/3, 1/4,..., i.e., where M changes value.

For any given application, (6-57) can be utilized to specify the length of delay line required for effective cancellation of multipath interference of given maximum delay and strength. Note that it is generally not sufficient to employ a delay line whose length merely equals the longest multipath delay. As an example, consider a multipath of strength $\alpha_a = 0.5$ (-6 dB) in the auxiliary antenna and (as a worst case) $\alpha_m = 0$ in the main antenna. For these parameters, the cancellation ratio is then

$$\frac{P_r}{P_s} = 2^{-2[T/\tau_o+1]} , \qquad (6\text{-}58)$$

i.e., 6 dB for each multiple of T to τ_o. Thus, in the absence of noise, 30 dB of cancellation would require $T > 5\ \tau_o$, i.e., the required delay is five times the longest multipath delay.

6.2.4 Computer Simulation Results

6.2.4.1 Wideband Jammer

A computer program was written to evaluate the performance of a single auxiliary channel, tapped delay CCL processor in regard to its ability to cancel a wideband jammer signal in a single multipath environment. The program was written in FORTRAN IV code and was compiled and executed on a VAX-II computer. All plots were generated on a PLXY plotter. Equations (6-28), (6-35)-(6-38) were written in FORTRAN code and the values of the weight vectors in (6-30) were obtained not by matrix inversion but by the Levinson-Robinson algorithm which requires only 0 (N^2) computations [32].

Referring to the simplified system diagram of Figure 6-8, the simulation parameters are the system bandwidth B, center frequency f_o, jammer power γ (also power to noise ratio since the noise power is normalized), multipath components strengths α_m and α_a, excess multipath delay in the auxiliary channel τ_1, total auxiliary delay T, and number of adaptive taps N. A set of nominal dimensionless parameters values was selected as $BT = 2$, $f_oT = 10$, $\tau_1/T = 10^{-3}$, $\gamma = 1000$ (30 dB), corresponding to B = 20 MHz, $f_o = 100$ MHz, T = .1 μsec, $\tau_1 = 10^{-4}$ μsec* and $\alpha_a, \alpha_m = 0, .5, 1$. Plots of P_r(dB) vs. $\tau_o/T = 0, .01, .02, \ldots, 1.8$ for N = 4,8,16,32,64 were generated.

---

*This corresponds to an angle $\theta \simeq 2°$ in Figure 6-8 for an antenna separation of 1m.

Initial runs using single precision arithmetic resulted in poor accuracy for N > 8. Therefore all calculations were done in double precision arithmetic. An additional problem was experienced for large values of N, whereby the covariance matrix $\underline{R}$ of (6-28a) used in (6-29) becomes highly ill-conditioned, due to a high ratio of largest to smallest eigenvalues of $\underline{R}$. This ratio of largest to smallest eigenvalues is sometimes referred to as the condition number of a matrix and can be related to the spectral variation of the sampled power spectrum [33] [20],

$$S_a'(f) = \sum_{n=-\infty}^{\infty} S_a(f-nN/T) \ . \qquad (6\text{-}59)$$

For a bandpass spectrum, there is no overlap in (6-59) for N > BT, and hence the eigenvalue spread is unbounded and the matrix is inherently ill-conditioned. The ratio of spectral variation will also be large for $\alpha_a \approx 1$ due to multipath cancellation of some frequency components.

To counteract the ill-conditioning of $\underline{R}$ which results in inaccuracies in P_r, a small value ΔR was added to the diagonal elements of $\underline{R}$. An optimum value of

$$\Delta R \cong 10^{-9}$$

was determined empirically.

A plot of P_r (dB) versus τ_o/T for α_m=0, α_a=.5 and N=4,8,16,32,64 is shown in Figure 6-10. From sampling theory, it is known* that for an infinite number of samples, optimum performance in P_r will be obtained provided the sampling rate ($R_s = N/T$) is greater than the Nyquist rate, which is defined as twice the largest significant frequency in the signal spectra ($R_N = 2f_o + B$). The deterioration in performance for a finite number of samples that is progressively getting smaller is addressed in detail in Appendix B. From Figure 6-10 it is seen that for $\tau_o/T<.3$, near-optimum performance is attained for as few as N=16 taps, corresponding to a relative sampling ratio

$$\frac{R_s}{R_N} = \frac{N}{2\ f_o T + BT} = \frac{16}{2(10) + 2} = 0.73 \ .$$

Also, the performance degradation due to increasing multipath delay length τ_o is evident as predicted by (6-55).

---

* The relationship of sampling theory to the multipath cancellation problems was suggested by Dr. Frank Dickey of the General Electric Co., Syracuse, N. Y.

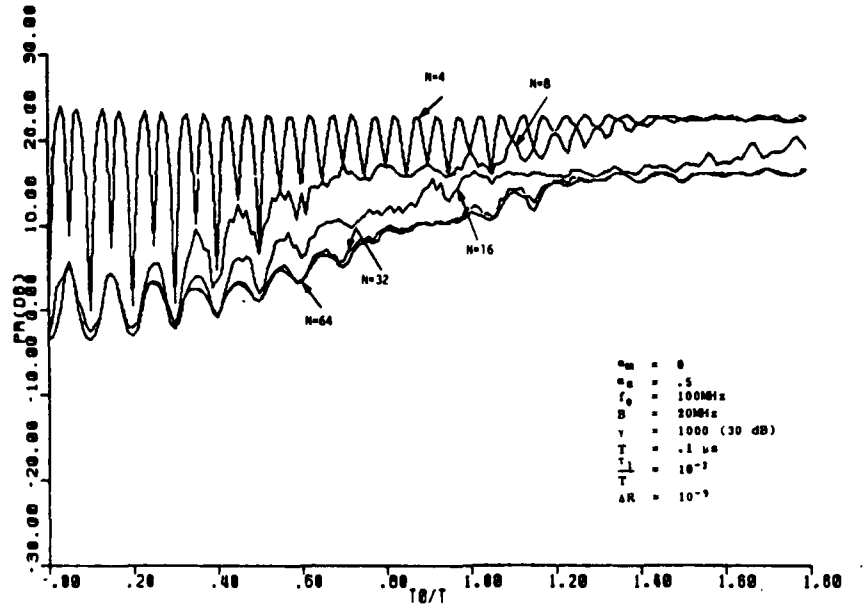

Figure 6-10. Output Residue Power vs. Normalized Multipath Delay for a Wideband Jammer and T = 0.1 μsec.

The fine structure in the response is due to spectral interference of the multipath components. As shown in Figure 6-9, the auxiliary channel response $H_a(f)$ contains peaks at integer multiples of $1/\tau_o$. Therefore, the auxiliary bandpass signal spectrum will be enhanced by the multipath if τ_o/T is an integer multiple of $1/f_oT = 0.1$ and hence improve performance at these points. Thus, the valleys in Figure 6-10 for large N which occur for $\tau_o/T = 0.1, 0.2, \ldots$ are a result of auxiliary signal enhancement. On the other hand, for points in between $\tau_o/T = .05, .015, \ldots$, auxiliary signal is reduced, thereby increasing the residue power, and is also evident in Figure 6-10.

Another plot is shown in Figure 6-11 for all the same parameters as in Figure 6-10 except that the length of the delay line is increased by a factor of 8 to T = 0.8 μs. It is expected that the P_r response for N=64,128 will be at least as good as the one for N=8,16 of Figure 6-10 since the sampling rate is the same, although more total taps have now been added. In fact it is noted that the P_r response in Figure 6-11 has now achieved its limiting behavior for N=64 or a relative sampling ratio

$$\frac{R_s}{R_N} = \frac{64}{2(80) + 16} = 0.36 \ ,$$

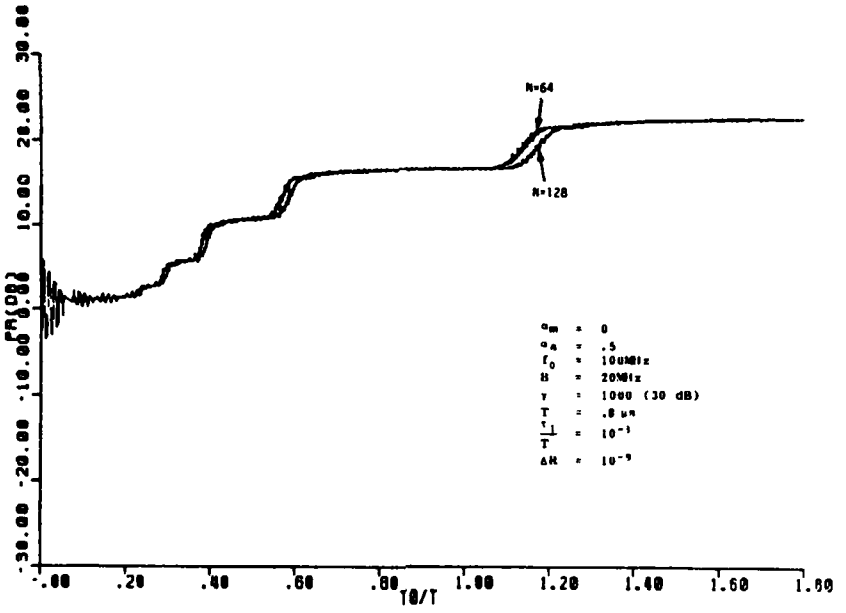

Figure 6-11. Output Residue Power vs. Normalized Multipath Delay for a Wideband Jammer and T = 0.8 μsec

as opposed to the Figure 6-10 P_r response achieving its limiting behavior at R_S = .73 R_N (N=16). The limiting performance of the P_r response of Figures 6-10 - 6-11 can be explained in terms of the taps occurring in quadrature pairs.*

The first four cycles of the fine structure in Figure 6-11 are similar to Figure 6-10 over an absolute time delay interval of $0 < \tau_o < 0.05$, as would be expected. For larger delay, the plateauing effect predicted by (6-57) is clearly evident. The entire response in fact is very close to that predicted by the impulse response model, whereby the residue jumps in 6 dB steps for τ_o/T = 1,1/2,1/3,1/4,... and eventually reaches a level of 1000/4 (24 dB). Actually each plateau holds on a little longer than expected because of the ability to predict the signal value somewhat beyond the length of the delay line.

---

* The effect of quadrature tap spacing on the processor performance is analyzed in Appendix C.

6.2.4.2 Narrowband Jammer

The effect of multiple narrowband jammers distributed over a band of frequencies will now be examined. The simplest situation to consider is two sinusoidal jammers located at the band edges. Referring to Figure 6-8, the additional simulation parameters required to specify the two tone jammer are the frequencies f_1, f_2 and the corresponding signal strengths (signal to noise power ratios) γ_1, γ_2. The nominal dimensionless parameters that were selected are $f_1 T = 9$, $f_2 T = 11$, $\gamma_1 = 1000$ (30 dB) and $\gamma_2 = 100$ (20 dB), corresponding to $f_1 = 90$ MHz, $f_2 = 110$ MHz for $T = 0.1$ μsec.

A plot of P_r versus τ_o/T for $\alpha_m = 0$, $\alpha_a = .5$, $T=0.1$ μsec and $N=4,8,16,32,64$ is shown in Figure 6-12. The ripples in these plots can be explained by interference of the direct and multipath sinusoids at the main and auxiliary antennas: variations of signal level at the main input will of course directly translate to the output; on the other hand, variations at the auxiliary input will affect the SNR, thereby enhancing or degrading the cancellation performance.

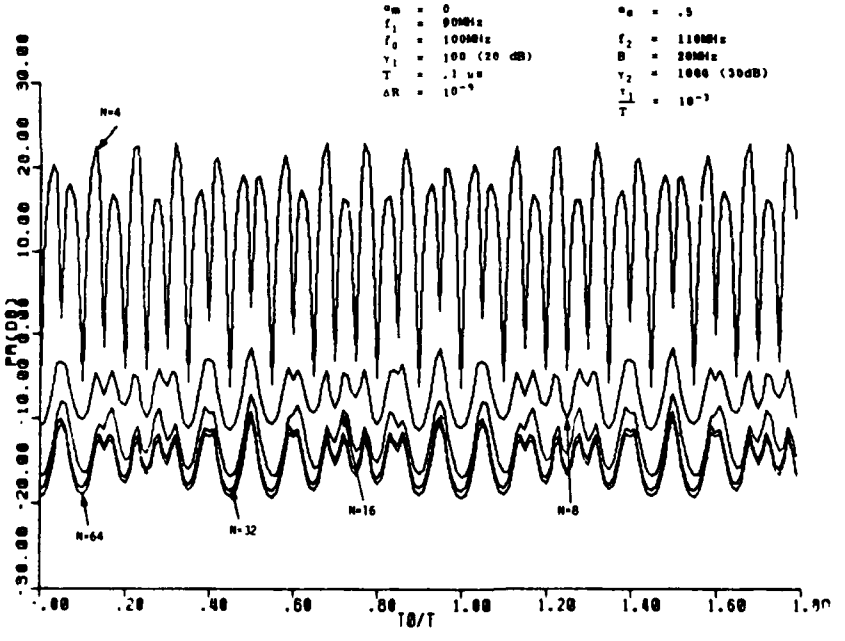

Figure 6-12. Output Residue Power vs. Normalized Multipath Delay for a Narrowband Jammer and T = 0.1 μsec.

Another point of interest concerning Figure 6-12 is that the plot is periodic, repeating at $\tau_o/T = 1.0$ since each sinusoid has then gone through an integer number of cycles, viz., $f_1\tau_o = 9$ and $f_2\tau_o = 11$.

As can be seen, contrary to the wideband case, the performance with the narrowband jammer does not degrade as τ_o is increased. This behavior is a consequence of the periodic nature of the signal autocorrelation function. Therefore, in this case, it is not necessary to have a delay line length which exceeds the longest multipath delay as was the case for wideband interference; the delay only has to encompass one period of the autocorrelation function envelope. For the case of two sinusoids, this period for the particular parameters chosen is given simply by $T=2/(f_2-f_1)$, which is equal to 0.1 μsec for the previous example.

Further examination of Figure 6-12 shows that near-optimum performance is attained for a normalized sampling rate

$$\frac{R_s}{R_N} = \frac{N}{2f_oT + BT} = \frac{32}{2(10)+2} = 1.46$$

corresponding to N = 32, as compared to the value $R_S/R_N = .73$ required for wideband jammer cancellation shown in Figure 6-10. However, in this case, the limiting residue power is much lower since the sinusoidal signals are correlated over the entire delay line, thereby distributing the noise power over a larger number of adaptive weights. In fact, the average near-optimum output power for the narrowband jammer is approximately 15 dB lower than the corresponding wideband power for approximately equal jammer signal strength ($\gamma_1 + \gamma_2 = 30.4$ dB, whereas $\gamma = 30$ dB). All of this seems to suggest that wideband jamming is the most difficult problem to be solved, presumably due to the higher number of degrees of freedom involved.

6.2.5 Conclusions

The steady-state cancellation performance of an adaptive array processor using a single, real, auxiliary tapped delay line with a multiple CCL has been analyzed for a single multipath interference environment. Both wideband random noise jammers and multiple narrowband jammers were considered. The techniques and results developed can be easily extended to multiple auxiliary channels and multiple multipath components.

For all types of interferences good cancellation is generally achieved provided that the auxiliary signal delay line taps are spaced closer than dictated by the Nyquist sampling rate. For the wideband jammer, near-optimum performance was attained in some cases at half the Nyquist sampling rate or less due to the taps occurring in quadrature pairs.

For small multipath delay, $B\tau_o << 1$, the CCL processor responses were explained in terms of auxiliary or main signal enhancement or reduction due to multipath. An impulse response model was developed to qualitatively explain the system behavior for large multipath delay, $B\tau_o >> 1$. This model relates the performance to a processor which employs a finite impulse response (FIR) filter in the auxiliary channel to match an ideal infinite impulse response (IIR) filter that would be required for exact cancellation.

For the wideband jammer, good cancellation is obtained, provided that the length of the delay line T is considerably longer than the longer multipath delay τ_o, depending on multipath components strengths of the main and auxiliary channels, denoted by α_m and α_a respectively. For large multipath delays, $B\tau_o >> 1$, the limiting output residual power can be simply expressed using this model as

$$P_r \cong \alpha_a^{2M} (\alpha_m - \alpha_a)^2 P_s ,$$

where P_s is the jammer signal power and $M = [T/\tau_o]$ is the number of integer multiples of τ_o contained in the total delay T.

For narrowband jamming, the cancellation performance was shown to be unaffected by τ_o provided that the delay line exceeds the period of the autocorrelation function.

In all cases, the effect of the auxiliary channel excess multipath delay length τ_1 on the processor performance is minimal since it merely shortens the effective delay length to $T - \tau_1 \approx T$ for $\tau_1 << T$, and is negligible for any practical application.

The main results of this report concern the performance of real multiple CCL, which relates to a specific hardware application. In general, adaptive cancellation systems process complex signals derived from in-phase and quadrature demodulation of a narrowband signal. The present analysis approach could be modified to accommodate this situation by redefining all signals as complex quantities and by employing complex arithmetic in solving for the steady-state residue power.

APPENDIX A

ADDITIONAL SIMULATION RESULTS

Additional simulation results are contained in this Appendix which further demonstrates the behavior of the processor cancellation performance in a multipath environment, as a function of the various system parameters. Plots of processor output power P_r (dB) versus normalized multipath delay τ_o/T for a wideband jammer are shown in Figures A1-A16, and the corresponding values of the system parameters are summarized in Table AI.

TABLE AI. WIDEBAND JAMMER SYSTEM PARAMETERS

Fig.#	f_0 (MHz)	B(MHz)	γ	α_m	α_a	T(μsec)	τ_1/T	ΔR	N
A1	100	20	1000	1	1	.1	10^{-3}	10^{-9}	8,16, 32,64
A2				.5	1				
A3				0	1				
A4				1	.5				
A5				.5	.5				
A6				0	.5				
A7				1	0				
A8				.5	0				
A9				0	0				
A10				0	.5		0		
A11							.1		
A12							.5		
A13							1		
A14							10^{-3}	0	
A15	60	10					10^{-3}	10^{-9}	
A16	60	10				.8	10^{-3}	10^{-9}	64,128

The plots in Figures A1-A9 demonstrate the effect of the multipath component strengths for $\alpha_m = \alpha_a = 0, .5, 1$ on the P_r response. As discussed in the main body of this report, the multiple CCL processor in the presence of multipath approximates the impulse response of an infinite impulse response (IIR) deconvolution filter with one of a finite impulse response (FIR) filter. As predicted by (6-55) and demonstrated by Figures A2-A3, this approximation is hopeless for $\alpha_a = 1$, since the deconvolution filter has a constant infinite impulse response. In the unlikely event that $\alpha_m = \alpha_a$, the residue power contains no signal component as predicted by (6-55) and, thus, reduces to the auxiliary noise level as seen in Figures A1, A5 and A9. The similarity of the P_r responses in Figures A4 and A6 can be easily

explained by (6-55) since $|\alpha_m - \alpha_a|$ is the same for both cases. In the absence of the auxiliary multipath component (α_a=0), the processor task is much easier, since it does not now have to synthesize the impulse response of an IIR filter, but simply introduces the main multipath component in the auxiliary. Thus, good cancellation performance is possible in this case as evidenced in Figures A7-A8. The behavior of the residue power in Figures A7-A8 for $\tau_o/T > 8$ can be explained in terms of good extrapolation being possible provided the number of taps N is large enough*. The nominal parameter values α_m=0, α_a=.5 were selected, and the remaining plots are variations of this case.

The effect of the delay across the array τ_1 on the P_r response is shown in Figures A10-A13. As can be seen, the result is essentially to shorten the delay line to an effective length $T-\tau_1$. Thus, the last three plots are similar to Figure A6 shifted to the left by the amount τ_1/T and the Figure A10 plot is essentially the same as the Figure A6 plot. Therefore, for the usual system condition $\tau_1 << T$, the effect of τ_1 is minimal and without loss of generality τ_1 could be set to 0.

The response of Figure A14 demonstrates the ill-conditioned nature of the covariance matrix $\underline{R}$ of (6-29) for large N and the resulting numerical inaccuracies when no small term (ΔR=0) is added to its diagonal elements to correct the situation. Superposition of Figure A14 on Figure A6 shows that adding $\Delta R = 10^{-9}$ to the diagonal of $\underline{R}$ has introduced an error less than 1 dB for large τ_0/T and significantly less than that for small τ_0/T.

The responses of Figures A15-A16 are similar to the ones of Figures 6-10 - 6-11 in the main body of the report, and they demonstrate the effect of increasing the length of the delay line by a factor of 8 to T=.8 μsec for the system parameters f = 60 and B = 10 MHz.† Note again that as predicted by sampling theory, the P_r responses in Figure A16 for N=64,128 are at least as good as the ones in Figure A15 for N=8,N=16. Also note the plateauing effect in Figure A16 occurring in 6 dB steps for $\tau_0/T \cong 1, 1/2, 1/3, 1/4, \ldots$, as predicted by (6-57).

The final plot for the wideband jammer in Figure A17 demonstrates the effect of adding a delay line of length T/2 in the main channel. In the absence of auxiliary multipath this would be highly desirable in order to provide good

---

* This is one of the results of Appendix B.

† The experimental AOAP laboratory implementation is being designed for f = 60, B = 10 MHz and T = 7 μsec.

interpolation* of the main signal multipath. However, for wideband jammer cancellation with auxiliary multipath, this modification is detrimental since the effective total auxiliary delay is halved, as evident by comparison of Figures A6 and A17.

Additional P_r plots for a narrowband jammer are shown in Figures A18-A19 for equal multipath component strength ($\alpha_m=\alpha_a=1$ and $\alpha_m=\alpha_a=0$ correspondingly). The ripples in Figure A18 can be explained by interference of the direct and multipath sinusoids at the main and auxiliary antennas. In particular for $\tau_0/T = .5 + m$, where m is an integer, the main signal entering the processor is zero, resulting in a null in the P_r response. Similarly for the peaks at $\tau_0/T = .59 + m$ and $\tau_0/T = .61 + m$ are due to auxiliary signal cancellation.

---

* As shown by the results in Appendix B.

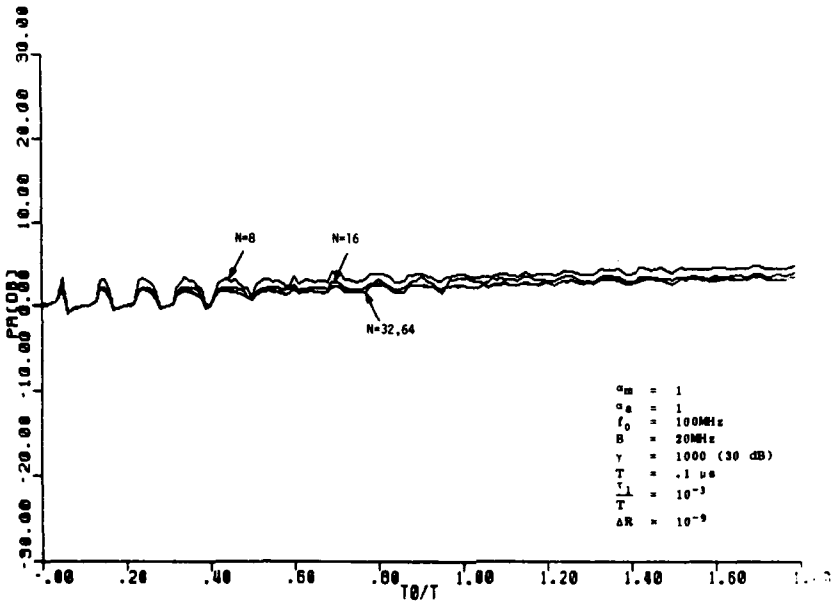

Figure A1. Output Residue Power vs. Normalized Multipath Delay for a Wideband Jammer and α_m=1, α_a=1

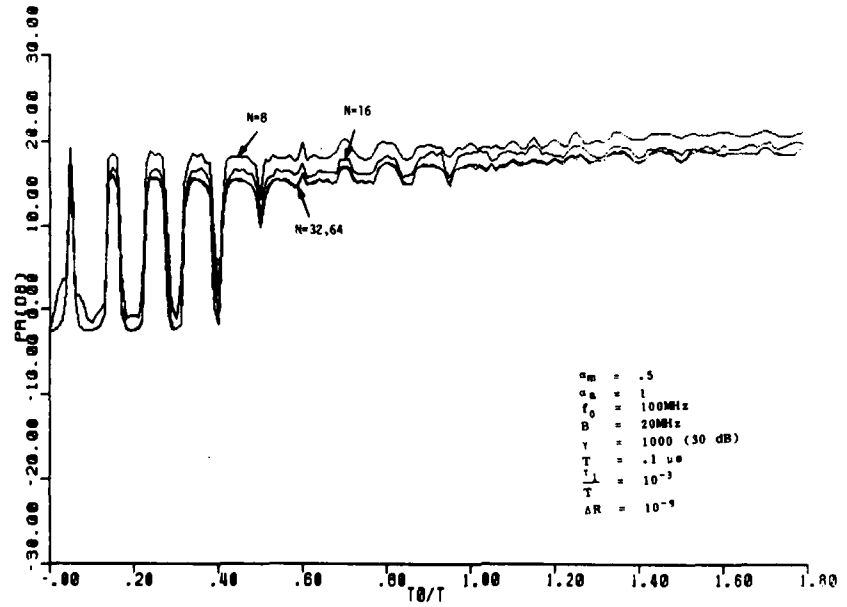

Figure A2. Output Residue Power vs. Normalized Multipath Delay for a Wideband Jammer and α_m=.5, α_a=1

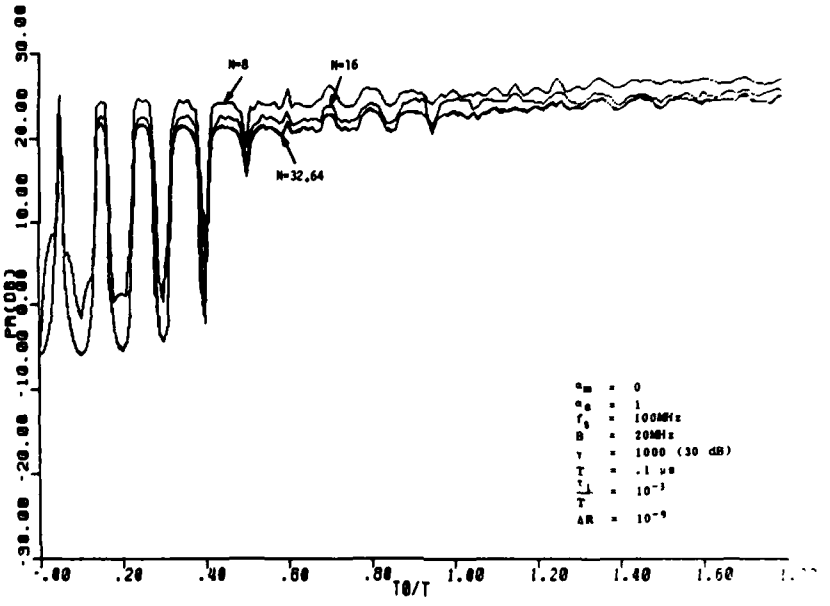

Figure A3. Output Residue Power vs. Normalizd Multipath Delay for a Wideband Jammer and α_m=0, α_a=1

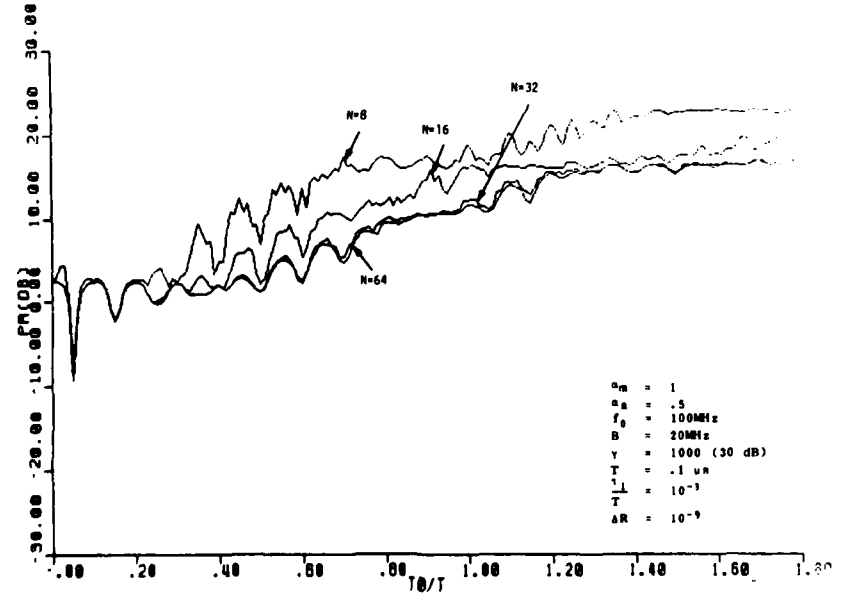

Figure A4. Output Residue Power vs. Normalized Multipath Delay for a Wideband Jammer and α_m=1, α_a=.5

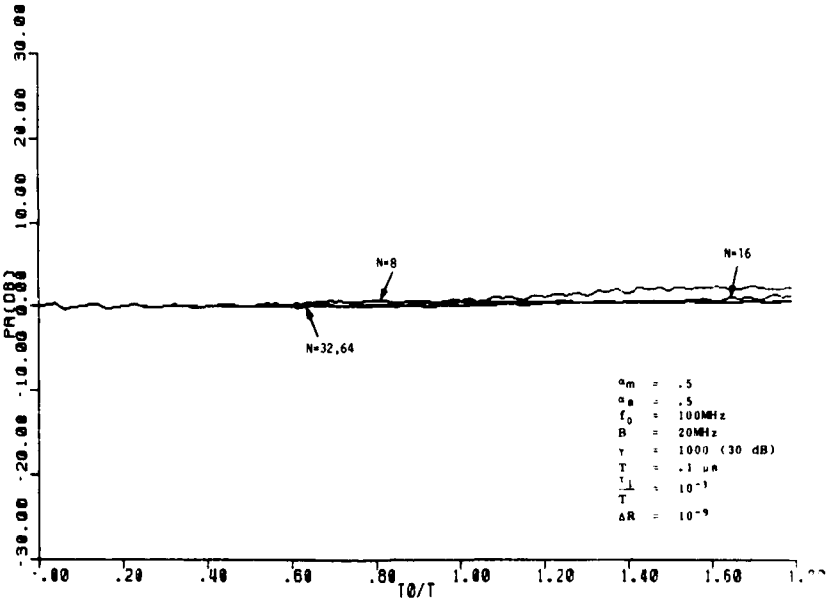

Figure A5. Output Residue Power vs. Normalized Multipath Delay for a Wideband Jammer and α_m=.5, α_a=.5

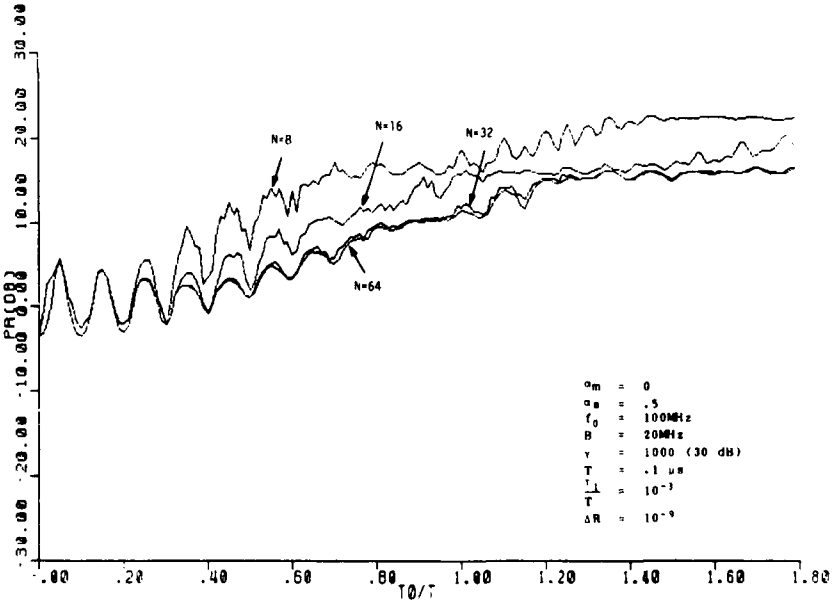

Figure A6. Output Residue Power vs. Normalized Multipath Delay for a Wideband Jammer and α_m=0, α_a=.5

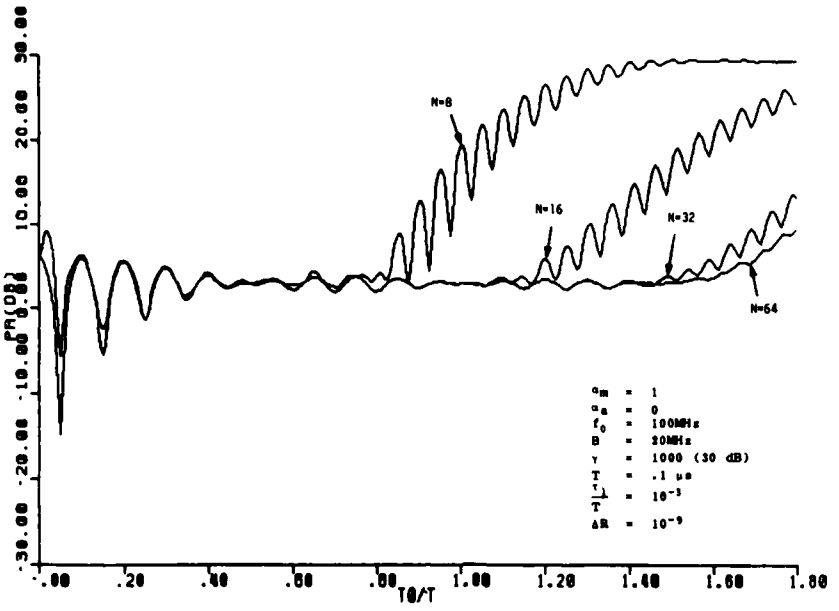

Figure A7. Output Residue Power vs. Normalized Multipath Delay for a Wideband Jammer and α_m=1, α_a=0

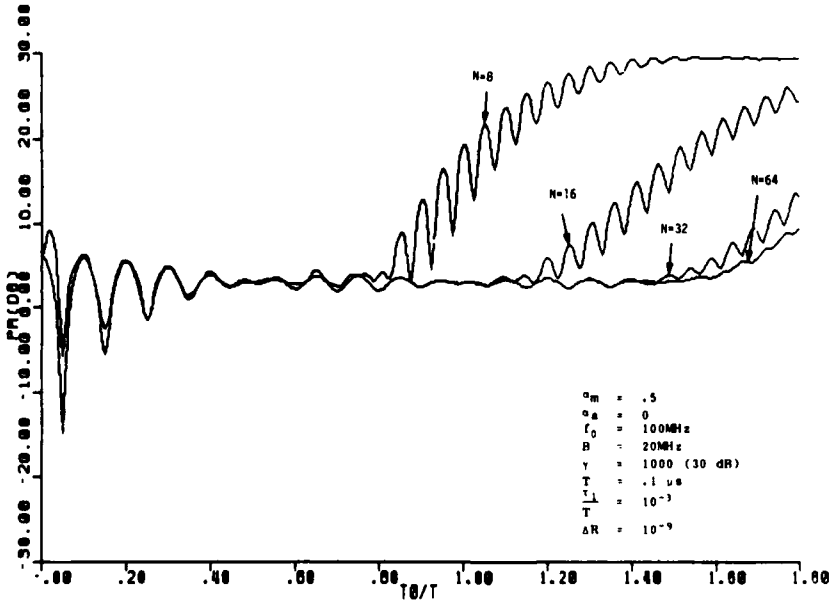

Figure A8. Output Residue Power vs. Normalized Multipath Delay for a Wideband Jammer and α_m=.5, α_a=0

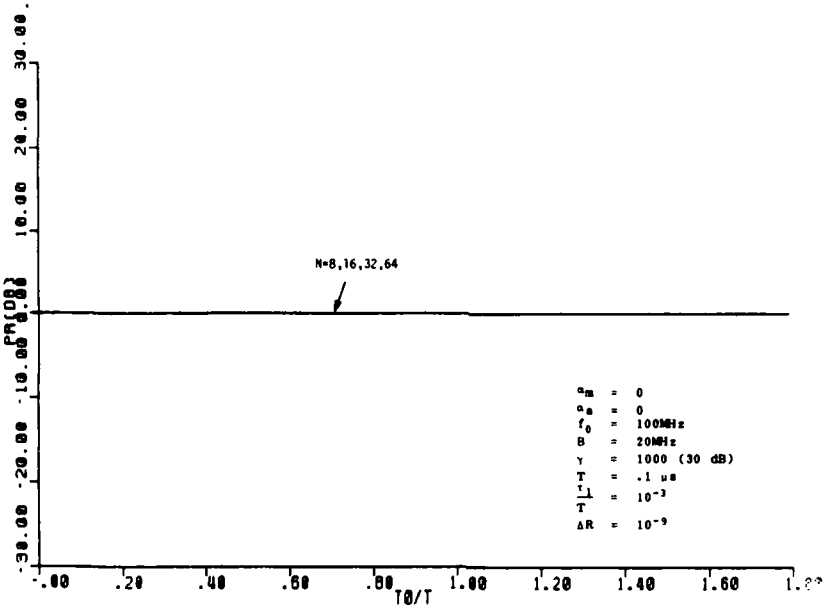

Figure A9. Output Residue Power vs. Normalized Multipath Delay for a Wideband Jammer and α_m=0, α_a=0

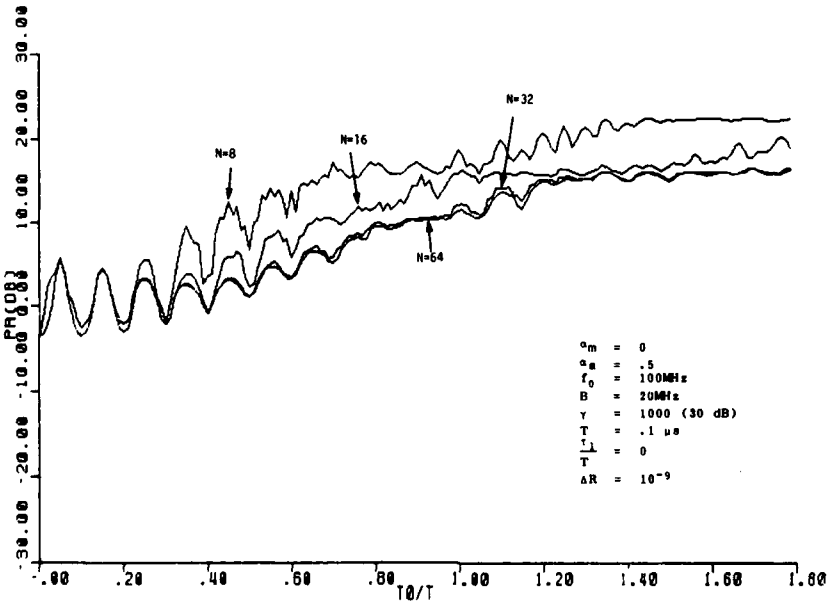

Figure A10. Output Residue Power vs. Normalized Multipath Delay for a Wideband Jammer and τ_1/T=0

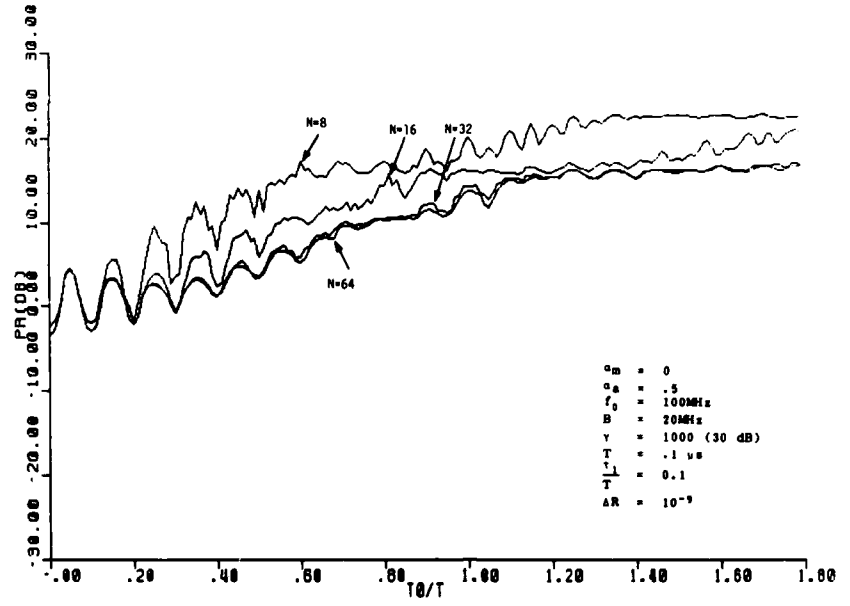

Figure A11. Output Residue Power vs. Normalized Multipath Delay for a Wideband Jammer and $\tau_1/T=.1$

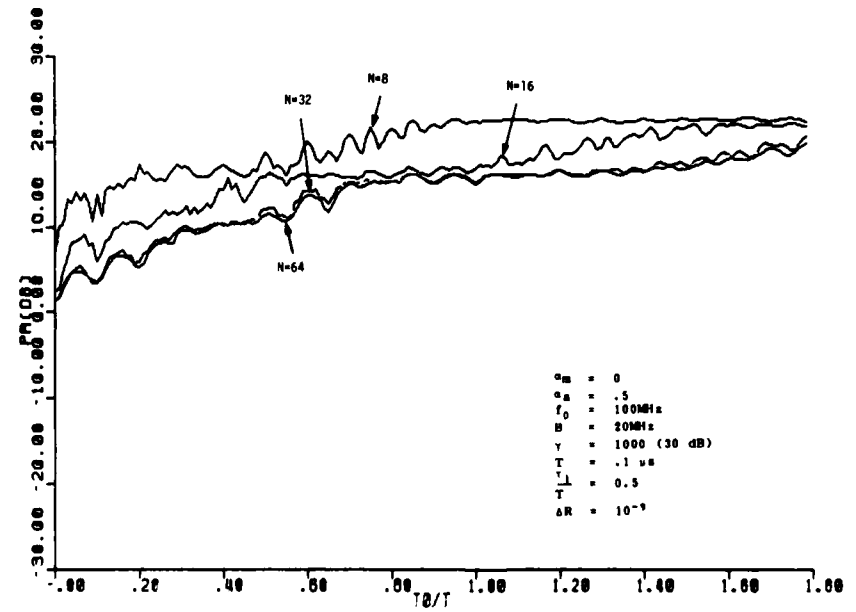

Figure A12. Output Residue Power vs. Normalized Multipath Delay for a Wideband Jammer and $\tau_1/T=.5$

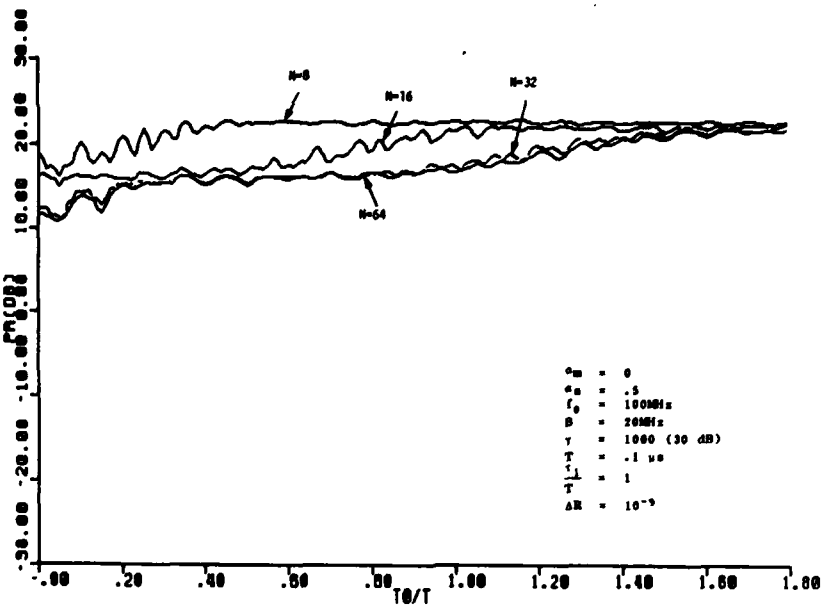

Figure A13. Output Residue Power vs. Normalized Multipath Delay for a Wideband Jammer and $\tau_1/T=1$

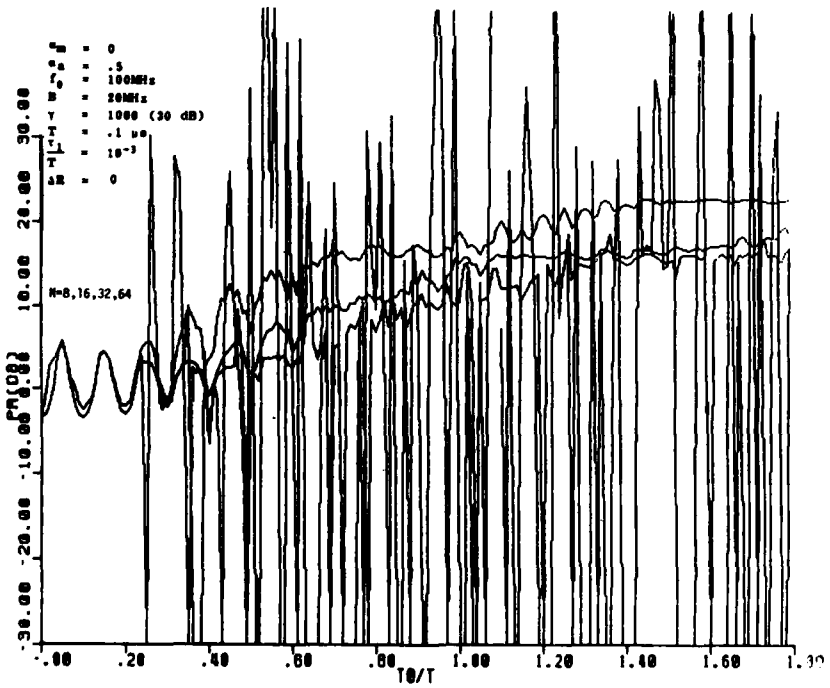

Figure A14. Output Residue Power vs. Normalized Multipath Delay for a Wideband Jammer and ΔR=0

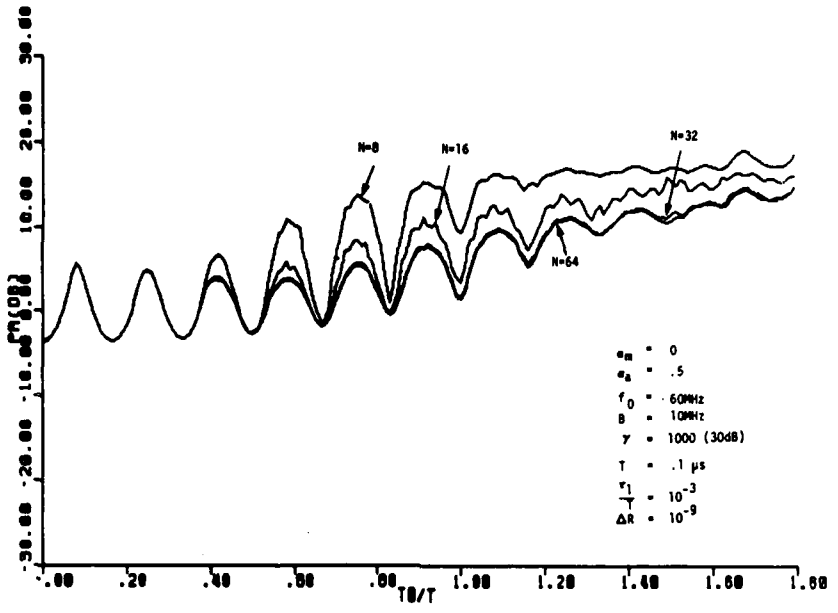

Figure A15. Output Residue Power vs. Normalized Multipath Delay for a Wideband Jammer and T=.1 μsec

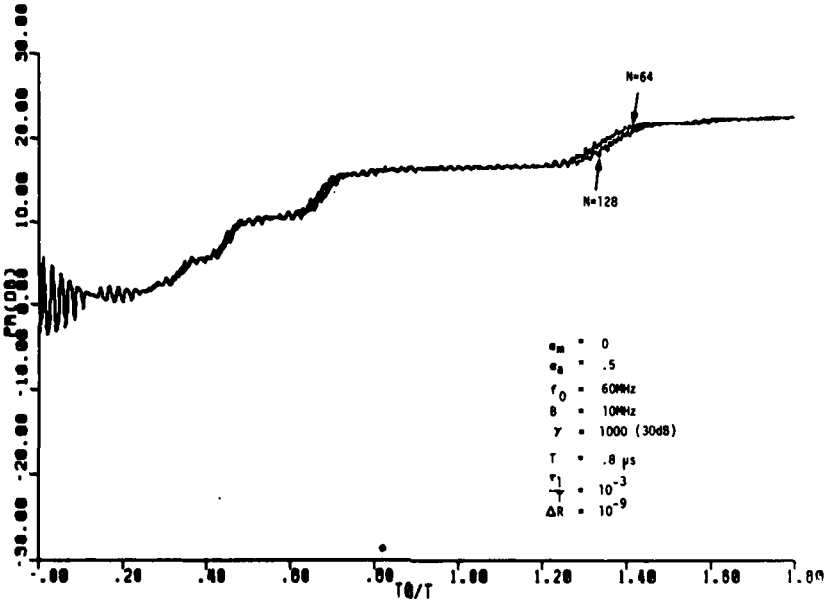

Figure A16. Output Residue Power vs. Normalized Multipath Delay for a Wideband Jammer and T=.8 μsec

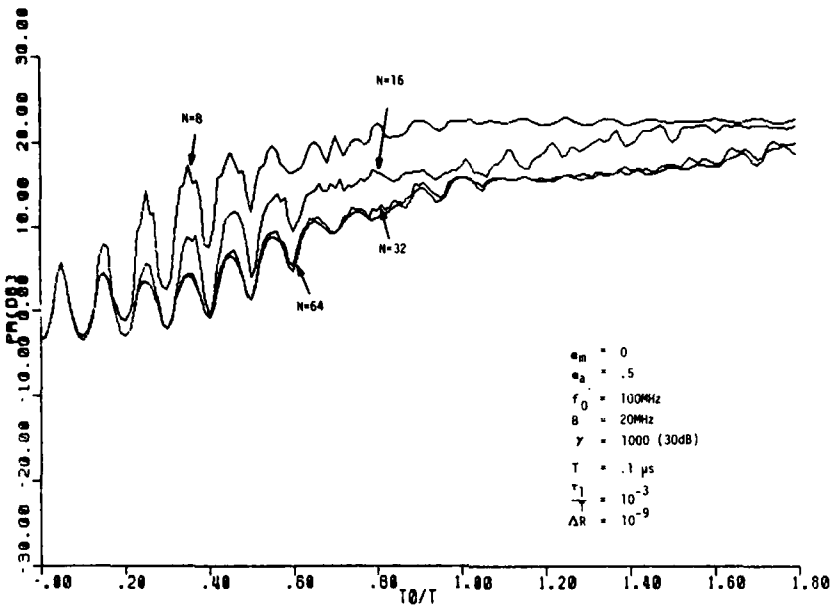

Figure A17. Output Residue Power vs. Normalized Multipath Delay for a Wideband Jammer and a T/2 Delay in the Main Channel

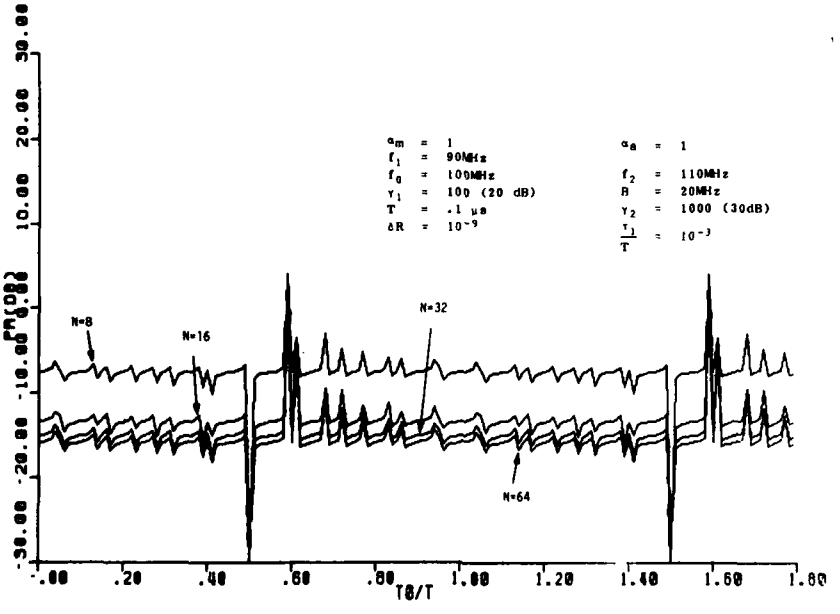

Figure A18. Output Residue Power vs. Normalized Multipath Delay for a Narrowband Jammer and α_m=1, α_a=1

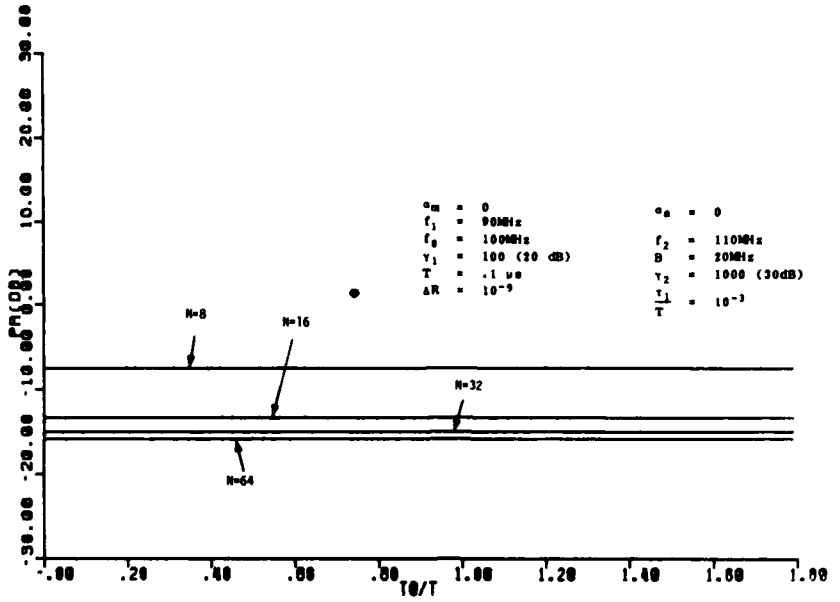

Figure A19. Output Residue Power vs. Normalized Multipath Delay for a Narrowband Jammer and $\alpha_m=0$, $\alpha_a=0$

APPENDIX B

INTERPOLATION AND EXTRAPOLATION OF A BANDLIMITED PROCESS

B.1 GENERAL

Consider a random process x(t) defined on the infinite interval. An estimate of the process x(t) can be obtained as an appropriately weighted sum of N equally-spaced samples of the process covering a total delay T, and is expressed as

$$\hat{x}(t) = \sum_{n=1}^{N} a_n \, x\left(\frac{nT}{N}\right) . \qquad \text{(B-1)}$$

An illustration of this process is shown in Figure B1.

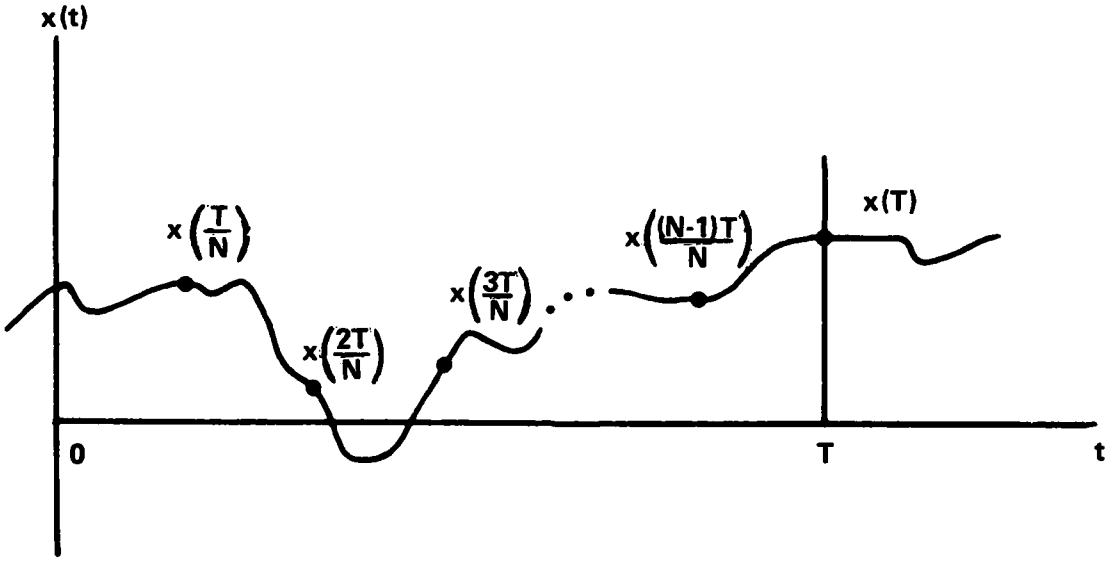

$$\hat{x}(t) = \sum_{n=1}^{N} a_n \, x\left(\frac{nT}{N}\right)$$

Figure B1. A Typical Bandlimited Random Process

The estimation error associated with (B-1) is then given as

$$e(t) = x(t) - \hat{x}(t) = x(t) - \sum_{n=1}^{N} a_n x\left(\frac{nT}{N}\right) . \qquad \text{(B-2)}$$

Minimizing the mean-squared estimation error, $\varepsilon = E\{e^2(t)\}$, is equivalent to applying the orthogonality principle [B-1]:

$$E\left[e(t)x\left(\frac{mT}{N}\right)\right] = R_x\left(t-\frac{mT}{N}\right) - \sum_{n=1}^{N} a_n R_x\left[\frac{(n-m)T}{N}\right] = 0$$

$$m = 1,\ldots,N \qquad \text{(B-3)}$$

where

$$R_x(\tau) \stackrel{\Delta}{=} E[x(t)\, x(t+\tau)] \qquad \text{(B-4)}$$

is the autocorrelation function of the process.

The optimal weight vector $\underline{a}_o$ is obtained by solving (B-3) which in vector form can be written as

$$\underline{R}\, \underline{a}_o = \underline{r} \qquad \text{(B-5)}$$

where $\underline{R}$ is a N×N covariance matrix and r is a N×1 column vector with elements defined in (B-3). Finally, using (B-2), (B-4), and (B-5), the minimum mean-squared estimation error is given simply as

$$\varepsilon_{min} \stackrel{\Delta}{=} \min_{\underline{a}} E\{e^2(t)\} = P_x - \underline{a}^T_o \underline{R}\, \underline{a}_o = P_x - \underline{a}^T_o \underline{r} , \qquad \text{(B-6)}$$

where $P_x = E\{e^2(t)\}$ is the power of the process.

B.2 BANDPASS PROCESS

Now consider the special case of a band-limited random process with a frequency spectrum of bandwidth B centered at f_o. The autocorrelation function of this process is the inverse Fourier transform of the power spectrum, which is then given as

$$R_x(\tau) = \text{sinc}\, B\tau \cos 2\pi f_o \tau$$

$$= \text{sinc}\, \frac{\tau}{T}\, BT \cos\left(2\pi \frac{f_o}{B}\, BT\, \frac{\tau}{T}\right) , \qquad \text{(B-7)}$$

where the sinc function is defined as

$$\text{sinc } x \triangleq \frac{\sin \pi x}{\pi x} ,$$

and for convenience, the process power has been normalized to unity.

Let R_N denote the Nyquist sampling rate which is equal to twice the largest significant frequency in the process power spectrum and let R_S denote the actual sampling rate which is simply given by N/T. The relative sampling rate is then defined as

$$\rho \triangleq \frac{R_S}{R_N} = \frac{N/T}{2f_o+B} = \frac{N}{\left(\frac{2}{B/f_o} + 1\right) BT} . \qquad \text{(B-8)}$$

Calculations of ϵ_{min} as a function of ρ and normalized point of interpolation t/T for a given number of points N and fractional bandwidth B/f_o were obtained by substituting (B-7) into (B-6).

The solution for $\underline{a}_o$ in (B-5) was obtained using the Levinson-Robinson algorithm [32]. Double precision arithmetic was employed to improve accuracy. A small positive term ΔR was added to the diagonal of the covariance matrix $\underline{R}$, whenever deemed necessary, (for large N or small B/f_o), in order to counteract ill-conditioning. The ill-conditioning of the covariance matrix $\underline{R}$ is related to the ratio of largest to smallest eigenvalue or equivalently to the spectral variation of the sampled power spectrum [33] [20].

$$S_x'(f) = \sum_{n=-\infty}^{+\infty} S_x\left(f - \frac{nN}{T}\right) . \qquad \text{(B-9)}$$

For a bandpass spectrum there is no overlap in (B-9) for N>BT, and hence the eigenvalue spread is unbounded and the matrix is inherently ill-conditioned.

B.3 SIMULATION RESULTS

Plots of ε_{min} (dB) versus t/T = 0 for B/f_o = .2* and N = 2,4,8,16 are shown in Figures B2-B5. The nulls in the figures correspond to perfect interpolation whenever the interpolation point coincides with one of the process's sampled points. Note that for a given level of performance, it is necessary to sample much faster for small N than for large N to obtain equivalent performance. Also for large N, good interpolation in the region $0 < t/T < 1$ is possible provided sampling slightly exceeds the Nyquist rate ($\rho > 1$). Note also as would be expected, the extrapolation error monotonically degrades in the region $t/T > 1$, as the correlation between x(t) and the sample values decreases.

The effect of fractional bandwidth B/f_o on ε_{min} is demonstrated in Figures B6-B10 which show plots of ε_{min} versus t/T for N=8 and B/f_o=.01,.1,.5,1,2. Note the performance degradation with increasing B/f_o and the capability of good extrapolation in the region t/T>1 for B/f_o=.01. The increase in ε_{min} with increasing B/f_o for a given ρ and N can be explained from (B-7) and (B-8): as B/f_o increases, BT also increases in (B-8) for the same value of ρ, such that the nulls of the sinc function in (B-7) which occur at multiples of 1/BT are pushed closer to the origin, resulting in sampling smaller values of the autocorrelation function and therefore performance degrades.

The previous results show the level of the minimum mean squared estimation error as a function of N, R_S/R_N and B/f_o and how the performance degrades with decreasing N, R_S/R_N and increasing B/f_o. The results relate to the performance capabilities of the multiple CCL processor in the main body of this report when the same wideband jammer signal is received in both main and auxiliary channels.

---

* This ratio corresponds to the nominal values B=20 MHz, f_o = 100 MHz parameters used in the main body of this report.

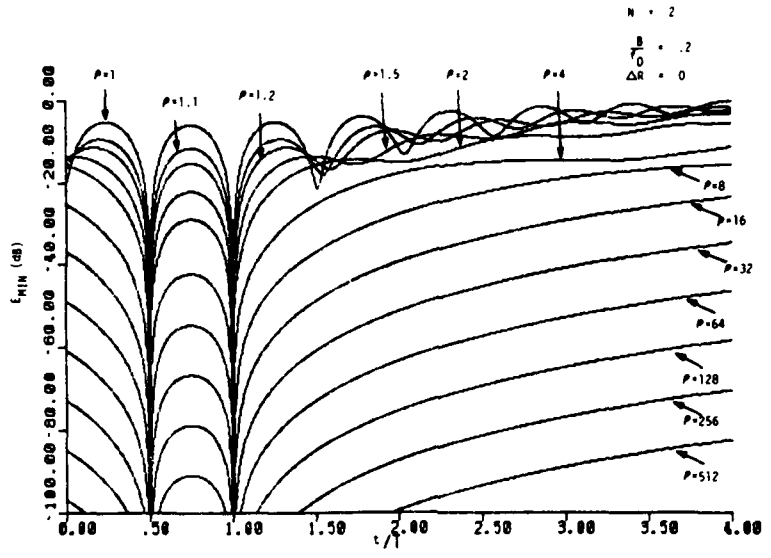

Figure B2. Minimum Mean-Squared Estimation Error vs. Normalized Estimation Point and N=2

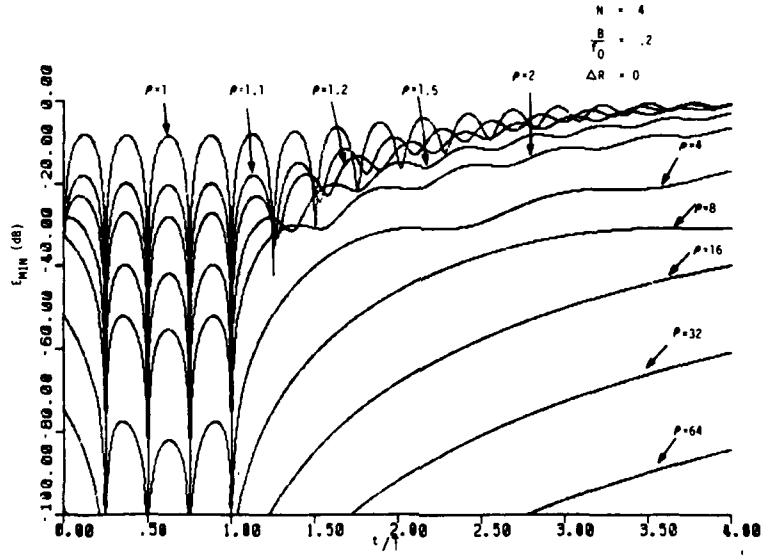

Figure B3. Minimum Mean-Squared Estimation Error vs. Normalized Estimation Point and N=4

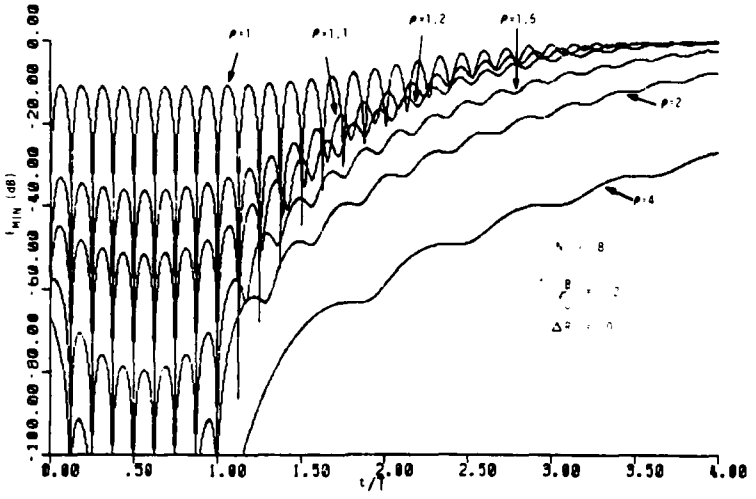

Figure B4. Minimum Mean-Squared Estimation Error vs. Normalized Estimation Point and N=8

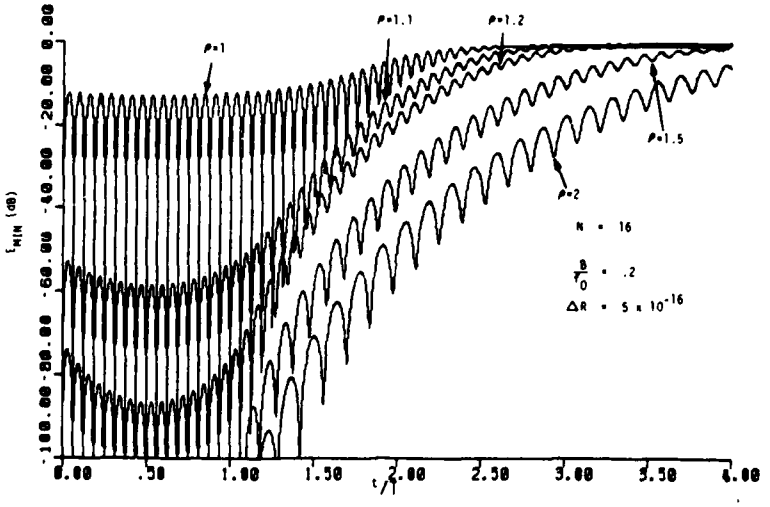

Figure B5. Minimum Mean-Squared Estimation Error vs. Normalized Estimation Point and N=16

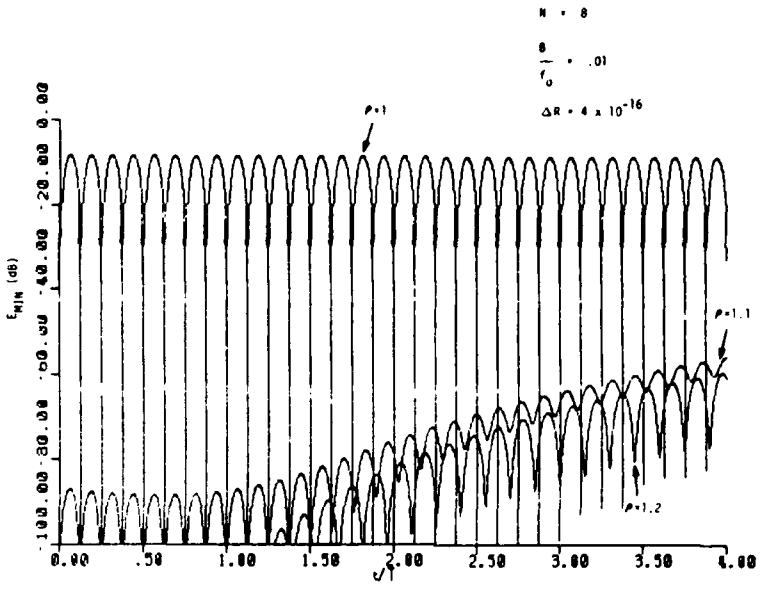

Figure B6. Minimum Mean-Squared Estimation Error vs. Normalized Estimation Point and B/f_O=.01

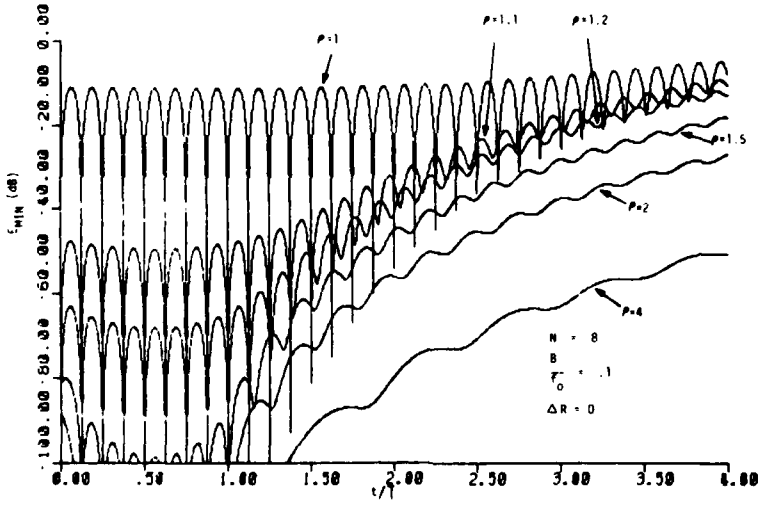

Figure B7. Minimum Mean-Squared Estimation Error vs. Normalized Estimation Point and B/f_O=.1

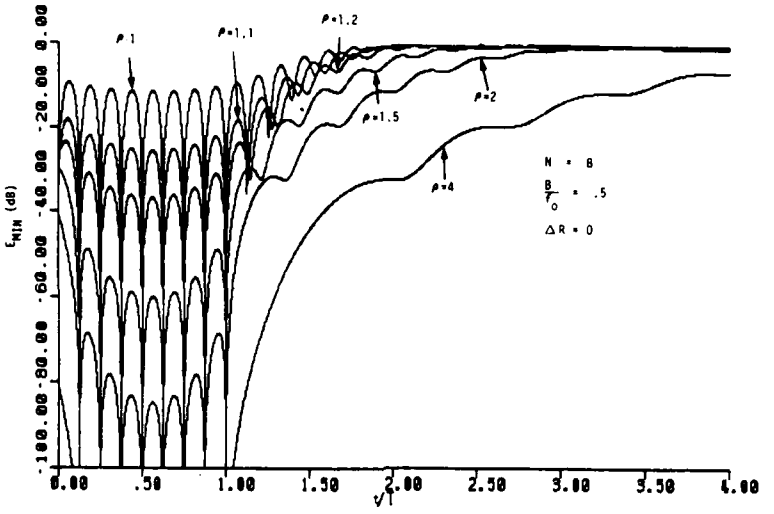

Figure B8. Minimum Mean-Squared Estimation Error vs. Normalized Estimation Point and B/f_o=.5

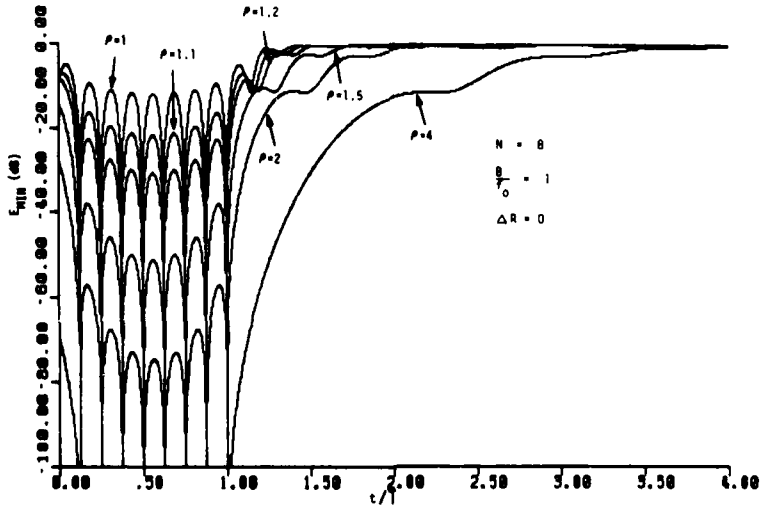

Figure B9. Minimum Mean-Squared Estimation Error vs. Normalized Estimation Point and B/f_o=1

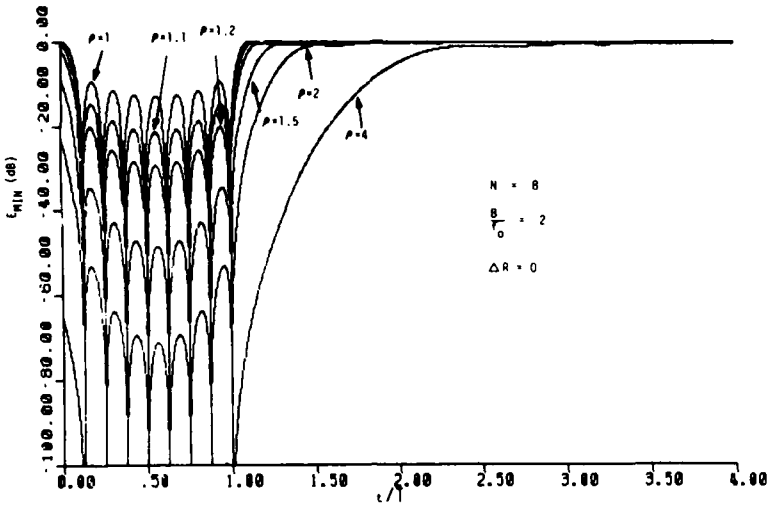

Figure B10. Minimum Mean-Squared Estimation Error vs. Normalized Estimation Point and $B/f_o=2$

APPENDIX C

SIMULATION RESULTS FOR QUADRATURE TAP SPACING

In this appendix, the multipath cancellation performance of the adaptive array processor considered in the main part of this report is investigated for quadrature tap spacing as opposed to uniform tap spacing.

The steady state value of the processor adaptive weight vector $\underline{w}_\infty$ is obtained as a solution to

$$\underline{R}\,\underline{w}_\infty = \underline{r}\ , \tag{C-1}$$

where $\underline{R}$ is the N×N auxiliary signal covariance matrix and $\underline{r}$ is a N×1 column vector. For a uniform tap spacing iT/N, i=0,...,N-1, where T is the delay line length and N is the number of adaptive taps, the matrix $\underline{R}$ is Toeplitz and can be solved using the Levinson-Robinson algorithm as was used in the main body of this report. For uniform tap spacing, $\underline{R}$ and $\underline{r}$ are given as

$$\underline{R} : \{r_{ij} = R_a[(i-j)\frac{T}{N}]\} \quad i,j=0,\ldots,N-1 \tag{C-2}$$

$$\underline{r} : \{r = R_{ma}(-j\frac{T}{N})\} \quad j = 0,\ldots,N-1 \tag{C-3}$$

where R_a is the auxiliary signal autocorrelation and R_{ma} is the cross-correlation between the main and auxiliary signal.

The processor output power P_r can be easily obtained as

$$P_r = 1 - \underline{w}_\infty{}^T\underline{R}\,\underline{w}_\infty = 1 - \underline{w}_\infty{}^T\underline{r}\ . \tag{C-4}$$

Plots of P_r (dB) versus τ_o/T for the nominal parameters, α_m=0, α_a=.5, B=20 MHz and T=.1 μsec were generated.

From sampling theory it is known that in general, optimum performance will be obtained provided the effective tap spacing is closer than required by the Nyquist sampling rate, that is,

$$\frac{T}{N} < \frac{1}{2\,f_o + B}\ . \tag{C-5}$$

Also from sampling theory, when the taps are located on the delay line in quadrature pairs, optimum performance is obtained provided the effective tap spacing is less than one over the bandwidth, that is

$$\frac{T}{N} < \frac{1}{B} \quad . \tag{C-6}$$

A plot of P_r (dB) versus τ_o/T for N=4,8,16,32,64 and for the nominal system frequency f_o=100 MHz is shown in Figure C1. The nominal phase of the auxiliary tapped delay line signals is given by

$$\phi_i = 2\pi f_o \frac{iT}{N} \qquad i = 0,1,\ldots, N-1. \tag{C-7}$$

For N=8, it can be seen that successive taps are spaced apart 90° in phase, and thus the samples occur in quadrature pairs and (C-6) is satisfied. Therefore near-optimum performance in the output residue response is obtained for N>8. On the other hand, for N=4 the taps are not in quadrature pairs. Therefore (C-6) is not satisfied, and a degradation in the P_r response is noted.

A plot of P_r versus τ_o/T with f_o increased by a factor of four to f_o = 400 MHz is shown in Figure C2. For N=8, N=16 a performance degradation is observed which is the result of sampling at less than the Nyquist rate (C-5). For N=32,64 though the quadrature spacing of taps results in a near-optimum performance since (C-6) is satisfied.

A plot of P_r (dB) versus τ_o/T for a system frequency five times larger than the original or f_o=500 MHz is shown in Figure C3. For N=8 it can be seen from (C-7) that the taps are spaced apart 90° in phase, that is they occur in quadrature pairs and (C-6) applies. Therefore near-optimum performance is obtained for N>8. Comparison of Figures C2 and C3 shows the dramatic performance improvement possible with quadrature sampling in Figure C3 even though the corresponding system frequency is larger than the one in Figure C2 (500 versus 400 MHz). The previous discussion explains the choice of number of taps (N=8,16,32,64) in the simulation runs of the main body of this report.

Another way to ensure quadrature tap spacing is by sampling the auxiliary signal in pairs spaced $1/4f_o$ apart. In this case, since nonuniform tap spacing is employed, the covariance matrix $\underline{\underline{R}}$ is not Toeplitz and a solution for the steady-state weight $\underline{w}_\infty$ in (C-1) must be obtained by matrix inversion.

A plot of P_r (dB) versus τ_o/T for N=4,8 quadrature taps with single precision arithmetic is shown in Figure C4. Near-optimum performance is obtained for N=8 as predicted since (C-6) is satisfied. The degradation for N=4 can be explained perhaps because the number of samples N is not large enough.

A plot of P_r (dB) versus τ_o/T for N=4 and N=8 for uniform tap spacing was generated using again matrix inversion and single precision arithmetic and is shown for comparison in Figure C5. Note again that near-optimum performance for N=8 is obtained due to quadrature sampling and that performance is degraded for N=4.

The advantage of quadrature sampling as opposed to uniform sampling has been demonstrated. For a real signal processor it requires an inflexible system with exact alignment of the taps according to system frequency to insure that consecutive tap phase differences are 90° apart. A general processor on the other hand is more flexible and will have good performance provided (C-5) is satisfied, that is N is large enough.

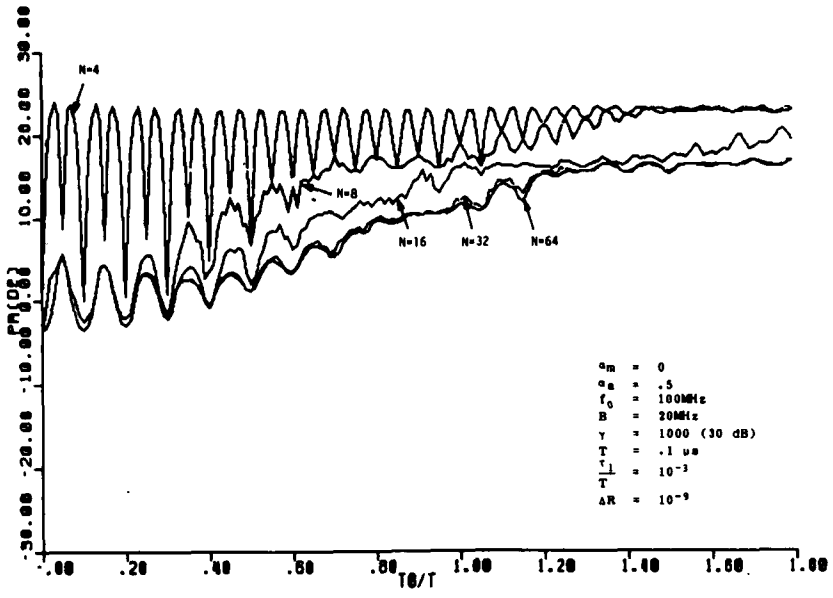

Figure C1. Output Residue Power vs. Normalized Multipath Delay for a Wideband Processor and f_o=100MHz

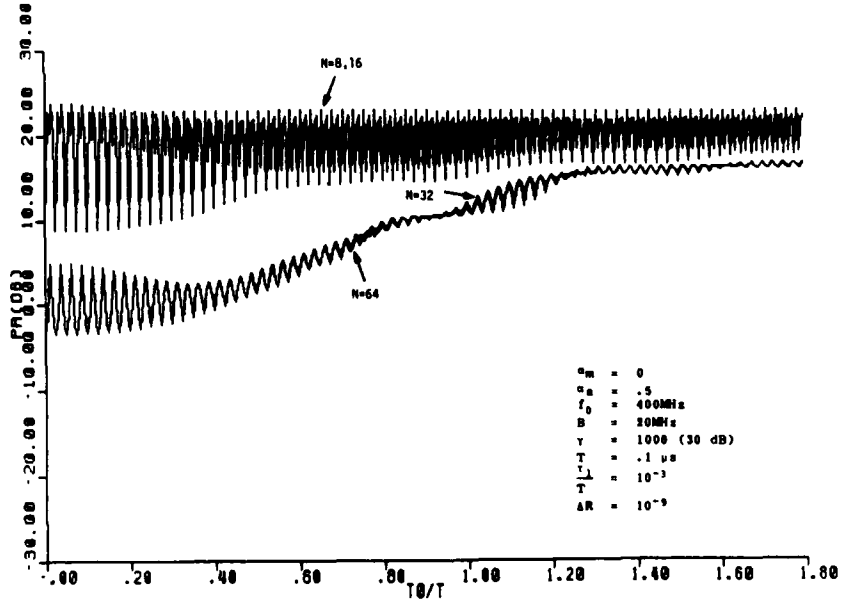

Figure C2. Output Residue Power vs. Normalized Multipath Delay for a Wideband Processor and f_o=400MHz

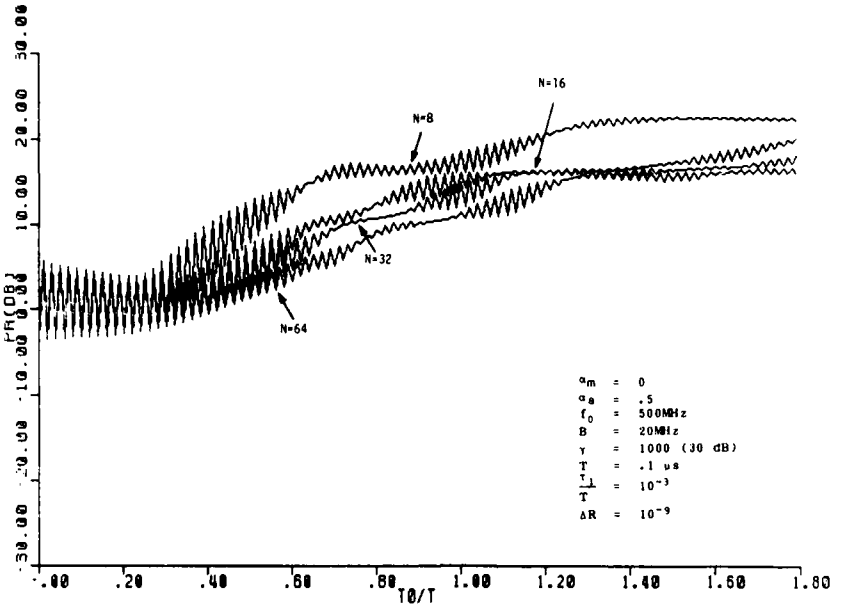

Figure C3. Output Residue Power vs. Normalized Multipath Delay for a Wideband Processor and f_o=500MHz

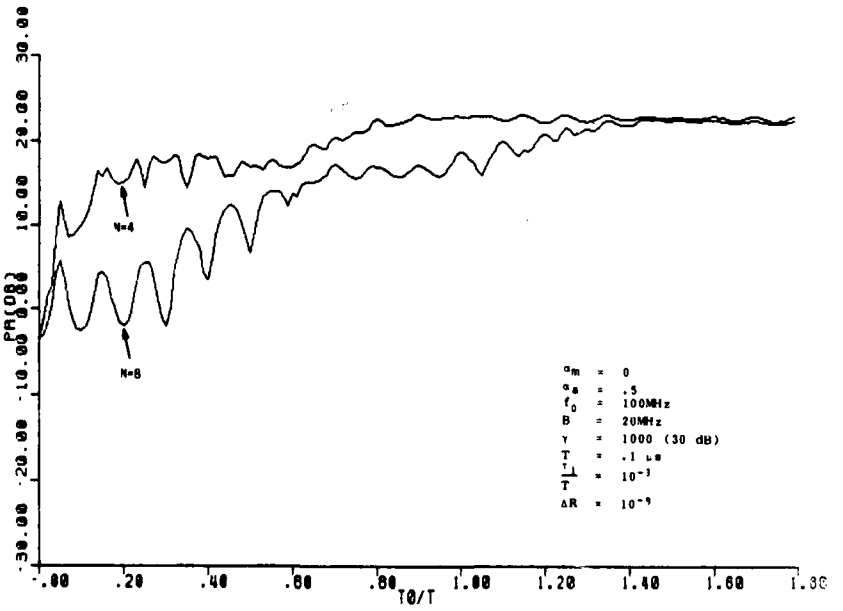

Figure C4. Output Residue Power vs. Normalized Multipath Delay for a Wideband Processor and Quadrature Tap Spacing

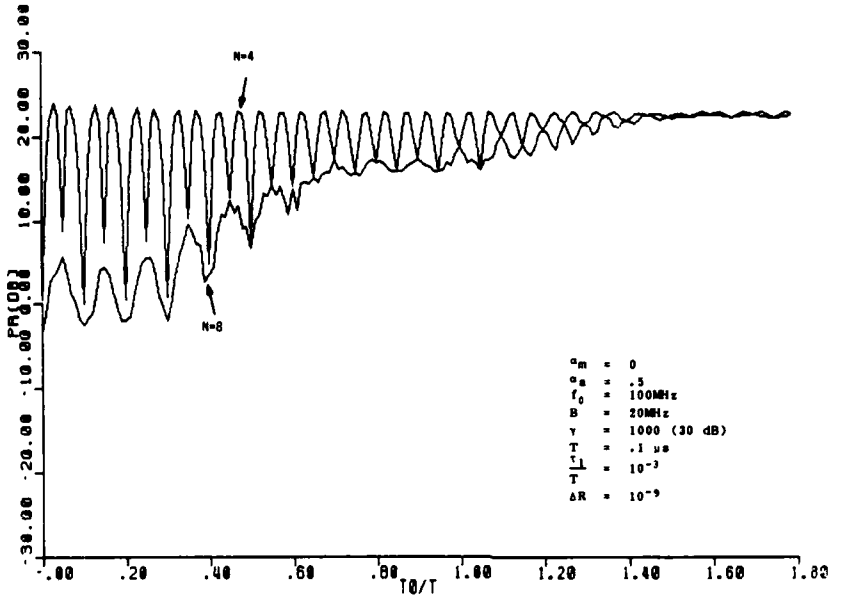

Figure C5. Output Residue Power vs. Normalized Multipath Delay for a Wideband Processor and Uniform Tap Spacing

APPENDIX D

PLOTS OF JAMMER AND NOISE AUTOCORRELATION FUNCTIONS

Consider a bandlimited random process x(t) with a frequency spectrum of bandwidth B and center frequency f_o. The process autocorrelation function $R_x(\tau)$ is given as

$$R_x(\tau) = \text{sinc } B\tau \cos 2\pi f_o \tau \ , \qquad \text{(D-1)}$$

where sinc x is defined as

$$\text{sinc } x = \frac{\sin \pi x}{\pi x} \ .$$

Plots of $R_x(\tau)$ versus τ for the fractional bandwidth, B/f_o=.01,.1,.2,.5,1,2 are shown in Figures D1-D6.

Let y(t) represent a narrowband random process consisting of two sinusoids of frequencies f_1 and f_2 and corresponding powers γ_1 and γ_2. The process autocorrelation function $R_y(\tau)$ is given as

$$R_y(\tau) = \gamma_1 \cos 2\pi f_1 \tau + \gamma_2 \cos 2\pi f_2 \tau \ . \qquad \text{(D-2)}$$

A plot of the normalized autocorrelation function $R_y(\tau)/(\gamma_1+\gamma_2)$ for the nominal parameter values f_1=90 MHz, f_2=110 MHz, γ_1=100 (20 dB) and γ_2=1000 (30 dB) is shown in Figure D7.

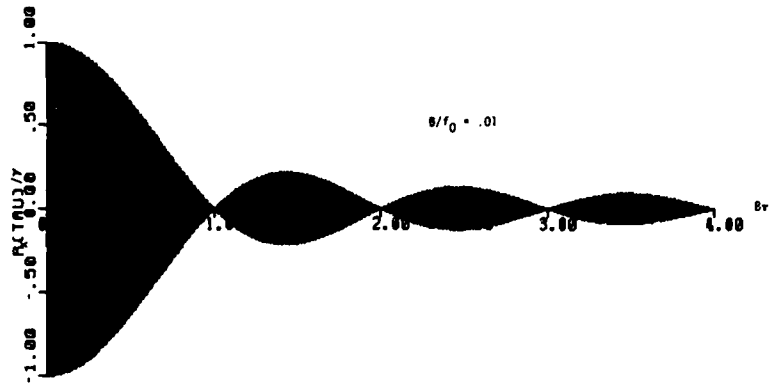

Figure D1. Autocorrelation Function of a Wideband Process and $B/f_o=.01$

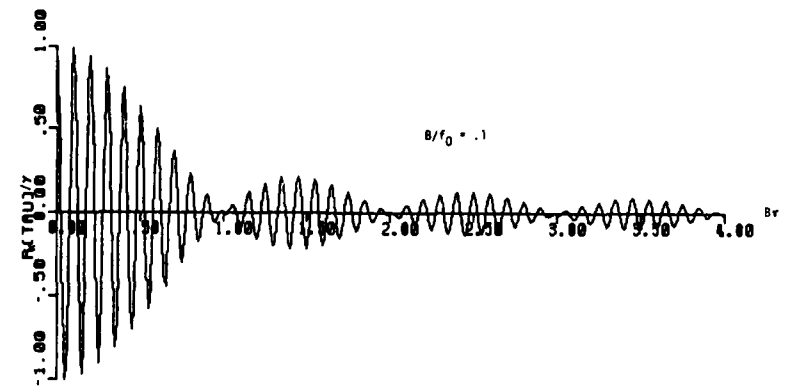

Figure D2. Autocorrelation Function of a Wideband Process and $B/f_o=.1$

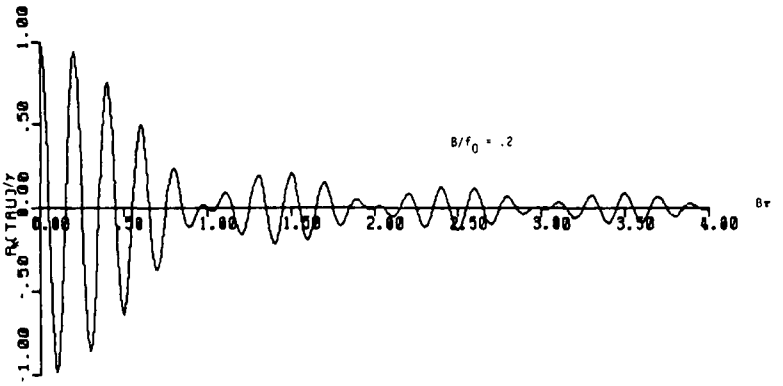

Figure D3. Autocorrelation Function of a Wideband Process and B/f_o=.2

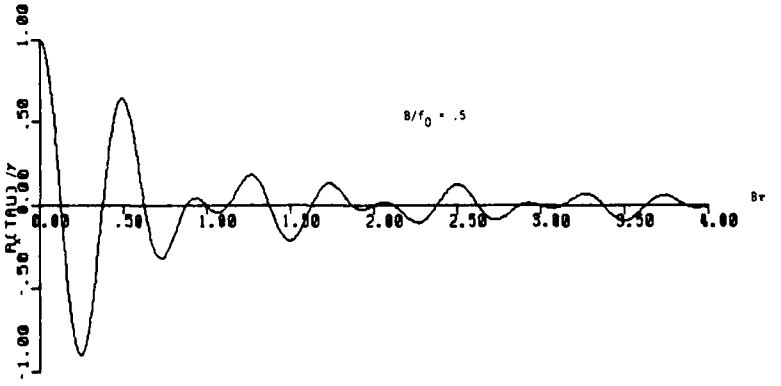

Figure D4. Autocorrelation Function of a Wideband Process and B/f_o=.5

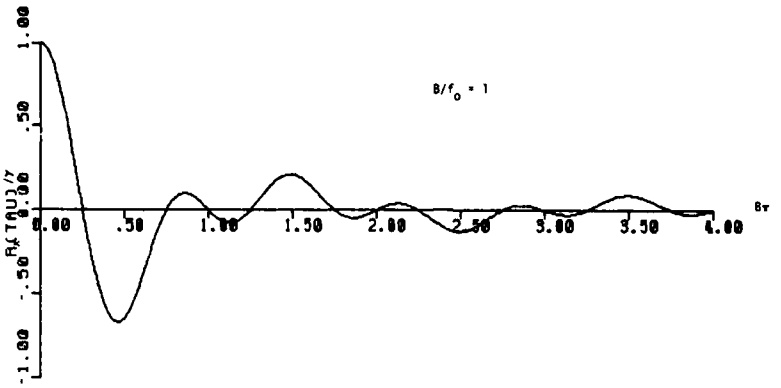

Figure D5. Autocorrelation Function of a Wideband Process and $B/f_o=1$

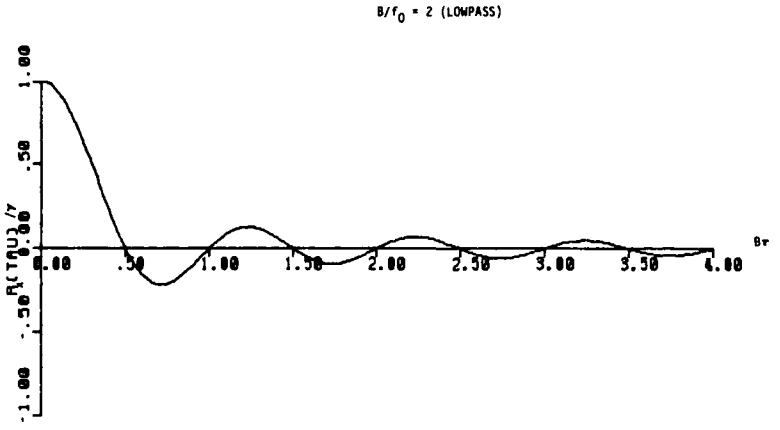

Figure D6. Autocorrelation Function of a Wideband Process and $B/f_o=2$

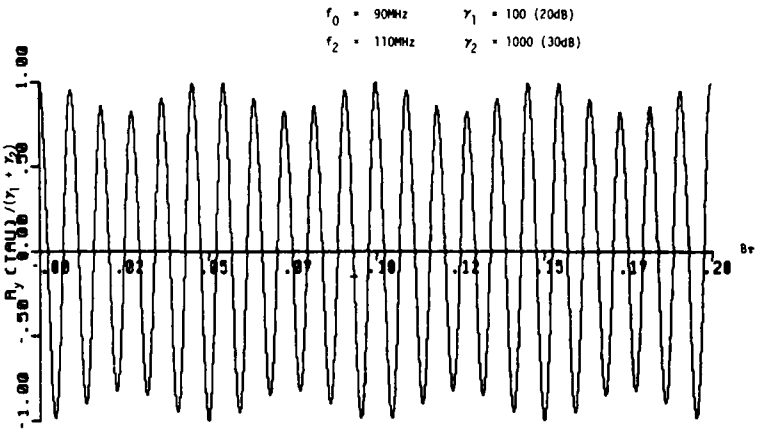

Figure D7. Autocorrelation Function of a Narrowband Process

APPENDIX E

COMPUTER PROGRAM LISTINGS

E.1 WIDEBAND JAMMER

This appendix describes the computer programs that were employed in the main body of this report for solving the adaptive array processor interference cancellation problem in a single multipath environment. For the wideband jammer, output residue data versus normalized multipath delay was generated by the program-file WIDBJAM a listing of which is shown in Figure E1.

The program employs double-precision arithmetic for variable definitions and calculations in order to obtain sufficient accuracy. It starts by reading in from file 24 the parameter values for the delay length T, the system frequency F and bandwidth BW, the jammer signal to noise power ratio G and the multipath component strengths AM and AA. Since the auxiliary channel covariance matrix is Toeplitz, a one-dimensional array R(N) is used to store its elements. The cross correlations of the main with the delayed auxiliary signals are stored in array B(N). Loop 2 calculates the elements in R(J), B(J), J=1,...,N by calling functions RA and RMA. Functions RA, RM, RN and RMA calculate for a given delay TAU the corresponding auxiliary, main and noise signal autocorrelations and the crosscorrelation between the main and auxiliary signals.

A small positive number RD=10^{-9} is added to R(1) to counteract the ill-conditioning of the auxiliary covariance matrix. A solution for the adaptive weights W(N) is obtained from subroutine SOLVE, which is a modified version of a subroutine listed in Appendix A of [34], based on Levinson's method.

Subroutine BERROR calculates the average and maximum errors in the estimates of B(N) due to the finite accuracy in the calculation of W(J), J=1,...N and the ill-conditioning of the covariance matrix.

The output residue PT is calculated in decibels by loop 4 and the five ensuing statements. If the output residue is less than or equal to zero, due to finite computer accuracy or ill-conditioning, its decibel value is set by statement 6 to -30.

Finally the program writes the output residue values PT and the corresponding normalized multipath delays TR1 = TO/T = 0,.01,.02,...,1.80 to file 101.

E.2 NARROWBAND JAMMER

The computer program-file NARBJAM generates output residue versus normalized multipath delay data for the narrowband jammer adaptive cancellation problem. The program is a variation of the wideband jammer program WIDBJAM. It reads from file 3 the delay length T, the frequencies of the two sinusoids F(1) and F(2), the system bandwidth BW, the sinusoid signal to noise power ratios G(1) and G(2) and the multipath parameters AM and AA. The program has the additional function RS which calculates the autocorrelation of the jammer. Its main difference to WIDBJAM is that it uses complex double precision arithmetic to calculate the output residues due to the sinusoids in loop 7. Finally the program writes to file 102 the normalized delay values TR1=0,.01,.02,...,1.8 the total output residue PT and the individual power residues PR(K),K=1,...,3.

E.3 INTERPOLATION AND EXTRAPOLATION OF A BANDLIMITED PROCESS

The program-file INTERPOL in Figure E3 generates output data for the minimum mean-squared estimation error (in decibels) EMIN of a bandlimited process as a function of normalized estimation point TT. The program is very similar to WIDBJAM and NARBJAM. For a given number of taps N, functional bandwidth BF and relative sampling to Nyquist rate RT(J), 1=1,...,13, it generates output data of TT=0,.0025,...,4 and EMIN. Its function RX calculates the autocorrelation of the bandlimited process and is essentially the same as function RN of programs WIDBJAM and NARBJAM.

E.4 PLOT ROUTINES

A plot of the output residue PT versus normalized multipath delay TR1=0,.01,...,1.8 was generated by the program-file PLTDAT. The program reads the number of taps N and the corresponding TR1, PT values from file IF and stores them in array, X(180), Y(180). For each N it calls subroutine LINE to plot the points X(J), Y(J), J=1,...,180. The X and Y axes are plotted by calling subroutine AXIS twice.

The program PLTDAT was also used to generate plots for the narrowband jammer after simply changing the format of the READ and WRITE statements in it. For the interpolation plots in addition to changing the READ and WRITE statements, the dimension of X and Y was increased to 1600 and IN changed to 1600 since a total of 1600 points were read and plotted. A PLXY plotter was used to generate all the plots.

```
C
C       FILE: WIDBJAM
C
C       1.  THE JAMMER CONSISTS OF A WIDEBAND SIGNAL (30 DB)
C       2.  ALL VARIABLES AND CONSTANTS ARE IN DOUBLE PRECISION
C       3.  A TYPICAL ANGLE IS EVALUATED AS:
C           OMEGA = MOD(2.D0*F(I)*TAU,2.D0)*PI
C       4.  AA AND AM ARE THE MULTIPATH GAINS FOR THE AUXILIARY AND MAIN
C           CHANNELS CORRESPONDINGLY.
C
        DOUBLE PRECISION R(260),B(260),W(260),Y1,Y2,YT
        DOUBLE PRECISION PT,XN,PI,T,T0,T1,TR,TR1,XX,YY
        DOUBLE PRECISION BHAT(260),BW,F,G,Y,P,RMA,RA,RM,AA,AM,RD
        COMMON AA,AM,T0,T1,G
        COMMON /B1/F,BW,PI
        PI=3.14159265358979320+0
        RD=1.D-9
        IF=101
        READ (24,*) T,F,BW,G,AM,AA
C
C       THE FOLLOWING NORMALIZATIONS ARE ASSUMED IN THE DEFINITIONS
C       OF THE PROGRAM VARIABLES:
C       F=F*1.E-6                BW=BW*1.E-6
C       T0=T0*1.E+6              T1=T1*1.E+6              T=T*1.E+6
C
        T1=1.0D-4
        TR=T1/T
        WRITE (IF,100) F,BW,G,AM,AA,T,TR,DD
  100 FORMAT (/,5X,'F0 =',F7.2,23X,'NOISE BANDWIDTH =',F5.1,10X,'(MEG
     ,AHERTZ)',/,5X,'GAMMA =',F7.1,20X,'ALPHA OF MAIN = ',F8.6,10X,
     ,'ALPHA OF AUXILIARY = ',F8.6,/,5X,'TAP
     ,DELAY LENGTH =',F5.3,11X,'T1/T =',F7.4,19X,'(MICROSECONDS)',/,
     ,5X,'WHITE NOISE ADDED TO RA(1) =',D10.2)
        N=8
        DO 1 M=1,4
        YT=0.D0
        T0=-.01D0*T
        WRITE (IF,200) N
  200 FORMAT (//,5X,'# OF DELAY TAPS =',I3)
        XN=DBLE(N)
        DO 3 L=1,180
        T0=T0+.01D0*T
        TR1=T0/T
```

Figure E1. Wideband Jammer (WIDBJAM) Program Listing
(Sheet 1 of 4 Sheets)

```
      DO 2 J=1,N
      Y1=DBLE(J-1)*T/XN
      Y2=DBLE(-J+1)*T/XN
      R(J)=RA(Y1)
    2 B(J)=RA(Y2)
      R(1)=R(1)+RD
      CALL SOLVE (R,W,B,N)
      R(1)=R(1)-RD
      CALL ERROR (R,W,B,BHAT,XX,YY,N)
      YT=YT+YY
      P=0.D0
      Y=0.D0
      DO 4 K=1,N
      DO 5 J=1,N
      JJ=IABS(K-J)+1
    5 P=P+W(K)*W(J)*R(JJ)
    4 Y=Y+W(K)*B(K)
      PT=RM(0.D0)+P-2.D0*Y
      IF (PT.LE.0.D0) GO TO 6
      PT=10.D0*DLOG10(PT)
      GO TO 3
    6 PT=-30.D0
    3 WRITE (IF,300) TR1,PT,XX,YY
  300 FORMAT (1X,'T0/T = ',F4.2,10X,'PR = ',F10.10,10X,
     ,'MAX. NORM. B ERROR =',D14.7,5X,'AVE. NORM. B ERROR =',D14.7)
      YT=YT/180.D0
      WRITE (IF,400) YT
  400 FORMAT (10X,'AVERAGE NORMALIZED B ERROR = ',D14.7)
    1 N=N*2
      STOP
      END
C
      FUNCTION RA (TAU)
      COMMON AA,AM,T0,T1,G
      DOUBLE PRECISION AA,AM,TAU,G,T0,T1,S1,S2,S3,S4,RA,RN
      S1=RN (TAU,G)
      S2=RN (TAU-T0-T1,G)
      S3=RN (TAU+T0+T1,G)
      S4=RN (TAU,1.0D0)
      RA=(1.D0+AA**2)*S1+AA*(S2+S3)+S4
      RETURN
      END
```

Figure E1. Wideband Jammer (WIDBJAM) Program Listing
(Sheet 2 of 4 Sheets)

```
C
      FUNCTION RM (TAU)
      COMMON AA,AM,T0,T1,G
      DOUBLE PRECISION AA,AM,TAU,G,T0,T1,S1,S2,S3,RM,RN
      S1=RN (TAU,G)
      S2=RN (TAU-T0,G)
      S3=RN (TAU+T0,G)
      RM=(1.D0+AM**2)*S1+AM*(S2+S3)
      RETURN
      END
C
      FUNCTION RMA(TAU)
      DOUBLE PRECISION AA,AM,G,TAU,T0,T1,S1,S2,S3,S4,RMA,RN
      COMMON AA,AM,T0,T1,G
      S1=RN (TAU,G)
      S2=RN (TAU-T0-T1,G)
      S3=RN (TAU+T0,G)
      S4=RN (TAU-T1,G)
      RMA=S1+AA*S2+AM*S3+AA*AM*S4
      RETURN
      END
C
      FUNCTION RN (TAU,G1)
      DOUBLE PRECISION F,G1,BW,TAU,X1,X2,X3,RN,PI
      COMMON /B1/F,BW,PI
      RN=G1
      IF (TAU.EQ.0.0D0) RETURN
      X1=BW*TAU
      X2=2.0D0*F*TAU
      X3=DMOD(X1,2.0D0)*PI
      X1=X1*PI
      X2=DMOD(X2,2.0D0)*PI
      RN=G1*DSIN(X3)*DCOS(X2)/X1
      RETURN
      END
C
      SUBROUTINE SOLVE (R,A,B,M)
      DOUBLE PRECISION R(260),A(260),B(260),F(260),TF(260)
      DOUBLE PRECISION ALPHA,BETA,GAMMA,C,Q
      F(1)=1.D0
      ALPHA=R(1)
      BETA=R(2)
```

Figure E1. Wideband Jammer (WIDBJAM) Program Listing
(Sheet 3 of 4 Sheets)

```
      A(1)=B(1)/R(1)
      GAMMA=A(1)*R(2)
      DO 1 N=2,M
      NM1=N-1
      C=-BETA/ALPHA
      IF (N-2) 2,2,3
    3 DO 4 J=2,NM1
      NN=N-J+1
    4 TF(J)=F(J)+C*F(NN)
      DO 5 J=2,NM1
    5 F(J)=TF(J)
    2 F(N)=C*F(1)
      ALPHA=ALPHA+C*BETA
      BETA=0.D0
      DO 6 J=1,N
      NN=N-J+2
    6 BETA=BETA+F(J)*R(NN)
      Q=(B(N)-GAMMA)/ALPHA
      DO 7 J=1,NM1
      NN=N-J+1
    7 A(J)=A(J)+Q*F(NN)
      A(N)=Q*F(1)
      GAMMA=0.D0
      DO 8 J=1,N
      NN=N-J+2
    8 GAMMA=GAMMA+A(J)*R(NN)
    1 CONTINUE
      RETURN
      END
C
      SUBROUTINE ERROR (R,W,B,BHAT,X,Y,N)
      DOUBLE PRECISION R(N),W(N),B(N),BHAT(N),SUM,X,Y
      X=1.D-16
      Y=0.D0
      DO 1 J=1,N
      SUM=0.D0
      DO 2 K=1,N
      KK=1+J-K
      IF (K.GT.J) KK=1+K-J
    2 SUM=SUM+R(KK)*W(K)
      IF (DABS(B(J)).LT.1.D-12) GO TO 3
      BHAT(J)=DABS((SUM-B(J))/B(J))
    3 Y=Y+BHAT(J)
    1 IF (BHAT(J).GT.X) X=BHAT(J)
      Y=Y/DBLE(N)
      RETURN
      END
```

Figure E1. Wideband Jammer (WIDBJAM) Program Listing (Sheet 4 of 4 Sheets)

```
C
C       FILE: NARBJAM
C
C       1.    ALL VARIABLES AND CONSTANTS ARE IN DOUBLE PRECISION
C       2.    A TYPICAL ANGLE IS EVALUATED AS:
C             OMEGA = MOD(2.D0*F(I)*TAU*PI,2.D0*PI)
C       3.    AA AND AM ARE THE MULTIPATH GAINS FOR THE AUXILIARY AND
C             MAIN CHANNELS CORRESPONDINGLY
C
      COMPLEX*16 SUM,C,X(3)
      DOUBLE PRECISION R(600),B(600),W(600),PR(3),PT,Y1,Y2,YT
      DOUBLE PRECISION RR(600),Y(3),XX,XN,TAU,S4,PI,T,T0,T1,TR,TR1,RD
      DOUBLE PRECISION BHAT(600),BW,F(3),G(2),TY,XT,P,RA,RMA,RN,AA,AM
      COMMON AA,AM,T0,T1
      COMMON /B1/F,PI
      COMMON /B2/G
      COMMON /B3/BW
      COMMON /B4/S4
      PI=3.14159265358979320+0
      RD=1.0D-9
      IF=102
      READ (3,*) T,(F(I),I=1,2),BW,(G(I),I=1,2),AM,AA
C
C       THE FOLLOWING NORMALIZATIONS ARE ASSUMED IN THE DEFINITIONS
C       OF THE PROGRAM VARIABLES:
C       F(1)=F1*1.E-6          F(2)=F2*1.E-6          BW=BW*1.E-6
C       T0=T0*1.E+6            T1=T1*1.E+6            T=T*1.E+6
C
      T1=1.D-4
      TR=T1/T
      F(3)=(F(1)+F(2))/2.D0
      WRITE (IF,100) (F(I),I=1,2),BW,(G(I),I=1,2),AM,AA,T,TR,DD
  100 FORMAT (/,5X,'F1 = ',F5.1,22X,'F2 = ',F5.1,15X,'NOISE
     ,BANDWIDTH = ',F5.1,10X,'(MEGAHERTZ)',
     ,/,5X,'GAMMA1 = ',F5.1,18X,'GAMMA2 = '
     ,F6.1,10X,'ALPHA OF MAIN = ',F8.6,10X,
     ,'ALPHA OF AUXILIARY = ',F8.6,/,5X,
     ,'TAP DELAY LENGTH = ',F5.3,10X,'T1/T = ',D12.4,36X,
     ,'(MICROSECONDS)',/,5X,'WHITE NOISE ADDED TO RA(1) =',D10.2)
      N=8
      DO 1 M=1,4
      YT=0.D0
      WRITE (IF,200) N
  200 FORMAT (//,5X,'# OF DELAY TAPS = ',I3,/)
      XN=DBLE(N)
      T0=-.01D0*T
      WRITE (IF,300)
  300 FORMAT (1X,'T0/T',12X,'PR',14X,
     ,'PR1',14X,'PR2',14X,'PR0',12X,'MAX. NORM. B ERROR',8X,'AVER.
     , NORM. B ERROR',/)
```

Figure E2. Narrowband Jammer (NARBJAM) Program Listing (Sheet 1 of 4 Sheets)

```
      DO 3 L=1,180
      T0=T0+.01D0*T
      TR1=T0/T
      DO 2 J=1,N
      Y1=DBLE(1-J)*T/XN
      Y2=DBLE(-J+1)*T/XN
      R(J)=RA(Y1)
      RR(J)=S4
    2 B(J)=RMA(Y2)
      R(1)=R(1)+RD
      CALL SOLVE (R,W,B,N)
      R(1)=R(1)-RD
      CALL ERROR (R,W,B,BHAT,XX,YY,N)
      YT=YT+YY
      DO 7 K=1,2
      SUM=DCMPLX(0.D0,0.D0)
      DO 4 J=1,N
      XT=DBLE(J-1)*T/XN
      X(1)=2.D0*P(K)*XT
      X(2)=2.D0*P(K)*(XT+T0+T1)
      X(3)=2.D0*P(K)*T0
      DO 8 JJ=1,3
      Y(JJ)=DMOD(Y(JJ),2.0D0)*P1
    8 X(JJ)=DCMPLX(0.D0,-Y(JJ))
    4 SUM=SUM+W(J)*(CDEXP(X(1))+AA*CDEXP(X(2)))
      C=1.D0+AM*CDEXP(X(3))-SUM
    7 PR(K)=G(K)*(CDABS(C)**2)
      P=0.D0
      DO 5 K=1,N
      DO 5 J=1,N
      JJ=IABS(K-J)+1
    5 P=P+W(K)*W(J)*RR(JJ)
      PR(3)=P
      PT=PR(1)+PR(2)+PR(3)
      PT=10.D0*DLOG10(PT)
      DO 6 K=1,3
    6 PR(K)=10.D0*DLOG10(PR(K))
      WRITE (IF,400) TR1,PT,(PR(K),K=1,3),XX,YY
  400 FORMAT (1X,F4.2,4(6X,F11.6),2(10X,D14.7))
    3 CONTINUE
      YT=YT/180.D0
      WRITE (IF,500) YT
  500 FORMAT (10X,'AVERAGE NORMALIZED E ERROR = ',D14.7)
    1 N=N*2
      STOP
      END
C
      FUNCTION RA(TAU)
      COMMON AA,AM,T0,T1
      COMMON /B4/S4
      DOUBLE PRECISION AA,AM,TAU,T0,T1,S1,S2,S3,S4,RA,RS,RN
```

Figure E2. Narrowband Jammer (NARBJAM) Program Listing (Sheet 2 of 4 Sheets)

```
      S1=RS(TAU)
      S2=RS(TAU-T0-T1)
      S3=RS(TAU+T0+T1)
      S4=RN(TAU)
      RA=(1.D0+AA**2)*S1+AA*(S2+S3)+S4
      RETURN
      END
C
      FUNCTION RS(TAU)
      DOUBLE PRECISION F(3),G(2),X(2),TAU,RS,Y,PI
      COMMON /B1/F,PI/B2/G
      RS=0.D0
      DO 1 K=1,2
      X(K)=2.D0*F(K)*TAU
      X(K)=DMOD(X(K),2.0D0)*PI
      Y=DCOS(X(K))
    1 RS=RS+G(K)*Y
      RETURN
      END
C
      FUNCTION RMA(TAU)
      DOUBLE PRECISION AA,AM,TAU,T0,T1,S1,S2,S3,S4,RMA,RS
      COMMON AA,AM,T0,T1
      S1=RS(TAU)
      S2=RS(TAU-T0-T1)
      S3=RS(TAU+T0)
      S4=RS(TAU-T1)
      RMA=S1+AA*S2+AM*S3+AA*AM*S4
      RETURN
      END
C
      FUNCTION RN(TAU)
      DOUBLE PRECISION F(3),BW,TAU,X1,X2,X3,Y,RN,PI
      COMMON /B1/F,PI/B3/BW
      RN=1.D0
      IF (TAU.EQ.0.0D0) RETURN
      X1=BW*TAU
      X3=X1*PI
      X1=DMOD(X1,2.0D0)*PI
      X2=2.0D0*F(3)*TAU
      X2=DMOD(X2,2.0D0)*PI
      RN=DSIN(X1)*DCOS(X2)/X3
      RETURN
      END
C
      SUBROUTINE SOLVE (R,A,B,M)
      DOUBLE PRECISION R(600),A(600),B(600),F(600),IF(600)
      DOUBLE PRECISION ALPHA,BETA,GAMMA,C,Q
      F(1)=1.D0
```

Figure E2. Narrowband Jammer (NARBJAM) Program Listing (Sheet 3 of 4 Sheets)

```
      ALPHA=R(1)
      BETA=R(2)
      A(1)=B(1)/R(1)
      GAMMA=A(1)*R(2)
      DO 1 N=2,M
      NM1=N-1
      C=-BETA/ALPHA
      IF (N-2) 2,2,3
    3 DO 4 J=2,NM1
      NN=N-J+1
    4 IF(J)=F(J)+C*F(NN)
      DO 5 J=2,NM1
    5 F(J)=IF(J)
    2 F(N)=C*F(1)
      ALPHA=ALPHA+C*BETA
      BETA=0.D0
      DO 6 J=1,N
      NN=N-J+2
    6 BETA=BETA+F(J)*R(NN)
      Q=(B(N)-GAMMA)/ALPHA
      DO 7 J=1,NM1
      NN=N-J+1
    7 A(J)=A(J)+Q*F(NN)
      A(N)=Q*F(1)
      GAMMA=0.D0
      DO 8 J=1,N
      NN=N-J+2
    8 GAMMA=GAMMA+A(J)*R(NN)
    1 CONTINUE
      RETURN
      END
C
      SUBROUTINE ERROR (R,W,B,BHAT,X,Y,N)
      DOUBLE PRECISION R(600),W(600),B(600),BHAT(600),SUM,X,Y
      X=1.0D-16
      Y=0.D0
      DO 1 J=1,N
      SUM=0.D0
      DO 2 K=1,N
      KK=1+J-K
      IF (K.GT.J) KK=1+K-J
    2 SUM=SUM+R(KK)*W(K)
      IF (DABS(B(J)).GT.1D-12) GO TO 3
      BHAT(J)=DABS((SUM-B(J))/B(J))
    3 Y=Y+BHAT(J)
    1 IF (BHAT(J).GT.X) X=BHAT(J)
      Y=Y/DBLE(N)
      RETURN
      END
```

Figure E2. Narrowband Jammer (NARBJAM) Program Listing (Sheet 4 of 4 Sheets)

```
C
C     FILE: INTERPOL
C
C     1.  THIS PROGRAM INVESTIGATES THE INTERPOLATION OF A BANDLIMITED
C         PROCESS OF DURATION T AS A FUNCTION MAINLY OF THE LOCATION OF
C         THE POINT TAU WHERE THE PROCESS IS INTERPOLATED.
C     2.  THE PROCESS IS SAMPLED AT N POINTS.
C     3.  THE MINIMUM MEAN SQUARED ERROR (EMIN) IS CALCULATED IN DB
C         AS A FUNCTION OF THE BANDWIDTH TIME PRODUCT BT (B*T), FRACTIONAL
C         BANDWIDTH BF (B/F0), THE NUMBER OF SAMPLES N, AND THE NORMALIZED
C         POINT OF INTERPOLATION TT (TAU/T).
C     4.  ALL VARIABLES AND CONSTANTS ARE IN DOUBLE PRECISION
C     5.  A TYPICAL ANGLE IS EVALUATED AS:
C         OMEGA = MOD(2.D0*F(I)*TAU,2.D0)*PI
C
      DOUBLE PRECISION R(260),B(260),W(260),BHAT(260)
      DOUBLE PRECISION EMIN,XN,PI,TT,XX,YY,Y1,Y2,YT
      DOUBLE PRECISION BF,BT,Y,P,RX,RD,DTT,RT(13)
      COMMON /B1/BF,BT,PI
      PI=3.1415926535897932D+0
      RD=0.D0
      BF=.2
      RT(1)=1.
      RT(2)=1.1
      RT(3)=1.2
      RT(4)=1.5
      RT(5)=2.
      DO 10 J=6,13
   10 RT(J)=RT(J-1)*2.
      IF=101
      N=2
      XN=DBLE(N)
      DTT=.0025D0
      WRITE (IF,100) BF,N,RD
  100 FORMAT (/,5X,'FRACTIONAL BANDWIDTH = ',F3.1,10X,
     ,'# SAMPLES =',I3,
     ,5X,'WHITE NOISE ADDED TO RA(1) =',D10.2)
      DO 1 M=1,13
      YT=0.D0
      TT=-DTT
      BT=XN/(RT(M)*(1.D0+2.D0/BF))
      WRITE (IF,200) RT(M),BT
  200 FORMAT (/,5X,'RATIO OF SAMPLING TO NYQUIST RATE = ',
     ,F8.1,10X,'TIME BANDWIDTH PRODUCT = ',F9.6)
      DO 3 L=1,1600
      TT=TT+DTT
      DO 2 J=1,N
      Y1=DBLE(J-1)/XN
      Y2=TT+DBLE(-J)/XN
      R(J)=RX(Y1)
    2 B(J)=RX(Y2)
```

Figure E3. Interpolation and Extrapolation of a Bandlimited Process (INTERPOL) Program Listing (Sheet 1 of 3 Sheets)

```
      R(1)=R(1)+RD
      CALL SOLVE (R,W,B,N)
      R(1)=R(1)-RD
      CALL ERROR (R,W,B,BHAT,XX,YY,N)
      YT=YT+YY
      P=0.D0
      Y=0.D0
      DO 4 K=1,N
      DO 5 J=1,N
      JJ=IABS(K-J)+1
    5 P=P+W(K)*W(J)*R(JJ)
    4 Y=Y+W(K)*B(K)
        EMIN=1.0D0+P-2.D0*Y
        IF (EMIN.LE.0.D0) GO TO 6
        EMIN=10.D0*DLOG10(EMIN)
        GO TO 3
    6 EMIN=-100.D0
    3 WRITE (1F,300) TT,EMIN,XX,YY
  300 FORMAT (1X,'TAU/T = ',F7.5,5X,
     ,'MIN. MEAN SQ. ERROR = ',F11.6,5X,'MAX NORM. B ERR. = '
     ,,D14.7,5X,'AVE. NORM. B ERR. = ',D14.7)
        YT=YT/1600.D0
        WRITE (IF,400) YT
  400 FORMAT (10X,'AVE. NORM. B ERROR = ',D14.7)
    1 CONTINUE
      STOP
      END
C
      FUNCTION RX (TAU)
      DOUBLE PRECISION BF,BT,TAU,X1,X2,X3,RX,PI
      COMMON /B1/BF,BT,PI
      RX=1.0D0
      IF (TAU.EQ.0.0D0) RETURN
      X1=BT*TAU
      X3=DMOD(X1,2.0D0)*PI
      X1=X1*PI
      X2=2.0D0*BT*TAU/BF
      X2=DMOD(X2,2.0D0)*PI
      RX=DSIN(X3)*DCOS(X2)/X1
      RETURN
      END
C
      SUBROUTINE SOLVE (R,A,B,M)
      DOUBLE PRECISION R(260),A(260),B(260),F(260),TF(260)
      DOUBLE PRECISION ALPHA,BETA,GAMMA,C,Q
      F(1)=1.D0
```

Figure E3. Interpolation and Extrapolation of a Bandlimited Process (INTERPOL) Program Listing (Sheet 2 of 3 Sheets)

```
      ALPHA=R(1)
      BETA=R(2)
      A(1)=B(1)/R(1)
      GAMMA=A(1)*R(2)
      DO 1 N=2,M
      NM1=N-1
      C=-BETA/ALPHA
      IF (N-2) 2,2,3
    3 DO 4 J=2,NM1
      NN=N-J+1
    4 TF(J)=F(J)+C*F(NN)
      DO 5 J=2,NM1
    5 F(J)=TF(J)
    2 F(N)=C*F(1)
      ALPHA=ALPHA+C*BETA
      BETA=0.D0
      DO 6 J=1,N
      NN=N-J+2
    6 BETA=BETA+F(J)*R(NN)
      Q=(B(N)-GAMMA)/ALPHA
      DO 7 J=1,NM1
      NN=N-J+1
    7 A(J)=A(J)+Q*F(NN)
      A(N)=Q*F(1)
      GAMMA=0.D0
      DO 8 J=1,N
      NN=N-J+2
    8 GAMMA=GAMMA+A(J)*R(NN)
    1 CONTINUE
      RETURN
      END
C
      SUBROUTINE ERROR (R,W,B,BHAT,X,Y,N)
      DOUBLE PRECISION R(N),W(N),B(N),BHAT(N),SUM,X,Y
      X=1.D-16
      Y=0.D0
      DO 1 J=1,N
      SUM=0.D0
      DO 2 K=1,N
      KK=1+J-K
      IF (K.GT.J) KK=1+K-J
    2 SUM=SUM+R(KK)*W(K)
      IF (DABS(B(J)).LT.1.D-12) GO TO 3
      BHAT(J)=DABS((SUM-B(J))/B(J))
    3 Y=Y+BHAT(J)
    1 IF (BHAT(J).GT.X) X=BHAT(J)
      Y=Y/DBLE(N)
      RETURN
      END
```

Figure E3. Interpolation and Extrapolation of a Bandlimited Process (INTERPOL) Program Listing (Sheet 3 of 3 Sheets)

```
C
C       FILE: PLTDAT
C
        DIMENSION X(182),Y(182)
        DOUBLE PRECISION RD
        IN=180
        IF=101
        IG=30
        READ (IF,100) F,BW,G,AM,AA,T,TR,RD
  100 FORMAT (/,9X,F7.2,40X,F5.1,/,12X,F7.1,36X,F8.6,31X,
       ,F8.6,/,23X,F5.3,17X,F7.4,/ ,33X,D10.2)
        WRITE (IG,200) F,BW,G,AM,AA,T,TR,RD
  200 FORMAT (/,5X,'F0 =',F7.2,23X,'NOISE BANDWIDTH =',F5.1,10X,'(MEG
       ,AHERTZ)',/,5X,'GAMMA =',F7.1,20X,'ALPHA OF MAIN = ',F8.6,10X,
       ,'ALPHA OF AUXILIARY = ',F8.6,/,5X,'TAP
       ,DELAY LENGTH =',F5.3,11X,'T1/T =',F7.4,19X,'(MICROSECONDS)',/,
       ,5X,'WHITE NOISE ADDED TO RA(1) =',D10.2)
        DO 1 J=1,4
        READ (IF,300) N
  300 FORMAT (//,22X,I3)
        WRITE (IG,400) N
  400 FORMAT (//,5X,'# OF DELAY TAPS =',I3)
        DO 2 I=1,IN
        READ (IF,500) X(I),Y(I)
        IF (Y(I).LT.-30.0) Y(I)=-30.0
    2 CONTINUE
  500 FORMAT (8X,F4.2,15X,F16.10)
        IF (J.GT.1) GO TO 3
        CALL PLOTST (1.,2HIN,1)
        Y(IN+1)=-30.
        Y(IN+2)=10.
        X(IN+1)=0.
        X(IN+2)=.2
        CALL AXIS (.5,.5,4HT0/T,-4,9.,0.,X(IN+1),X(IN+2))
        CALL AXIS (.5,.5,6HPR(DB),6,6.,90.,Y(IN+1),Y(IN+2))
        CALL PLOT (.5,.5,-3)
    3 CALL LINE (X,Y,IN,1,0,1)
    1 READ (IF,*)
        CALL PLOT (0.,0.,-3)
        CALL PLOTND
        CALL EXIT
        STOP
        END
```

Figure E4. Plotting Routine Program Listing (PLTDAT)

REFERENCES

[1] P.W. Howells, "Intermediate Frequency Side-Lobe Canceller," Patent 3202990, Aug. 24, 1986 (filed May 4, 1959).

[2] S.P. Applebaum, "Adaptive Arrays," Syracuse University Research Corp., Rep. SPL-709, June 1964; reprinted in IEEE Trans. Antennas Propagat., Vol. A-24, pp. 573-598, Sept. 1976.

[3] B. Widrow et al., "Adaptive Antenna Systems," Proc.IEEE, Vol. 55, pp. 2143-2159, Dec. 1967.

[4] F.R. Dickey, Jr., "Photo-electric Acoustic Adaptive Signal Processor," General Electric Co., Heavy Military Equipment Department, Syracuse, N.Y., Report No. R75EMH9, March 1975.

[5] M.M. Fitelson, "Acousto-Optic Adaptive Processor (AOAP)," General Electric Co., Electronics Laboratory, Syracuse, N.Y., Report No. R77ELS029, June 1977.

[6] W.A. Penn, S. Wanuga and M.M. Fitelson, "Analysis and Development Status of the Acousto-Optic Adaptive Processor (AOAP)," GE Class 3 TIS #R78ELS030, May 1978.

[7] Morgan, D.R., "An Analysis of Multiple Correlation Cancellation Loops with a Filter in the Auxiliary Path," IEEE Trans. on Acoustics, Speech, and Sig. Proc., Vol. ASSP-28, No. 4, August 1980.

[8] Hitachi Laser Diode Application Manual (HLP 1000, HLP 2000, HLP 3000 Series) Published by Hitachi, Ltd., Tokyo, Japan.

[9] M. Born, E. Wolf, Principles of Optics, Pergamon Press, New York, 1959, pp. 62-681.

[10] E.G. Coker, L.N.G. Filon, A Treatise on Photo-Elasticity, Cambridge University Press, London, 1957, pp. 181-192, 209-210.

[11] W.G. Hoefer, "Theory of Optical Diffraction by Ultrasonic Waves in Solid Media," General Electric Electronics Laboratory, Final Report DA-983-FH-370, January 14, 1966, pp. 10-20.

[12] W.P. Mason, "Acoustic Properties of Solids," (Sec. 3f), American Institute of Physics Handbook, D.E. Gray, Editor, McGraw-Hill, New York, 1957, pp. 3-75 to 3-84.

[13] W.R. Klein, B.D. Cook, "Unified Approach to Ultrasonic Light Diffraction," IEEE Transactions on Sonics and Ultrasonics, Vol. SU-14, No. 3, July 1967, pp. 123-134.

[14] D.A. Pinnow, "Guide Lines for the Selection of Acousto-Optic Materials," IEEE Journal of Quantum Electronics, Vol. QE-6, No. 4, April 1970, pp. 223-238.

[15] "Optical Signal Processing Study for Terminal BMD Radars," General Electric Co., Electronic Systems Division, June 30, 1976, Final Report Contract No. DASG 60-75-C-0104, pp. 4-13.

[16] "Typical Absolute Spectral Response Characteristics of Photoemissive Devices" and "Typical Absolute Spectral Response Characteristics of Aluminized Phosphor Screens," Charts published by ITT, Electro-Optical Products Division, Ft. Wayne, Indiana.

[17] W.P. Bleha, et. al., "Application of the Liquid Crystal Light Valve to Real Time Optical Data Processing," Optical Engineering (Journal of the Society of Photo-Optical Instrumentation Engineers), Vol. 17, No. 4, July-August 1978, pp. 371-384.

[18] D.R. Morgan and S.E. Craig, "Real Time Adaptive Linear Prediction Using the Least Mean Square Gradient Algorithm," IEEE Trans. Acoust., Speech, Signal Processing, Vol. ASSP-24, pp. 494-507, Dec. 1976.

[19] B. Widrow et al, "Adaptive Noise Cancelling: Principles and Applications," Proc. IEEE, Vol. 63, pp. 1692-1716, Dec. 1975.

[20] J. Makhoul, "Linear Prediction: A Tutorial Review," Proc. IEEE, Vol. 63, pp. 561-580, April 1975.

[21] J. Makhoul, "Spectral Linear Prediction: Properties and Applications," IEEE Trans. on Acoustics, Speech and Signal Proc., Vol. ASSP-23, pp. 283-296, June 1975.

[22] D.R. Morgan, "Response of a Delay-Constrained Adaptive Linear Predictor Filter to a Sinusoid in White Noise," General Electric Co., Electronics Laboratory, Syracuse, N.Y., Report No. R81ELS014, March 1981.

[23] A. Papoulis, Probability, Random Variables and Stochastic Processes, McGraw-Hill, New York, 1965.

[24] J.L. Moschner, "Adaptive Filter with Clipped Input Data," Stanford University, Information Systems Laboratory, Stanford, Calif., Report No. 6796-1, June 1970.

[25] J.R. Treichler, "Transient and Convergent Behavior of the Adaptive Line Enhancer," IEEE Trans. Acoustics, Speech, and Signal Proc., Vol. ASSP-27, pp. 53-62, Feb. 1979.

[26] B. Widrow, "Adaptive Filters I: Fundamentals," Stanford Electronics Lab., Stanford, CA., Rep. SEL-66-126 (Tech. Rep. 6764-6), Dec. 1966.

[27] B. Widrow, "Adaptive Filters," in Aspects of Networks and System Theory, Part IV, R.E. Kalman and N. DeClaris, Eds. New York: Holt, Rinehart, and Winston, 1971, pp. 563-587.

[28] R.W. Lucky, "Adaptive Redundancy Removal in Data Transmission," Bell Syst. Tech. J., pp. 549-573, Apr. 1968.

[29] J.R. Rosenberger and E.J. Thomas, "Performance of an Adaptive Echo Canceller Operating in a Noisy, Linear, Time-Invariant Environment," Bell Syst. Tech. J., pp. 785-813, Mar. 1971.

[30] R.W. Lucky, "A Survey of the Communication Literature," IEEE Trans. Inform. Theory, Vol. IT-19, pp. 725-739, Nov. 1973.

[31] D.R. Morgan, "Adaptive Multipath Cancellation for Digital Data Communications," IEEE Trans. Commun., Vol. COM-26, pp. 1380-1390, Sept. 1978.

[32] N. Wiener, Extrapolation Interpolation and Smoothing of Time Series, Cambridge, Mass.: MIT Press, 1966, Appendix B.

[33] A. Gersho, "Adaptive Equalization of Highly Dispersive Channels for Data Transmission," Bell Syst. Tech. J., Vol. 48, pp.55-70, Jan. 1969.

[34] J.D. Markel, "Formant Trajectory Estimation from a Linear Least-squares Inverse Filter Formulation," Speech Communication Research Lab Inc., Santa Barbara, Calif. AD 734679, Oct. 1971.

MISSION
of
Rome Air Development Center

RADC plans and executes research, development, test and selected acquisition programs in support of Command, Control Communications and Intelligence (C^3I) activities. Technical and engineering support within areas of technical competence is provided to ESD Program Offices (POs) and other ESD elements. The principal technical mission areas are communications, electromagnetic guidance and control, surveillance of ground and aerospace objects, intelligence data collection and handling, information system technology, ionospheric propagation, solid state sciences, microwave physics and electronic reliability, maintainability and compatibility.